AN ABSTRACT OF THE DISSERTATION OF

Mingyang Tan for the degree of Doctor of Philosophy in Chemical Engineering presented on September 6, 2018.

Title: A Study of the Dynamics and Rheology of Passive and Active Suspensions of Particles with Various Geometries

Abstract approved: _____

Travis W. Walker

Suspensions of particles in fluids are everywhere in our life, such as paints, pharmacies, food, etc. Suspensions can exhibit properties that common fluids do not possess. For example, the paint needs to flow well when brushing so that it can be smeared on the wall, which is aided by the *shear-thinning* of the fluid. However, when brushing stops, paint needs to stay still on the wall, which is aided by the *yield-stress* of the paint. These types of behavior depend on the dynamics and microstructures of the suspensions. Suspensions of particles can serve as precursors of composite materials, for example, a composite can be created by curing a suspension of particles in a monomer solution. In such case, the properties of the composite can be affected by the dynamics of the fluid. Investigating the dynamics of suspensions of particles can be crucial to the manufacture of composite

materials.

This study covers theoretical, computational, and experimental studies of suspensions of particles in various aspects, such as suspensions of spherical and aspherical particles, suspensions with or without external fields, and suspensions in Newtonian and non-Newtonian fluids.

The theoretical and computational study focuses on a fundamental investigation of the dynamics of the suspending particles. Under a magnetic field, magnetic disks can be aligned by a magnetic field. An analytic solution that describes the motion of a single magnetic disk under a rotating field is derived in this study, and it has shown good comparison with experimental data. When multiple particles are present in the fluid, the particles interact with each other hydrodynamically and magnetically if a magnetic field is applied. Under the influence of the magnetic field, the microstructures of the material can be altered. The dynamic behavior depends on hydrodynamic interactions. I discuss the hydrodynamic and magnetic interactions from a fundamental point of view, and I implement a computational method called *Stokesian dynamics* to simulate such systems. Furthermore, I also discuss a way of simulating aspherical suspensions that is based on the spherical suspensions.

The experimental study focuses on the characterization of complex fluids by suspending microparticles as the probes that can measure the local properties of fluids, and the method is called *microrheology*. The complex fluids that are characterized

in this study serve as an inexpensive substitute of the sputum of *cystic fibrosis* (CF) patients. The goal of this part of the study is to explore an efficient drug-delivery vehicle that can transport through the mucus of CF patients. The formula of the substituting fluids that are proposed by our lab has shown similar rheological properties with the sputum from CF patients in the macroscopic lengthscale. I also characterized the fluids in the microscopic lengthscale and I have seen differences between the macroscopic and microscopic properties. I deduce that the differences arise from the heterogeneity of the fluids, which cannot be well detected in the macroscopic method.

Finally, I combine the knowledge that we obtain from the theoretical study with the technique that we utilize in the experimental study to obtain a proof-of-concept study. We have successfully suspended microdisks in a yield-stress fluid so that the microdisks can be aligned while constrained in the elastic cages of the fluid. The yield-stress is characterized by a microrheological technique, and we apply the scalings that we have derived previously to control the parameters to achieve the goal of aligning microdisks while suppressing the translations of microdisks.

A Study of the Dynamics and Rheology of Passive and Active Suspensions of Particles with Various Geometries

by

Mingyang Tan

A DISSERTATION

submitted to

Oregon State University

in partial fulfillment of
the requirements for the
degree of

Doctor of Philosophy

Presented September 6, 2018
Commencement June 2019

Doctor of Philosophy dissertation of Mingyang Tan presented on September 6, 2018.

APPROVED:

Major Professor, representing Chemical Engineering

Head of the School of Chemical, Biological, and Environmental Engineering

---

Dean of the Graduate School

I understand that my dissertation will become part of the permanent collection of Oregon State University libraries. My signature below authorizes release of my dissertation to any reader upon request.

Mingyang Tan, Author

ACKNOWLEDGEMENTS

The five years of Ph.D study cannot be accomplished solely by myself without all the help I've received during this meaningful journey.

The person who gives me the most academic help, of course, is my advisor Travis. As the model of my academic life, Travis teaches me how to research, write, program, and how to tell a good story. It is not the knowledge that I've learned from him that benefits me the most, it is the way he thinks and tackles problems. I've learned to look at the problems from a fundamental point of view. Travis is also a good friend in life. He has helped me a lot in dealing with the things that are painful to me, like moving my furnitures using his great strength. My another advisor, Skip, gives me tremendous help in my experiments. Skip is always generous of letting me use the goodies in his lab, giving me directions of running instruments, and answering my questions. His passion of work motivates me to pursue my goals. His sense of humor gives me a lot of joy. Also, I'm grateful to Albrecht and Pallavi for giving me help in electromagnetics. The major part of this work started from a discussion n a coffee shop five years ago about aligning magnetic disks. I also would like to thank Líney Árnadóttir and Martin Fisk for being my committee members, as well as Kate Schilke as my former committee member.

The help and joy brought from my colleagues is also an important part of my

Ph.D journey. My lab mate, Yating, has helped a lot in the experiments. The microrheological study cannot progress so well without her help. By the way, she makes the saltiest and numbest (caused by a kind of pepper from China) food that I've ever tried. Brit is a passionate and generous lady who has never turned down my request for help to me and my wife! Kat is the nicest lady I've ever met in the U.S. I am thankful to her for bringing the very useful Ibidi micro-channels to the lab, for holding good parties in her house, and for giving support to my life.

I'm sincerely grateful to my parents, Yixin Li and Xisheng Tan, for giving me the deepest love and unconditional support. I cannot achieve what I have without them. They come to the U.S every six months since September 2016 to help taking care of my son and my life and give me enough freedom for me to pursue what I am interested in since I was a little boy. The same gratefulness is to my parents in law, Xiu Qiao and Yongyao Jiang, who also take turns of coming to the U.S. to help my family. I would like to thank my other family members, my grandparents, my cousins, my uncles, and aunts for giving me their love. I know my nanna is watching me and protecting me from the heaven all the time.

Finally and most importantly, the people I want to thank the most is my wife Lingting and my son Neal. My life cannot be colorful and complete without them. Lingting gives me any support that I ask for and has never complained about the difficulties in life. She is the most honest and sincere person that I know. Her gentleness as well as toughness have made our family a warm and strong one. Neal

is the biggest joy brought to my life. His laughter is better than anything that can erase my depression and weariness. Having them, I know what I am fighting for.

TABLE OF CONTENTS

TABLE OF CONTENTS (Continued)

TABLE OF CONTENTS (Continued)

LIST OF FIGURES

LIST OF FIGURES (Continued)

LIST OF FIGURES (Continued)

LIST OF FIGURES (Continued)

LIST OF TABLES

LIST OF APPENDIX FIGURES

Chapter 1

Introduction and Background

Suspensions of particles are ubiquitous in both nature and engineering fields, such as proteins, bacteria, and viruses in biological fluids, precursors of composite materials, dispersions of pigments in paint, and mixtures of polymer emulsions. The study of the mechanical properties of such substances requires rheological measurements. A rheological measurement perturbs (slightly or significantly) the substance out of equilibrium and measures the stress responses. Thus, the study of the dynamics of the non-equilibrium state of materials is crucial to understanding the rheology of these materials.

This study is divided into two main parts. The first part focuses on the theoretical and computational study of the dynamics of suspensions of particles. The motivation of this part is to fabricate magnetic composites that would be used in high-frequency applications such as antennae and inductors. The magnetic microparticles are suspended in a monomer solution, and a magnetic field and a UV light are applied to the medium to achieve a polymer-metal mixture with different microstructures of the magnetic particles, depending on the properties of the particles and magnetic fields. The equilibrium structure depends on the magnetic interactions between magnetic particles, while the non-equilibrium dynamics depend on the hydrodynamic interactions. Both interactions are addressed in this study, and theoretical models are proposed to describe the dynamics and predict the rheological properties. Although many studies of the dynamic simulations of suspensions focus on spherical particles, aspherical particles will be investigated in this study, not only because a limited number of studies of aspherical particles exist, but also the anisotropic properties caused by the aspherical particles raise new problems in different fields. Models of spherical particles are also discussed in this study, since they are the foundations of the method that is used in this study, and also they are used as benchmarks of the method. The details of the theoretical studies are presented in Chapters 2 and 3.

The second part investigates the microrheological properties of complex fluids. Although the rheological properties were predicted in the first part as a result of simulation, the second part focuses on the experimental study of the rheology.

Microrheology builds the relationship of the motion of probing particles that are suspended in the complex fluids, driven by the thermal energy of the fluids or by external fields, with the mechanical properties of the complex fluids. Thus, mircorheology can measure the mechanical properties of the complex fluids at a lengthscale of the size of the probing particles. The rheological properties that are extracted by microrheological measurements can be comparable to the conventional rheological measurements, or the microrheological properties can be very different from the conventional rheological measurements, relying on the size of the probing particles relative to the characteristic lengthscales of the microstructures of the fluids. If the heterogeneity of the fluids needs to be characterized, for example the motions of microparticles in biological fluids, microrheological study is preferred. The details of the microrheological study are given in Chapter 4. Chapter 5 combines the ideas from Chapter 2, 3, and 4. It uses theoretical scalings based on Chapter 2 and 3 and to predict the dynamics of microdisks that are suspended in a yield-stress fluid, which is characterized by a microrheological technique introduced in Chapter 4.

An overview of the thesis is given below.

> **Chapter 2** studies the rotational motion of a magnetic microdisk under external magnetic fields. In this chapter, the dilute limit is assumed; thus, no hydrodynamic or magnetic interaction between particles is present. An analytic model describing the rotational motion of the microdisk is proposed

and compared to experimental data. Chapter 2 is mainly adapted from a work published by Tan et al. [3].

Chapter 3 relaxes the dilute limit assumption. Models describing the hydrodynamic and magnetic interactions are discussed, and the method we use to simulate the hydrodynamic interactions is *Stokesian dynamics*. The problem is first illustrated in spherical suspensions, and then, the aspherical suspensions are discussed.

Chapter 4 investigates the microrheological properties of xanthan gum (XG) solutions. While in Chapter 3 the particles are suspended in a fluid (Newtonian fluid) with known rheological properties, and we simulate the change of the rheological properties caused by the presence of the particles, in Chapter 4 the rheological properties of the fluids are unknown, and they are measured by the dynamics of the particles. The presence of the particles are assumed to have no effect on the rheological properties (dilute limit). We use a technique called *multiple particle tracking* to characterize the rheological properties of the XG solutions. Chapter 4 is mainly adapted from a paper that is under preparation.

Chapter 5 works as a combination of the two main parts of this study. We have derived several scaling parameters describing the dynamics of the magnetic microdisks that are shown in Chapters 2 and 3. One practical goal of the research is to devise a technique of fabricating a well-dispersed, non-

contacting suspension of magnetic microdisks with uniform orientation. This goal is difficult to achieve in a Newtonian fluid; however, it can be achieved in a fluid with elastic microstructures that are characterized by microrheological methods that are introduced in Chapter 4. Chapter 5 is mainly adapted from a paper published by Tan et al. [4]

Chapter 2

Alignment of a Single Magnetic Particle — Single Particle Dynamics

This chapter is mainly adapted from the work I have published on *Physics of Fluids* [3].

2.1 Introduction

Compared to isotropic composites, anisotropic composites can provide directionally dependent bulk properties that are enhanced in certain directions. Anisotropic composites are found in many natural substances, such as the prismatic layers of teeth [5] and mollusk shells [6] and the plywood fiber structures in fish scales [7], insects [8], and plants [9]. Inspired by the anisotropic architectures of the natural materials, people are committed to developing new materials that contain aligned anisotropic particles [10–13]. These materials can exhibit enhanced magnetic, mechanical, optical, and diffusive (heat and mass) properties. For example, soft magnetic composites, consisting of magnetic particles embedded in an insulating matrix, have great potential for a variety of breakthrough applications, including magneto-optics [14], biological tissue scaffolds [15, 16], drug targeting [17], and high-frequency applications such as microwave absorption, electromagnetic shielding [18], inductors, and antennae [19, 20].

The anisotropic properties of non-spherical particles like rods and disks allow them to be aligned by an external driving torque that can be generated by several techniques. Examples include optical tweezers that use a strongly focused beam of light to trap or move particles with sizes ranging from nanometers to micrometers [21, 22], electrorotation that generates a rotating electric field to rotate elongated metallic particles [23], and dielectrophoresis that uses alternating electric field to manipulate and assemble nanowires [24, 25]. Compared to these tech-

niques, manipulation of ferromagnetic nano- and micro-particles by using magnetic fields provides a low-cost, efficient, and non-contact method that is easy to implement [26]. We denote the particles that can be orientated under magnetic field by magnetically orientable particle (MOP).

In this study, aligned composites are created by orienting magnetic microdisks. Since the particles have a high-susceptibility plane ($\chi_{\perp}^{E}$) in the radial direction perpendicular to the orientation vector, $\mathbf{p}$, and a low-susceptibility axis ($\chi_{\parallel}^{E}$) that is parallel to $\mathbf{p}$ as shown in Fig. 2.1(a), a planar rotating magnetic field can be used to align the particles in the plane Fig. 2.1(b). This work presents a theoretical model that describes the dynamics associated with the orientation of a magnetic oblate spheroid being aligned by a rotating magnetic field.

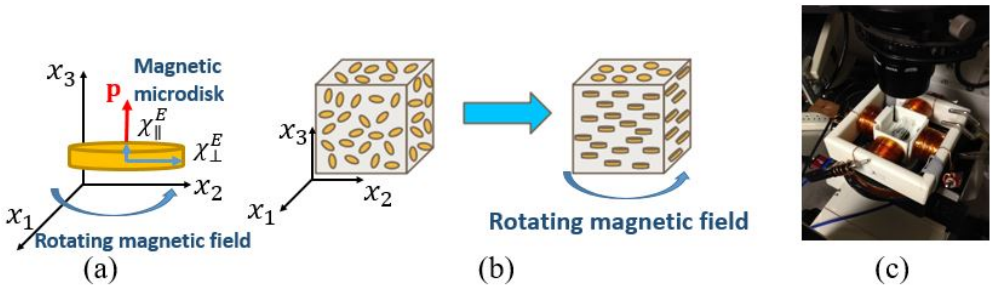

Figure 2.1: **(a)** Magnetic microdisk with in-plane susceptibility, $\chi_{\perp}^{E}$, and out-of-plane susceptibility, $\chi_{\parallel}^{E}$, where $\chi_{\perp}^{E} > \chi_{\parallel}^{E}$, and with orientation vector, $\mathbf{p}$. **(b)** Microdisks aligned by a rotating magnetic field into planar alignment. At first, the microdisks have a random distribution of orientation in the absence of a magnetic field. Upon introducing a rotating magnetic field, the microdisks are aligned such that their $\chi_{\parallel}^{E}$ axis is perpendicular to the magnetic field plane. **(c)** The setup of the experiment–a three-axis electromagnetic coil system mounted on an inverted microscope. The z-coil (not visible) is underneath the x-y coils seen in the picture.

Kimura et al. studied the dynamics of diamagnetic polymer fibers under both static

and dynamic magnetic fields [27,28]. Since a diamagnetic fiber has a lower magnetic susceptibility in its long axis than in its radial plane, its magnetic anisotropy is similar to a ferromagnetic disk, even though the geometries differ. Kimura et al. provided an analytic model to describe the alignment dynamics of diamagnetic rods in a constant magnetic field [27]. They also proposed an asymptotic model that describes the alignment dynamics of diamagnetic rods at the high rotating-frequency limit [28]. However, a complete analytic model that covers all possible frequencies is needed to describe the alignment dynamics of oblate spheroids or disks in a rotating field.

We investigate two types of magnetic fields – *constant* and *rotating* – in this study. A single mathematical representation that covers both types can be constructed by designating the constant field to have a rotating frequency of zero. In a constant magnetic field, the low-susceptibility axis ($\chi_{\parallel}^{E}$) of the microdisk aligns perpendicular to the field direction, but the disk is still free to rotate within the plane that is perpendicular to the field direction. However, in a rotating magnetic field, the high-susceptibility plane of the microdisk is found to seek the shortest opportunity to be aligned with the magnetic field, which is the short-term response driven by magnetics. When the microdisk is rotating with the magnetic field, it experiences a hydrodynamic drag caused by the fluid. To reduce the drag, the microdisk will find a position where the drag can be minimized. Minimum drag is achieved when the plane of the microdisk is aligned in the plane where the magnetic field rotates (i.e., the microdisk reduces the amount of area that the bluff body projects perpen-

dicular to the flow that is caused by the particle's rotation). This drag reduction is the long-term response driven by hydrodyanmics, allowing the orientation of magnetic microdisk.

If the microdisks can be frozen in place after the alignment, a composite with uniformly oriented microdisk fillers can be created as shown in previous works [19, 29]. Driven by the idea of manufacturing magnetic composites, we study the fundamental physics and provide analytic models in this chapter. The analytic models cover the complete range of the frequency of the field, from 0 to ∞, and are confirmed by finite difference numerical methods of the systems. The comparison between the models and experimental results have shown agreement. The models also enable to predict the dependence of bulk rheological properties of composites on the orientation distribution of the particles.

2.2 Experimental Methods and Materials

The goal of this chapter is to present mathematical models that are validated by the experimental results. The experiments follow the work of Song et al. [19, 29]. Ferromagnetic Ni-Fe microdisks with approximately 5 μm diameter and 150 nm thickness (aspect ratio $\approx$ 33) are investigated. The Ni-Fe microdisks are fabricated by wet etching photolithographically patterned permalloy thin films. The microdisks are suspended in a viscosity-standard silicone oil with viscosities of 215 cp and 550 cp (Brookfield Engineering Laboratories, Inc.), which were mea-

sured using a rotational rheometer (DHR-3, TA Instruments). The magnetic field is generated by a three-axis electromagnetic coil system. Initially, an out-of-plane (1, 3-plane) field is generated to align microdisks perpendicular to the plane of observation to maximize unalignment (seeFig. 2.1(a)). Then, an in-plane (1, 2-plane) field is generated to align the microdisks into the plane of observation. To achieve a rotating magnetic field, the 1 and 2 axis coils are driven in quadrature with cosinusoidal and sinusoidal current via a function generator. The dynamics are observed using a Nikon Ti-S inverted microscope with a 40×objective and recorded by a CCD camera (Guppy Pro 125B, Allied Vision). The setup of the experiments is shown in Fig. 2.1(c).

Ferromagnetic materials, such as the microdisks used in this study, can be magnetized by a magnetic field, forming an induced dipole moment, μ_j. Assuming the induced dipole moment is below saturation (the saturation field is 100 mT for Ni-Fe, and the applied field is below 10 mT), the induced moment scales approximately linearly with external field, particle size, and effective susceptibility such that

$$\mu_j = \frac{V}{\mu_0}\chi^E_{jn}B_n, \tag{2.1}$$

where μ_j is the induced dipole moment, V is the particle volume, μ_0 is the free-space permeability, and B_n is the external magnetic field vector. The effective susceptibility, χ^E_{jn}, is a second-order tensor that relates the particle geometry and the induced dipole moment, describing the degree of magnetizing of a material in response to an external field. Generally for ferromagnetic materials, χ^E_{ij} depends

on the magnitude of the external magnetic field; however, in the range of working fields in this study (1—10 mT), χ_{jn}^{E} remains constant for the Ni-Fe microdisk, as determined by vibrating sample magnetometry.

2.3 Layout of Model

In this section, an analytic model is developed to describe the rotational motion of the magnetic microdisk. Since the aspect ratio of the microdisks used in this study is high, we use the oblate spheroid as an analytic surface to approximate the microdisk.

The dynamic study starts with the Langevin equation,

$$\mathbf{M} \cdot \frac{d\mathbf{U}}{dt} = \mathbf{F}^{H} + \mathbf{F}^{E} + \mathbf{F}^{B}, \tag{2.2}$$

where $\mathbf{M}$ is the generalized mass/moment of inertia matrix, $\mathbf{U}$ is the translational/rotational velocities of the particle, $\mathbf{F}^{H}$ is the hydrodynamic force/torque, $\mathbf{F}^{E}$ is the external (magnetic here) force/torque and $\mathbf{F}^{B}$ is the Brownian force/torque. In this chapter, we assume that the suspension is infinitely dilute, or the volume fraction ϕ tends to be null. The particle is assumed to have an induced dipole. Under a uniform external magnetic field, the magnetic force can be neglected. Moreover, the sedimentation time is at least 15 times as long as the alignment. Therefore, the translational motion can be neglected. Thus, we can only focus on the torque balance part of the Langevin equation. In addition, the Reynolds

number is trivial ($\mathcal{O}\left[10^{-7}\right]$) in this study, so the inertia is neglected. Thus, the Langevin equation given by the index notation becomes,

$$T_i^H + T_i^E + T_i^B = 0, \tag{2.3}$$

where T_i^H, T_i^E, and T_i^B are hydrodynamic, external, and Brownian torque respectively. Each of the torque is given by

$$T_i^H = C_{ij}\left(\Omega_j^\infty - \omega_j\right) + H_{ijk}E_{jk}^\infty, \tag{2.4a}$$

$$T_i^E = \varepsilon_{ijk}\mu_j B_k, \text{ and} \tag{2.4b}$$

$$T_i^B = -\varepsilon_{ijk}p_j\frac{\partial\left[k_B T\log\Psi\right]}{\partial p_k}, \tag{2.4c}$$

where C_{ij} and H_{ijk} are hydrodynamic tensors that will be discussed in details later, Ω_j^∞ and E_{jk}^∞ are far-field fluid velocity fields, μ_j is the dipole moment of the particle, B_k is the external magnetic field, p_j is the orientation vector of the particle, k_B is the Boltzmann constant, T is the temperature, Ψ is the probability density function, and ε_{ijk} is the permutation tensor. The torque balance equation yields

$$C_{ij}\left(\Omega_j^\infty - \omega_j\right) + H_{ijk}E_{jk}^\infty + \varepsilon_{ijk}\mu_j B_k - \varepsilon_{ijk}p_j\frac{\partial\left[k_B T\log\Psi\right]}{\partial p_k} = 0. \tag{2.5}$$

In a quiescent fluid, such like this study, Ω_j^∞ and E_{jk}^∞ are set null. Following Kim and Karrila [30], the hydrodynamic tensor, C_{ij}, for an axisymmetric particle can

be written as (H_{ijk} is omitted since the particle is in a quiescent fluid),

$$C_{ij} = 8\pi\eta a^3 \left(X^C p_i p_j + Y^C \left(\delta_{ij} - p_i p_j \right) \right), \tag{2.6}$$

where η is viscosity, a is one-half of the major axis of the particle, and X^C and Y^C are hydrodynamic functions depending on the geometry of the particle. Similar to the hydrodynamic tensor, the induced dipole moment, μ_j, of an axisymmetric particle is [31]

$$\mu_j = \frac{V}{\mu_0} \left(\chi_{\parallel}^E p_j p_n + \chi_{\perp}^E \left(\delta_{jn} - p_j p_n \right) \right) B_n, \tag{2.7}$$

where $\chi_{\parallel}^E$ and $\chi_{\perp}^E$ are the susceptibility parallel and perpendicular to the orientation vector respectively.

The rate-of-change of the orientation vector for an axisymmetric particle is

$$\frac{dp_i}{dt} = \varepsilon_{ijk} \omega_j p_k. \tag{2.8}$$

If we have an explicit expression for the angular velocity, a direct substitution into Eq. (2.8) provides a complete form of the particle alignment dynamics. Before proceeding, we need to make assumptions and clarifications to simplify the equation. First, we define a "rotational Peclét number" to be the ratio between the magnetic torque and the Brownian torque(see details in the Appendix A.2). In the experimental system of this study, the rotational Peclét number is very large ($\mathcal{O}[10^4]$), so the Brownian contribution is trivial and therefore is neglected. Second, we can

write the hydrodynamic tensor, C_{ij}, in an isotropic form such as $C_{ij} = \zeta_r \delta_{ij}$, since the rotation of an axisymmetric particle is isotropic (see proof and details in Appendix A.1). Now, with the assumptions and expressions for the hydrodynamic tensor and induced moment, we have the governing equation as

$$\frac{dp_i}{dt} = -\frac{V\left(\chi_\perp^E - \chi_\parallel^E\right)}{\mu_0 \zeta_r} B_n p_n \left(B_i - B_k p_k p_i\right). \tag{2.9}$$

The leading term on the right-hand-side of Eq. (2.9) contains all the information regarding the particle and the fluid. Since the parameters are held constant for any specific experiment, we define the following combined parameter,

$$A \equiv \frac{V\left(\chi_\perp^E - \chi_\parallel^E\right)}{\mu_0 \zeta_r}. \tag{2.10}$$

For the magnetic microdisks used in this study, the susceptibility in-plane is greater than the susceptibility out-of-plane ($\chi_\perp^E > \chi_\parallel^E$). We can now decouple the magnetic field by setting $B_k \equiv B b_k$, where B is the magnitude of the magnetic field, and b_k is a unit vector pointing in the direction of the magnetic field. At this point in the derivation, we have a characteristic timescale which is the intrinsic timescale that the particle can be aligned in a specific experiment. We can use the intrinsic timescale to nondimensionalize the time and the dimensionless time, τ, is given by

$$\tau = \frac{t}{t_R}, \ \ni t_R = \frac{1}{AB^2}. \tag{2.11}$$

The dimensionless governing equation is then given by

$$\frac{dp_i}{d\tau} = -b_n p_n \left(b_i - b_k p_k p_i\right). \tag{2.12}$$

In the experimental setup, the magnetic field is rotating in the 1, 2 – plane, b_i is given by

$$b_i = \delta_{i1} \cos \omega t + \delta_{i2} \sin \omega t, \tag{2.13}$$

where ω is the rotating frequency. Now we can define a dimensionless frequency, ξ, such as,

$$\xi = \frac{2\omega}{AB^2}. \tag{2.14}$$

Here, the factor 2 is chosen in the dimensionless frequency for algebraic convenience, which is a result of the symmetry of the disk. The disk "sees" the field rotate twice as fast, since the disk cannot distinguish the north pole from the south pole of the field direction.

Note that Eq. (2.12) is set of three ordinary differential equations, each of which corresponds to each component of $\mathbf{p}$. Since $\mathbf{p}$ os restricted to the surface of a unit sphere, rewriting the equation in spherical coordinates, where $p_1 = \sin\theta\cos\varphi$, $p_2 = \sin\theta\sin\varphi$, and $p_3 = \cos\theta$, reduces the number of differential equations from

3 to 2. Thus, Eq. (2.12) becomes

$$\frac{d\varphi}{d\tau} = \frac{1}{2}\sin\left[2\varphi - \xi\tau\right], \text{ and} \tag{2.15a}$$

$$\frac{d\theta}{d\tau} = -\frac{1}{2}\sin 2\theta \cos^2\left[\varphi - \frac{\xi\tau}{2}\right] \tag{2.15b}$$

To ease issues with the oscillatory nature of the problem, we define a new variable u, which is defined to be the angle between the magnetic field direction and the projection of the orientation vector $\mathbf{p}$ on the 1, 2 – plane, such that

$$u = \varphi - \frac{\xi\tau}{2}. \tag{2.16}$$

Then the governing equations become

$$\frac{du}{d\tau} = \frac{1}{2}\sin 2u - \frac{\xi}{2}, \text{ and} \tag{2.17a}$$

$$\frac{d\theta}{d\tau} = -\frac{1}{2}\sin 2\theta \cos^2 u. \tag{2.17b}$$

Now we have a fully nondimensionalized set of first-order, nonlinear ordinary differential equations. We will show in the next section that it can be solved as a function of the one governing parameter ξ, and the corresponding initial conditions, u_0 and θ_0.

2.4 Analytic Solution

The solution depends on the dimensionless frequency ξ as mentioned before, and we will develop the solution in four cases

1. $\xi = 0$
2. $\xi < 1$
3. $\xi = 1$
4. $\xi > 1$

The first case corresponds to the constant field, and the rest corresponds to the rotating field.

2.4.1 Constant Field Solution, $\xi = 0$

A constant magnetic field is the special case of a rotating field where the frequency is null ($\xi = 0$); thus, the direction of b_i is constant, and $b_i = \delta_{i1}$ is chosen for convenience. In this case, the phase shift u is simply equivalent to the azimuthal angle φ. We can write Eq. (2.17a) and (2.17b) with $\xi = 0$ as

$$\frac{d\varphi}{d\tau} = \frac{1}{2}\sin 2\varphi, \text{ and} \tag{2.18a}$$

$$\frac{d\theta}{d\tau} = -\frac{1}{2}\sin 2\theta \cos^2\varphi, \tag{2.18b}$$

and the they can be solved analytically such that

$$\frac{\tan\varphi}{\tan\varphi_0} = \exp\left[\tau\right], \text{ and} \tag{2.19a}$$

$$\frac{\tan\theta}{\tan\theta_0} = \sqrt{\frac{\tan^2\varphi_0 + \exp\left[-2\tau\right]}{1+\tan^2\varphi_0}}, \tag{2.19b}$$

where φ_0 and θ_0 are initial azimuthal and polar angles respectively. If we write the solution in terms of the orientation vector, we have

$$p_1 = \sqrt{\frac{1}{1+\bar{p}^2\exp\left[2\tau\right]}}, \text{ and} \tag{2.20a}$$

$$\sqrt{p_2p_2+p_3p_3} = \frac{\bar{p}}{\sqrt{\bar{p}^2+\exp\left[-2\tau\right]}}, \tag{2.20b}$$

where $\bar{p}^2 = \left.\frac{1-p_1p_1}{p_1p_1}\right|_{\tau=0}$ is the initial orientation of the particle. The solution in Eq. (2.20a) indicates that as $\tau \to \infty$, p_1 would vanish (see Fig. 2.2). However, the steady-state values of p_2 and p_3 depend on the initial value, which means that the low-susceptibility axis of the particle is free to rotate within the plane that is perpendicular to the field direction. Thus, we call this situation one-dimensional alignment, since only one major axis of the oblate spheroid is aligned with the magnetic field.

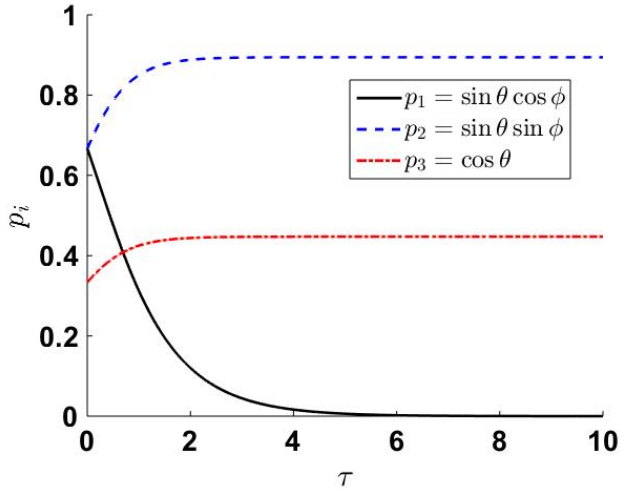

Figure 2.2: Evolution of p_1, p_2, and p_3 in constant field. The initial value for $\mathbf{p}$ is set to be $\left(\frac{2}{3}, \frac{2}{3}, \frac{1}{3}\right)$. Thus, p_1 goes to zero regardless of its initial value, since the field is pointing to the direction of 1. The steady-state values of p_2 and p_3 depend on the initial values.

2.4.2 Rotating Field Solution, $\xi > 0$

The detailed derivations of the solutions of Eqs. (2.17a) and (2.17b) with $\xi > 0$ are provided in Appendix A.3.

Case $\xi < 1$

If $\xi < 1$, the observed field frequency, 2ω, is smaller than the intrinsic frequency, AB^2, which can be achieved by making the field rotate slowly or by increasing the

field strength. The solution of Eqs. (2.17a) and (2.17b) for $\xi < 1$ is

$$\log\left[\frac{\tan\theta}{\tan\theta_0}\right] = -\frac{\tau}{2} + \frac{1}{2}\log\left[\frac{\sinh^2\Pi}{\sinh^2\Pi_0}\left(\frac{\xi^2 + \left[\sqrt{1-\xi^2}\coth\Pi + 1\right]^2}{\xi^2 + \left[\sqrt{1-\xi^2}\coth\Pi_0 + 1\right]^2}\right)\right] \tag{2.21}$$

where

$$\Pi = \frac{1}{2}\log\left[\frac{-\xi\tan u + 1 - \sqrt{1-\xi^2}}{-\xi\tan u + 1 + \sqrt{1-\xi^2}}\right], \tag{2.22a}$$

$$\Pi_0 = \frac{1}{2}\log\left[\frac{-\xi\tan u_0 + 1 - \sqrt{1-\xi^2}}{-\xi\tan u_0 + 1 + \sqrt{1-\xi^2}}\right], \text{ and} \tag{2.22b}$$

$$\Pi = \frac{\sqrt{1-\xi^2}}{2}\tau + \Pi_0. \tag{2.22c}$$

The change of the orientation vector $\mathbf{p}$ is shown in Fig. 2.3 for $\xi = 0.5$ with an initial orientation of $\varphi_0 = \frac{\pi}{4}$, and $\cos\theta_0 = 1 \times 10^{-4}$. Fig. 2.3(a) showing the top view along the 3-direction which is perpendicular to the plane of the rotating field, plots the trajectory of the orientation vector, showing that p_1 and p_2 slowly vanish. Fig. 2.3(b) and (c) plot the side view (along the 1- and 2- directions, respectively) of the trajectory, showing that p_3 limits to unity while p_1 and p_2 vanish. Fig. 2.3(d) plots the change of p_3 with respect to time τ, showing that p_3 goes to unit at steady-state, implying that the particle is aligned into the plane of the rotating field.

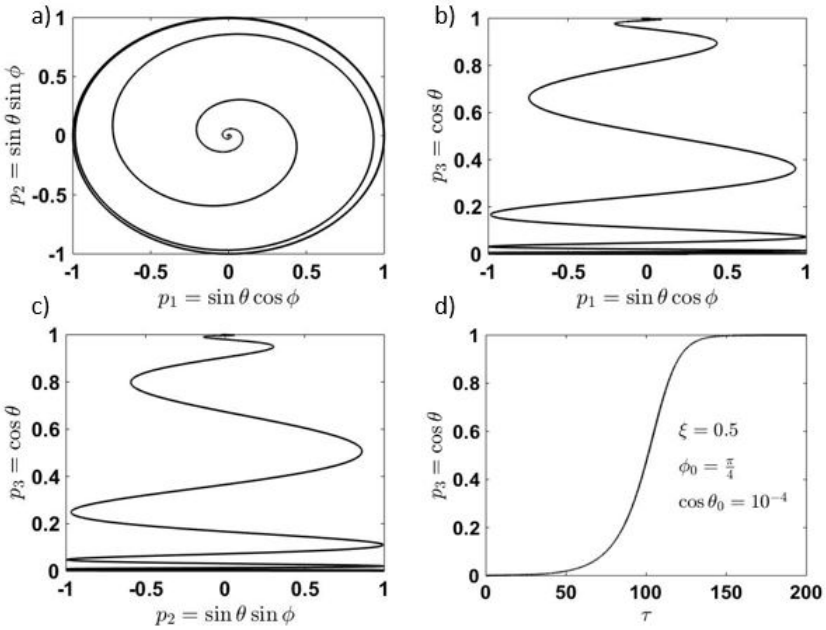

Figure 2.3: Evolution of orientation vector $\mathbf{p}$ at $\xi = 0.5$. **(a)** View perpendicular to the rotating field. The spiral trajectory shows that p_1 and p_2 slowly limit to 0. **(b), (c)** View parallel to the rotating field. At steady state, both p_1 and p_2 vanish, and p_3 limits to 1. **(d)** Change of p_3 with respect to τ. In long time p_3 slowly limits to 1.

Case $\xi = 1$

If $\xi = 1$, the observed field frequency, 2ω, is equal to the intrinsic frequency, AB^2. The solution to Eqs. (2.17a) and (2.17b) for $\xi = 1$ is

$$\log\left[\frac{\tan\theta}{\tan\theta_0}\right] = -\frac{\tau}{2} + \frac{1}{2}\log\left[\frac{2\Lambda^2 + 2\Lambda + 1}{2\Lambda_0^2 + 2\Lambda_0 + 1}\right], \tag{2.23}$$

where

$$\Lambda = \frac{1}{\cot u - 1}, \tag{2.24a}$$

$$\Lambda_0 = \frac{1}{\cot u_0 - 1}, \text{ and} \tag{2.24b}$$

$$\Lambda = -\frac{\tau}{2} + \Lambda_0. \tag{2.24c}$$

The $\xi = 1$ case occurs only when the observed field frequency is identical to the intrinsic frequency, making it an unstable case.

Case $\xi > 1$

If $\xi > 1$, the observed field frequency, 2ω, is larger than the intrinsic frequency., AB^2, which can be obtained either by making the field rotate faster than that the particle respond to the field or by decreasing the field strength B. The solution to

Eqs. (2.17a) and (2.17b) for $\xi > 1$ is

$$\log\left[\frac{\tan\theta}{\tan\theta_0}\right] = -\frac{\tau}{2} + \frac{1}{2}\log\left[\frac{\cos^2 K}{\cos^2 K_0}\left(\frac{\xi^2 + \left[\sqrt{\xi^2-1}\tan K - 1\right]^2}{\xi^2 + \left[\sqrt{\xi^2-1}\tan K_0 - 1\right]^2}\right)\right], \quad (2.25)$$

where

$$K = \arctan\left[\frac{1-\xi\tan u}{\sqrt{\xi^2-1}}\right], \quad (2.26a)$$

$$K_0 = \arctan\left[\frac{1-\xi\tan u_0}{\sqrt{\xi^2-1}}\right], \text{ and} \quad (2.26b)$$

$$K = \frac{\sqrt{\xi^2-1}}{2}\tau + K_0. \quad (2.26c)$$

The change of the orientation vector, $\mathbf{p}$, is shown in Fig. 2.4 for $\xi = 2$ with an initial orientation of $\varphi_0 = \frac{\pi}{4}$, $\cos\theta_0 = 1 \times 10^{-4}$. At $\xi = 2$, the field rotates faster than the particle is able to respond. Thus, the particle appreas to "wobble" in response to the rotating field, and the trajectories of p_1 and p_2 are not smooth, creating velocities that appear discontinuous in Fig. 2.4(a) - (c) and plateaus in Fig. 2.4(d). These characteristics are in direct contrast to the trajectories in Fig. 2.3; however, the overall trend of p_3 in both cases is monotonically limiting to unity.

In each of the three cases, the values of u and θ are calculated using the initial value of the azimuthal angle, u_0 (which is equal to φ_0). For the case of $\xi < 1$, u_0 is substituted into Eq. (2.22b) to calculate $\mathit{\Pi}_0$. Then, at a given time τ, the value of $\mathit{\Pi}$ can be found using Eq. (2.22c). With the knowledge of $\mathit{\Pi}$, at any given

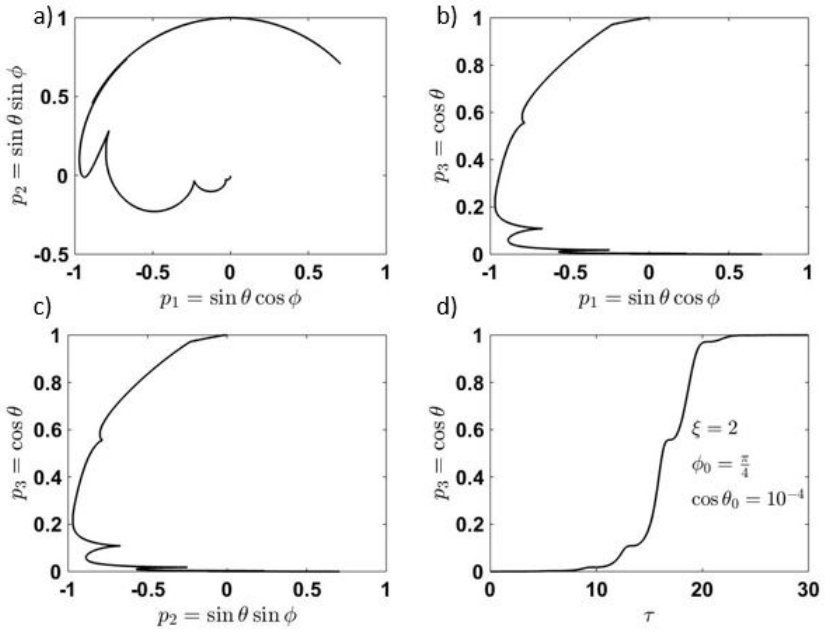

Figure 2.4: Evolution of orientation vector $\mathbf{p}$ at $\xi = 2$. **(a)** View perpendicular to the rotating field. The shorter trajectory shows that p_1 and p_2 rapidly limit to 0. **(b), (c)** View parallel to the rotating field. At steady state, both p_1 and p_2 vanish, and p_3 limits to 1. **(d)** Change of p_3 with respect to τ. In long time p_3 rapidly limits to 1.

time, the values of $u(\varphi)$ and θ can be found by solving Eqs. (2.22a) and (2.21) respectively. Similar processes can be followed to find u and θ for the cases $\xi = 1$ and $\xi > 1$.

2.5 Asymptotic Solution

Though complete, the solution derived in Section 2.4 are cumbersome to implement, disguising the simplicity of the effect of ξ on the alignment time. Simplified expressions would be more manageable for implementation into industrial settings. Thus, in an attempt to make the solutions more tractable, asymptotic expressions are derived for the two limiting cases of ξ as visualized in Fig. 2.5.

2.5.1 Case $\xi \ll 1$

The full solution for $\xi < 1$, Eq. 2.21, can be rewritten in terms of exponentials to ease the asymptotics, such that

$$\frac{\tan\theta}{\tan\theta_0} = \left[\Gamma_1 + \Gamma_2 + \Gamma_3\right]^{1/2}, \tag{2.27}$$

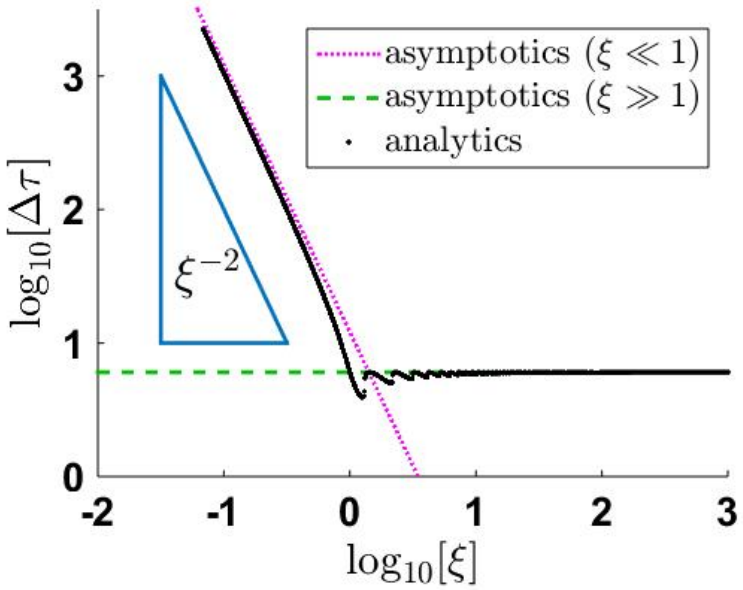

Figure 2.5: The alignment time, $\Delta\tau$, chosen from $p_3 = 0.1$ to $p_3 = 0.9$ versus ξ from both analytics and asymptotics. Asymptotic expansions show that $\Delta\tau$ scales as ξ^{-2} at $\xi \ll 1$ and $\Delta\tau$ scales as ξ^0 at $\xi \gg 1$.

where

$$\Gamma_1 = \left(\frac{\lambda_2 + \lambda_0 - 2\xi\lambda_1}{1-\xi^2} + \frac{\lambda_2 - \lambda_0}{\sqrt{1-\xi^2}} \right) \frac{\exp\left[-\tau\left(1-\sqrt{1-\xi^2}\right)\right]}{2}, \tag{2.28a}$$

$$\Gamma_2 = \left(\frac{\lambda_2 + \lambda_0 - 2\xi\lambda_1}{1-\xi^2} + \frac{\lambda_0 - \lambda_2}{\sqrt{1-\xi^2}} \right) \frac{\exp\left[-\tau\left(1-\sqrt{1+\xi^2}\right)\right]}{2}, \text{ and} \tag{2.28b}$$

$$\Gamma_3 = \left(\frac{2\lambda_1\xi}{1-\xi^2} - \frac{\xi^2}{1-\xi^2} \right) \exp\left[-\tau\right], \tag{2.28c}$$

such that

$$\lambda_0 = \frac{1}{1+\tan^2\varphi_0}, \tag{2.29a}$$

$$\lambda_1 = \frac{\tan\varphi_0}{1+\tan^2\varphi_0}, \text{ and} \tag{2.29b}$$

$$\lambda_2 = \frac{\tan^2\varphi_0}{1+\tan^2\varphi_0}. \tag{2.29c}$$

As $\xi \to 1$, Γ_2 and Γ_3 decay much faster than Γ_1, and at long time, $\Gamma_1 \gg \Gamma_2$, Γ_3. Thus, the leading-order Taylor expansions of each of the Γ-terms results in the following simplification for Eq. (2.27) (details provided in Appendix A.4), where

$$\frac{\tan\theta}{\tan\theta_0} = \left[\lambda_2 \exp\left[-\frac{\xi^2\tau}{2} \right] \right]^{1/2}. \tag{2.30}$$

By taking the limit of Eq. (2.27) as $\xi \to 0$, the constant field solutions are recovered, confirming the low-ξ asymptotic solution.

2.5.2 Case $\xi \gg 1$

If the magnetic field rotates much faster than the particle can respond ($\xi \gg 1$), the long-term response dominates. Starting with Eq. (2.17a),

$$\frac{du}{d\tau} \approx -\frac{\xi}{2}, \tag{2.31}$$

since $\xi \gg \sin 2u$. This equation can be solved easily such that

$$u = \varphi_0 - \frac{\xi\tau}{2}, \tag{2.32}$$

where φ_0 (the initial azimuthal angle) is equal to u_0 (the initial phase shift) by Eq. (2.16). Also, from Eq. (2.16), the expression

$$\varphi = \varphi_0 \tag{2.33}$$

is a straighforward result, which means, at high ξ, the azimuthal angle does not change. Substituting Eq. (2.32) into Eq. (2.17b) gives the following differential equation for the alignment

$$\frac{d\theta}{d\tau} = -\frac{1}{2}\sin 2\theta \cos^2\left[\varphi_0 - \frac{\xi\tau}{2}\right]. \tag{2.34}$$

Separating the variables and integrating this expression gives

$$\frac{\tan\theta}{\tan\theta_0} = \exp\left[-\frac{\tau}{2} + \frac{\varphi_0}{\xi} + \frac{\sin\left[2\varphi_0 - \xi\tau\right]}{\xi}\right] \tag{2.35}$$

which can be further simplified by assuming $\xi \to \infty$, such that

$$\frac{\tan\theta}{\tan\theta_0} = \exp\left[-\frac{\tau}{2}\right]. \tag{2.36}$$

The solution in Eq. (2.36), derived rigorously here, is consistent with the work of Kimura [28].

2.6 Results and Discussion

We can analyze the φ-motion without solving the Eq. (2.17a) by using the *stability analysis*. The motion of φ will have *phase-locked* and/or *phase-ejected* states depending on the value of ξ and initial condition. The details can be found in the Appendix A.5, while this section will concentrate on analyzing the analytics and the θ-motion since the full alignment is indicated by the change of θ.

In the constant-field solution, if we shift the dimensionless time by a factor of $(-\log\bar{p})$, Eq. (2.20a) becomes

$$p_1 = \sqrt{\frac{1}{1+\exp\left[2\tau\right]}}, \tag{2.37}$$

which is independent of the initial value of p_1. This result indicates that the particle follows the same alignment path for any initial condition, which is consistent with general Stokes flow principles.

For $\xi < 1$, separate short-term and long-term responses are noticeable, resulting from motion of φ_0 and θ_0. If $\theta_0 < \frac{\pi}{2} - \varphi_0$, the shortest path to alignment is in the θ-direction, and a separate short-term response is seen as a quick θ-motion, as visualized in trajectories for $\varphi_0 = 0$ and $\varphi_0 = \frac{\pi}{4}$ in Fig. 2.6. After the major axis of spheroid is locked into position with the field, the long-term response proceeds to align the easy plane over a significantly longer time. If $\theta_0 > \frac{\pi}{2} - \varphi_0$, the short-term response will be in the azimuthal φ-direction, and no quick alignment motion will be observed (viz., the $\left(\varphi_0 = \frac{\pi}{2}\right)$-case in Fig. 2.6).

For $\xi > 1$, the field rotates so fast that it can be approximated as a planar field, and only the long-term hydrodynamic response will be present. As derived in Eq. (2.36), the evolution of p_3 becomes independent of ξ and φ_0 as ξ grows large, as visualized in Fig. 2.7, where the solutions collapse into a single trajectory. In Fig. 2.7, when $\xi = 10$, the particle "wobbles", as previously discussed, while it attempts to move with the field. When $\xi = 10^3$, the field rotates so fast that the particle experiences the effects of the field in all directions, making the major axis always aligned regardless of φ_0.

To enable comparisons to experiments, an alignment time, $\Delta\tau$, is chosen arbitrarily to be the difference in times as the particle aligns from a starting orientation $p_3^{(1)}$

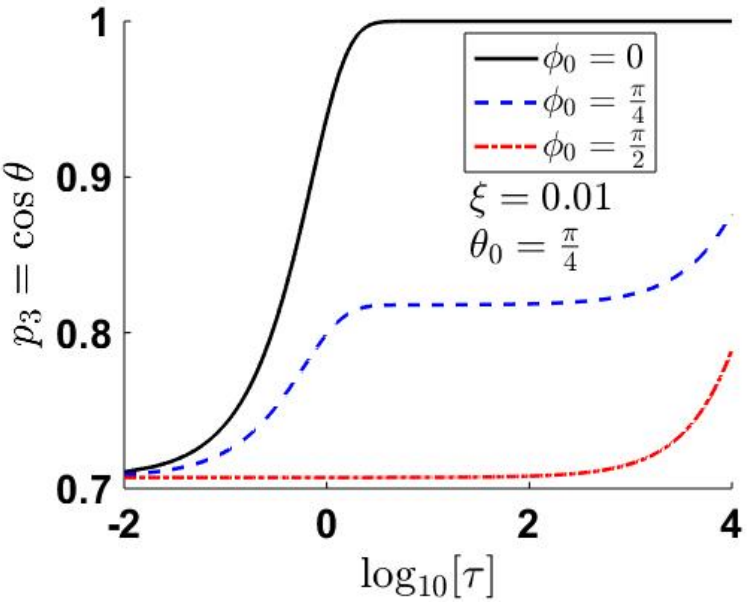

Figure 2.6: The evolution of p_3 at $\xi = 0.01$ with $\theta_0 = \frac{\pi}{4}$ for $\phi_0 \in \left\{0, \frac{\pi}{4}, \frac{\pi}{2}\right\}$. A short-term response of θ-motion can be observed for the $\phi_0 = 0$ and $\frac{\pi}{4}$ cases. All cases limit to unity in long time.

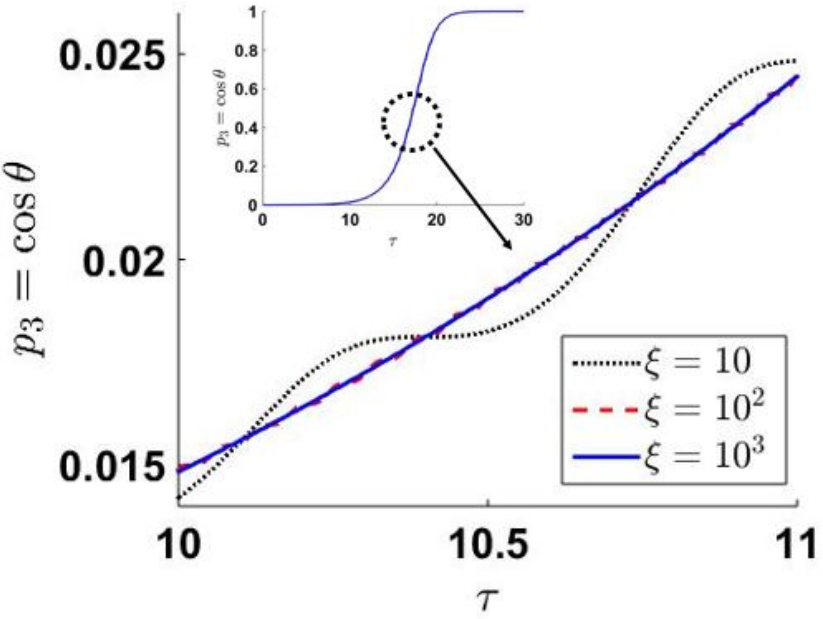

Figure 2.7: Evolution of p_3 in rotating field at different $\xi > 1$ with $\phi_0 = 0$. At $\xi = 10$ (the black dotted line), the microdisk wobbles to follow the field. At $\xi = 100$ and $\xi = 1000$ (red dashed and blue solid lines, respectively), the microdisk "sees" the field as a planar field, and the solutions collapse.

to a final orientation p_3^2, where the alignment is considered to be complete, such that

$$\Delta\tau = \tau\left(p_3^{(2)}\right) - \tau\left(p_3^{(1)}\right). \tag{2.38}$$

From the asymptotic solution for $\xi \ll 1$, Eq. (2.30), the alignment time is

$$\Delta\tau = \frac{-2}{\xi^2}\log\left[\frac{\tan^2\theta_2}{\tan^2\theta_1}\right], \tag{2.39}$$

which scales as ξ^{-2}. For the $\xi \gg 1$ case, the alignment time is

$$\Delta\tau = -2\log\left[\frac{\tan\theta_2}{\tan\theta_1}\right], \tag{2.40}$$

which is constant for any chosen set of θ_1 and θ_2.

In this work, $p_3^{(1)}$ is chosen to be 0.1, and $p_3^{(2)}$ is chosen to be 0.9. A cartoon representation of this alignment time can be seen in Fig. 2.8. In Fig. 2.9, the alignment time is plotted as a function of dimensionless frequency, ξ. The alignment time obtained from the analytic solution at low-ξ limit appears to scale as ξ^{-2} and at high-ξ limit appears to scale as ξ^0, which is validated by the asymptotic solutions. Furthermore, we plot the experimental results on top of the analytics and asymptotics, and the results confirm this theory.

The high-ξ condition (practically larger than a value of 20) can provide a precise control of the experiments and minimize the control parameters (e.g., φ_0). Since $\tau = AB^2t$, at high ξ, where $\Delta\tau$ is a contant, the processing alignment time Δt

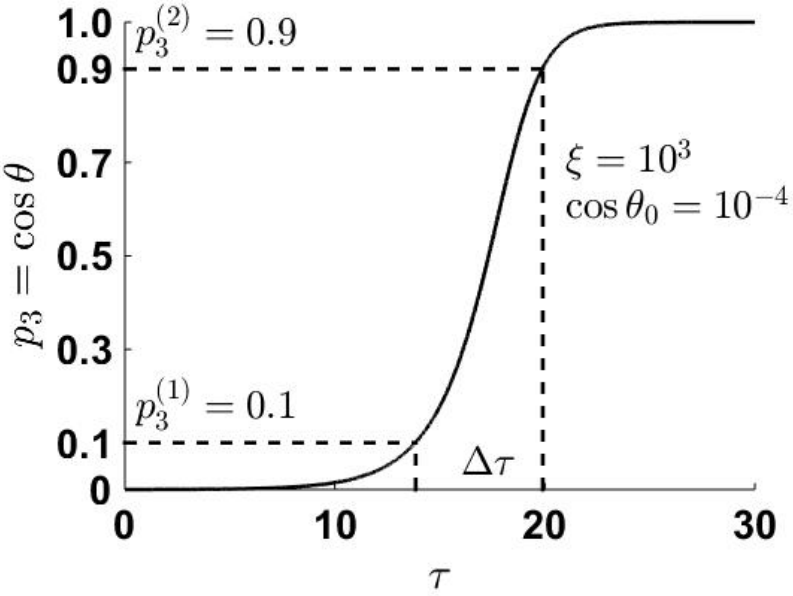

Figure 2.8: The alignment time, $\Delta\tau$, is chosen to be time from $p_3^{(1)} = 0.1$ to $p_3^{(2)} = 0.9$.

scales linearly with $1/B^2$. Although the model is based on single-particle dynamics, where the experimental data are collected from very samples (0.001 vol.%), the high-ξ limit also agrees with higher-volume-fraction (0.1 vol.%) samples shown in previous work [19].

Beyond predicting single-particle dynamics, the model developed here can be used as a first-order approximation to predict the probability of alignment in a multi-particle system where particle-particle interaction is negligible. Suppose that the initial orientations of the particles follow a uniform probability distribution on the surface of a unit hemisphere. For a given definition of the alignment time $\Delta\tau$, the probability that the particles are aligned to or beyond the chosen final orientation

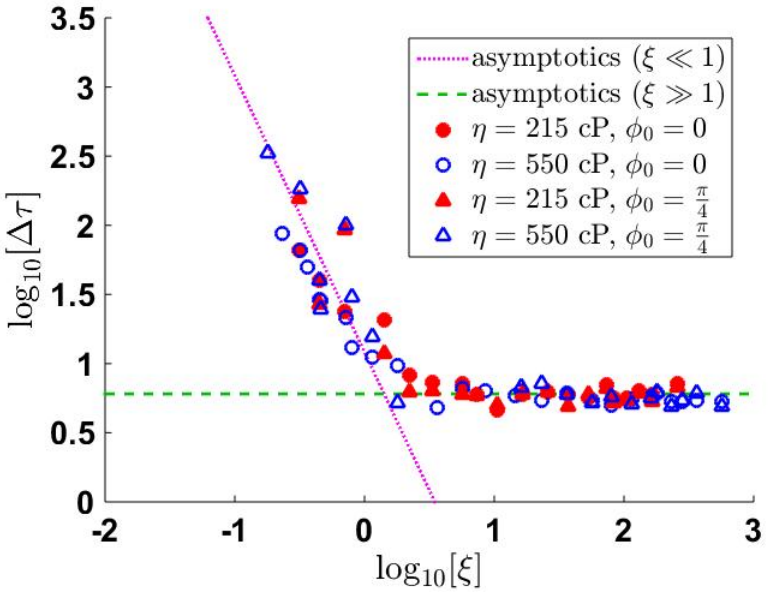

Figure 2.9: The alignment time, $\Delta\tau$, chosen from $p_3^{(1)} = 0.1$ to $p_3^{(2)} = 0.9$, versus dimensionless frequency ξ from both the asymptotic solutions and the experiments. At high ξ, the experiments show that the dimensionless alignment time is constant. At low ξ, the dimensionless alignment time grows with decreasing ξ, agreeing with the asymptotic expansion.

$p_3^{(2)}$ is

$$\mathbb{P} = \frac{\int_{\varphi=0}^{\varphi=2\pi} \int_{\theta=0}^{\theta=\arccos p_3^{(1)}} \sin\theta d\theta d\varphi}{\int_{\varphi=0}^{\varphi=2\pi} \int_{\theta=0}^{\theta=\pi/2} \sin\theta d\theta d\varphi} = 1 - p_3^{(1)}. \tag{2.41}$$

Thus, the particles whose initial orientation is smaller than the chosen $p_3^{(1)}$ are not considered to be aligned after $\Delta\tau$.

In addition to studying the dynamics, the rheological properties can also be predicted with the knowledge of the orientation of the particle. For a suspension of particles without hydrodynamic interactions, we can write the average stress such as

$$\langle \sigma_{ij} \rangle = -P\delta_{ij} + 2\eta E_{ij}^{\infty} + \frac{1}{V} \sum_{\alpha=1}^{N} S_{ij}^{\alpha}, \tag{2.42}$$

where $\langle \sigma_{ij} \rangle$ is the ensemble-averaged stress, P is the pressure, and S_{ij}^{α} is the *stresslet* of particle α. We can write the the stresslet, following Kim and Karrila [30], such that

$$S_{ij}^{\alpha} = \frac{20}{3}\pi\eta a^3 M_{ijk\ell}^{\alpha} E_{k\ell}^{\alpha} + \frac{20}{3}\pi\eta a^3 H_{ijk}^{\alpha} \left(\Omega_k^{\infty} - \omega_k\right), \tag{2.43}$$

where $M_{ijk\ell}^{\alpha}$ and H_{ijk}^{α} are the hydrodynamic tensors that depend on the configuration of the particle. At any time, $M_{ijk\ell}^{\alpha}$ and H_{ijk}^{α} can be calculated with the known orientation $\mathbf{p}$. Therefore, the *effective viscosity* can be calculated by dividing the average stress by shear rate.

We believe that variations in the experimental data result from the shape of the particle. In the model, we assumed an axisymmetric disk, but the microdisks produced for this investigation are not perfectly axisymmetric. If distortion from

axisymmetry is present, a second axis of orientation exists, and the particle will have a susceptibility to align this second orientation as well. The effect of an extra axis of orientation in the plane is observed in the experiments. After the microdisks are aligned into the field plane, they will continue to wobble in time with the rotatting field. Other possible sources of errors come from the assumptions of no random Brownian motion and no translational motion via sedimentation.

2.7 Conclusion

Although the alignment of anisotropic particles has been previously studied experimentally and theoretically, the full analytic solution to predict the orientation of magnetically susceptible microdisks under a rotating magnetic field is presented in this work for the first time. Good agreement with experimental results suggests that the model can be extended to composites with higher volume fraction of particle dispersion and smaller particle size. The model also provides a direction for optimizing the alignment process. In general, by keeping the dimensionless frequency, ξ, at a high value, the processing alignment time, Δt, can be reduced by increasing the field strength B.

Chapter 3

Coarsening of Magnetic Particles — Multiple Particle Dynamics

In Chapter 2, we neglect the magnetic and hydrodynamic interactions between particles. However, in practice, both interactions exist. The magnetic interaction prompts the formation of structures, e.g., one-dimensional structure in a constant field and two-dimensional structure in a dynamic field. The dynamic change of the structure depends on the hydrodynamic interactions between the particles. In this chapter, both the hydrodynamic and magnetic interactions will be discussed from

a fundamental point of view. We start our discussion with spherical suspensions and then move to aspherical particles.

3.1 Introduction

A suspension of magnetic particles, termed a magnetorheological (MR) fluid, can respond to an external field, and thus, the rheological properties can change drastically. As observed in our previous studies [29], sheets of magnetic microdisks are formed under a rotating magnetic field. In our studies, the particles have induced dipoles under an external magnetic field. The induced dipole, in turn, creates its own magnetic field that interacts with other dipoles, and this dipole-dipole interaction causes the particles to aggregate into different structures, depending on the volume fraction of the particles and the characteristic applied external field (e.g., magnitude, static versus dynamic). The development of these structures results in significant changes in flow behavior, as they restrict the motion of the fluid, thereby increasing the apparent viscosity of the complex fluids and transitioning the properties from a more fluid state to a more solid state.

Equilibrium properties have been investigated extensively in previous studies. A constant field induces the chaining of particles into one-dimensional structures, and Mohebi et al. [32] and Martin et al. [33] both reported two timescales in such a field. Columns of particles are formed parallel to the magnetic field on a short timescale, and aggregation of columns orthogonal to the magnetic field takes place

on a long timescale. Martin et al. [33] characterized the structures by studying the anisotropy of the conductivity. They observed a rise in anisotropy on the short timescale and a decrease in the anisotropy on the long timescale, and also a decrease in the anisotropy when the volume fraction of particles increases. Martin et al. [34] also reported a formation of hexagonal packing under rotating magnetic field, which is consistent with our observations [19]. Melle et al. [35] studied the formation of optically anisotropic chains under rotating magnetic field. They reported that the length of chains stays constant at low frequencies, while the chains break up at high frequencies. In these studies, the hydrodynamic interactions were not considered while modeling the dynamics. Bonnecaze and Brady [36] modeled the dynamics of electrorheological (ER) fluids, analogs of MR fluids, under static electrical fields. This work accurately simulates both the hydrodynamic and electrostatic interactions. The method used for modeling the hydrodynamic interactions is the same with the one used in this study, and we will discuss it in details later.

In these works, the suspending particles are spherical. In contrast to conventional MR fluids that contain spherical particles, MR fluids with anisotropic particles, such as fiber-shape particles, can generate increased rheological properties (e.g., yield stress) for the same volume fraction [37–39] and decreased sedimentation rate [37,40]. Kuzhir et al. [39] attributed the increase of yield stress to the increased anisotropy of the structure and the solid friction between fibers. Bell et al. [40] explained that the degree of entanglement of the fibers is the primary factor that is

responsible for the reduced sedimentation rate. Although these studies investigate the macrorheology of MR fluids with fibrous colloids, a theoretical investigation of the aggregation dynamics of anisotropic magnetic particles is very rare. The drag on an aspherical particle has orientational dependence [30, 41–43], and few studies have investigated their particle-particle interactions. Satoh and coworkers used a Monte Carlo method to simulate the aggregation of rod-like particles [44] and plate-like particles [45–48] under a uniform magnetic field. However, an appropriate way to describe the hydrodynamic interactions between and among anisotropic particles is lacking in these equilibrium studies.

Further, the effects of different magnetic-field configurations on structures that are composed of anisotropic particles needs to be investigated [49]. Melle et al. [35] studied the motion of a chain of particles under a rotating magnetic field. They reported that the chain length stays constant at low frequency, while the chain breaks at high frequency. Martin et al. [34] and Jäger and Klapp [50] have studied the structural evolution of samples with high volume fraction under rotating fields, finding that two-dimensional structures are formed where spheres are packed into hexagonal sheets that are periodically positioned in the direction perpendicular to the field plane. Yet, similar studies on rods and disks are lacking. Since the anisotropy of these particles also provides the microstructure for many composites with anisotropic macroscopic properties, a clear need for a micromechanical description exists as bulk materials will have properties that depend on the orientation of the particles.

The hydrodynamic interactions between particles depend on the configuration solely, making the simulations of dynamics of particles with complex geometries difficult. Because the hydrodynamic interactions among spheres have been well characterized [51–53], several studies have used methods of decomposing complex geometries into spheres while keeping them in a rigid or flexible manner. Meng and Higdon [54, 55] simulated plate-like particles that are composed of spheres under shear flow and studied the rheology of the suspensions. They used a rigid-body tensor that forces the spheres to move as a rigid body, and this method is also adopted in this study, which will be discussed later. Yamamoto and Matsuoka [56] studied suspension of fiber-like and plate-like particles with far-field hydrodynamic interactions considered. Yamanoi et al. used a similar method as Yamamoto's to simulate rigid [57–59] and flexible fibers [59, 60] and ring-like particles [61]. Kutteh [62,63] applied accurate hydrodynamic interactions to study the dynamics and rheology of particles that are made of spheres and prescribed constraint forces to keep the spheres in rigid bodies. Bertevas et al. [64] simulated the rheological properties of suspensions of *real* oblate spheroids. In this study, only two-particle interactions are considered, and the method proposed in this study is only able to simulate spheroids with moderate aspect ratio. They used "equivalent spheres" to calculate the interparticle distance when calculating the lubrication interactions, but for spheroids with small or large aspect ratios, the surface fails to be approximated as spheres.

3.2 Elements of Hydrodynamic Interactions

The goal of this section is to introduce the fundamentals of hydrodynamic interactions between particles. We start with the classical problem — Stokes flow, and after a detailed discussion and some mathematical derivations, we will introduce the method that is used in this study to model the hydrodynamic interactions.

The system that is investigated in this study has a trivial Reynolds number ($Re \to 0$), so we are solving the Stokes equations. We start with Navier-Stokes equations

$$\rho\left(\frac{\partial u_i}{\partial t} + u_j\frac{\partial u_i}{\partial x_j}\right) = -\frac{\partial p}{\partial x_i} + \eta\frac{\partial^2 u_i}{\partial x_k \partial x_k}. \tag{3.1}$$

Navier-Stokes equations can be non-dimensionalized by choosing appropriate parameters, and the dimensionless form of Navier-Stokes equation is

$$Re\left(\frac{\partial u_i}{\partial t} + u_j\frac{\partial u_i}{\partial x_j}\right) = -\frac{\partial p}{\partial x_i} + \frac{\partial^2 u_i}{\partial x_k \partial x_k}, \tag{3.2}$$

where Re is the Reynolds number such that

$$Re = \frac{\rho U a}{\eta}. \tag{3.3}$$

This study focuses on a system microscopically; thus, Reynolds number can be

assumed to be negligible. Therefore, we will solve the Stokes equations:

$$\eta \frac{\partial^2 u_i}{\partial x_k \partial x_k} - \frac{\partial p}{\partial x_i} = 0, \text{ and} \tag{3.4a}$$

$$\frac{\partial u_i}{\partial x_i} = 0. \tag{3.4b}$$

Two main methods of solving Stokes' equations exist. One solves the problem in terms of eigenfunction expansions or vector harmonic functions, which is typically introduced in a graduate-level fluid dynamics class. The other one is based on the *fundamental* solution, which will be discussed in details in this study.

First, take a look at the classic problem – a uniform flow past a fixed sphere. It can be solved by harmonic functions (see details in Leal's book [65]), and the solution is

$$u_i - u_i^\infty = -\left(\frac{3}{4}\frac{a}{r} + \frac{1}{4}\frac{a^3}{r^3}\right) u_i^\infty - \left(\frac{3}{4}\frac{a}{r^3} - \frac{3}{4}\frac{a^3}{r^5}\right) x_k u_k^\infty x_i, \text{ and} \tag{3.5a}$$

$$p = -\frac{3a\eta}{2}\frac{u_k^\infty x_k}{r^3}. \tag{3.5b}$$

The drag, an integral of stress on the surface, on the sphere can be found to be

$$F_i = 6\pi a \eta u_i^\infty, \tag{3.6}$$

which is the well-known *Stokes law*. The same result can be derived by a funda-

mental solution which will be shown later. This study focuses on the fundamental solution which provides a base for constructing the numerical methods that will be introduced later.

3.2.1 A Fundamental Solution of Stokes Flow

Suppose that a point force, f_i, is imposed on the fluid at the origin. We can write the Stokes equations such that

$$\eta \frac{\partial^2 u_i}{\partial x_k \partial x_k} - \frac{\partial p}{\partial x_i} = f_i \delta(\mathbf{x}). \tag{3.7}$$

The velocity can be written as the product of a second-order tensor and the point force, and the pressure can be written as the product of a first-order tensor and the point force, following Kim and Karrila [30], such that

$$u_i = \frac{1}{8\pi\eta} J_{ij} f_j, \text{ and} \tag{3.8a}$$

$$p = \frac{1}{8\pi\eta} \mathscr{P}_j f_j, \tag{3.8b}$$

where

$$J_{ij} = \frac{\delta_{ij}}{r} + \frac{x_i x_j}{r^3}, \tag{3.9}$$

is called the *stokeslet*, and the corresponding pressure tensor $\mathscr{P}_j$ is

$$\mathscr{P}_j = 2\eta \frac{x_j}{r^3} + \mathscr{P}_j^{\infty}. \tag{3.10}$$

The corresponding stress tensor $\boldsymbol{\sigma}$ is

$$\begin{aligned}\sigma_{ij} &= -p\delta_{ij} + 2\eta E_{ij} \\ &= -\frac{3f_k x_k x_i x_j}{4\pi r^{10}},\end{aligned} \tag{3.11}$$

where E_{ij} is the rate-of-strain tensor such that

$$E_{ij} = \frac{1}{2}\left(\frac{\partial u_i}{\partial x_j} + \frac{\partial u_j}{\partial x_i}\right). \tag{3.12}$$

The rate-of-strain tensor is a symmetric second-order tensor with zero trace, $E_{ii} = 0$, due to the incompressibility of the fluid.

We will start with this form of the solution and develop the formulas for hydrodynamic interactions.

3.2.2 Lorentz Reciprocal Theorem

Suppose that $\mathbf{u}$ and $\mathbf{u}'$ represent the velocity fields that satisfy the Stokes flow that pass the same body with surface ∂D; and $\boldsymbol{\sigma}$ and let $\boldsymbol{\sigma}'$ be the corresponding stress fields. We calculate the following quantity $\boldsymbol{\sigma} : \mathbf{E}'$ and obtain that

$$\begin{aligned}\sigma_{ij}E'_{ij} &= \left(-p\delta_{ij} + 2\eta E_{ij}\right) E'_{ij} \\ &= 2\eta E_{ij}E'_{ij},\end{aligned} \tag{3.13}$$

since E'_{ij} is traceless. If we switch the roles of the primed and unprimed terms, we can obtain that

$$\sigma_{ij}E'_{ij} = \sigma'_{ij}E_{ij}. \tag{3.14}$$

Consider the calculation of $\boldsymbol{\sigma} : \mathbf{E}'$ that

$$\begin{aligned}\sigma_{ij}E'_{ij} &= \frac{1}{2}\sigma_{ij}\frac{\partial u'_i}{\partial x_j} + \frac{1}{2}\sigma_{ij}\frac{\partial u'_j}{\partial x_i} \\ &= \sigma_{ij}\frac{\partial u'_i}{\partial x_j} \\ &= \frac{\partial}{\partial x_j}\left(\sigma_{ij}u'_i\right) - \left(\frac{\partial \sigma_{ij}}{\partial x_j}\right)u'_i.\end{aligned} \tag{3.15}$$

In a similar manner, we can write

$$\sigma'_{ij}E_{ij} = \frac{\partial}{\partial x_j}\left(\sigma'_{ij}u_i\right) - \left(\frac{\partial \sigma'_{ij}}{\partial x_j}\right)u_i. \tag{3.16}$$

Substituting into Eq. (3.14), we have

$$\frac{\partial}{\partial x_j}\left(\sigma_{ij}u'_i\right) - \left(\frac{\partial \sigma_{ij}}{\partial x_j}\right)u'_i = \frac{\partial}{\partial x_j}\left(\sigma'_{ij}u_i\right) - \left(\frac{\partial \sigma'_{ij}}{\partial x_j}\right)u_i \tag{3.17}$$

Now integrating Eq. (3.17) over an infinite fluid region with volume V outside the body ∂D and applying *divergence theorem* yields the *Lorentz reciprocal theorem*:

$$\oint_{\partial D}\mathbf{u}'\cdot(\boldsymbol{\sigma}\cdot\mathbf{n})\,dS - \int\mathbf{u}'\cdot(\boldsymbol{\nabla}\cdot\boldsymbol{\sigma})\,dV = \oint_{\partial D}\mathbf{u}\cdot(\boldsymbol{\sigma}'\cdot\mathbf{n})\,dS - \int\mathbf{u}\cdot(\boldsymbol{\nabla}\cdot\boldsymbol{\sigma}')\,dV. \tag{3.18}$$

The conditions imposed by the Stokes flow require that $\boldsymbol{\nabla} \cdot \boldsymbol{\sigma} = 0$ and $\boldsymbol{\nabla} \cdot \boldsymbol{\sigma}' = 0$, and we have another form of the Lorentz reciprocal theorem such that

$$\oint_{\partial D} \mathbf{u}' \cdot (\boldsymbol{\sigma} \cdot \mathbf{n})\, dS = \oint_{\partial D} \mathbf{u} \cdot (\boldsymbol{\sigma}' \cdot \mathbf{n})\, dS. \tag{3.19}$$

3.2.3 An Integral Representation Solution

The integral representation for the solution of Stokes flow represents the velocity field at any point in the fluid domain in terms of the force distribution on the boundaries. The integral representation is the result of a direct application of the Lorentz reciprocal theorem.

Consider a fluid domain separated by a surface ∂D at position $\mathbf{y}$. Suppose that $\mathbf{u}$ is the solution of the Stokes flow, and $\mathbf{u}'$ is the solution of the Stokes flow subject to a point force, $\mathbf{u}' = \frac{1}{8\pi\eta}\mathbf{J}(\mathbf{x}-\mathbf{y}) \cdot \mathbf{f}$. Thus, the stress fields satisfy that $\boldsymbol{\nabla} \cdot \boldsymbol{\sigma} = 0$ and $\boldsymbol{\nabla} \cdot \boldsymbol{\sigma} = \mathbf{f}\delta(\mathbf{x}-\mathbf{y})$. Substituting the velocity and stress fields into Eq. (3.18) gives

$$\begin{aligned} u_i(\mathbf{x}) - u_i^{\infty}(\mathbf{x}) = &-\frac{1}{8\pi\eta} \int_{\partial D} \left(\frac{\delta_{ij}}{r} + \frac{(x_i - y_i)\,(x_j - y_j)}{r^3} \right) f_j\,(\mathbf{y}) \\ &+ \frac{3}{4\pi} \int_{\partial D} \frac{(x_i - y_i)\,(x_j - y_j)\,(x_k - y_k)}{r^5} u_j n_k, \end{aligned} \tag{3.20}$$

and the corresponding pressure field is

$$p(\mathbf{x}) = \frac{1}{4\pi}\int_{\partial D}\frac{(x_j - y_j)}{r^3}f_j(\mathbf{y})dS + \frac{1}{2\pi}\int_{\partial D}\left\{\frac{\delta_{ij}}{r} - \frac{3(x_i - y_i)(x_j - y_j)}{r^3}\right\}u_i n_j dS. \tag{3.21}$$

The first integral on the RHS of Eq. (3.20) is termed as the *single-layer potential*, and the second integral is termed the *double-layer potential* by an analogy with the point charge distribution on a surface in electrostatics. The integral representation solution provides a base for the method called the *boundary-integral method*. The integral representation does not provide solutions to a specific problem unless the tractions, f_j, on the surface are known. However, it provides a flexible method in numerical studies since the boundary ∂D is an arbitrary surface, rigid or flexible with any geometry.

If the boundary ∂D represents the surface of a solid-body, then at the boundary the no-slip boundary condition requires that $\mathbf{u}(\mathbf{y}) = \mathbf{U}^{\alpha} + \boldsymbol{\Omega}^{\alpha} \times \mathbf{y}$. After some derivations, we can show that for a solid boundary the double-layer potential vanishes, and the integral representation solution becomes

$$\begin{aligned} u_i(\mathbf{x}) - u_i^{\infty}(\mathbf{x}) &= -\frac{1}{8\pi\eta}\int_{\partial D}\left\{\frac{\delta_{ij}}{r} + \frac{(x_i - y_i)(x_j - y_j)}{r^3}\right\}f_j(\mathbf{y})\,dS \\ &= -\frac{1}{8\pi\eta}\int_{\partial D} J_{ij}(\mathbf{x} - \mathbf{y})\,f_j(\mathbf{y})\,dS. \end{aligned} \tag{3.22}$$

If more than one particle are suspended in the fluid, we can write the disturbance velocity field as the summation of the single-layer potential because of the linearity of Stokes flow such that

$$u_i(\mathbf{x}) - u_i^{\infty}(\mathbf{x}) = -\frac{1}{8\pi\eta}\sum_{\alpha=1}^{N}\int_{\partial D} J_{ij}(\mathbf{x}-\mathbf{y})\, f_j^{\alpha}(\mathbf{y})\, dS. \tag{3.23}$$

We start with Eq. (3.23) to derive the *far-field* hydrodynamic interactions among particles.

3.2.4 The Multipole Expansion

Given the exact knowledge of the tractions on the surfaces of the particles, Eq. (3.23) is an accurate representation of the velocity field. However, the tractions are not known in most cases, especially for complex geometries. Instead of solving Eq. (3.22) or (3.23), we expand the stokeslet, J_{ij}, in a Taylor series about the center, $\mathbf{x}^{\alpha}$, of each particle

$$\begin{aligned} J_{ij}(\mathbf{x}-\mathbf{y}) &= \sum_{n=0}^{\infty}\frac{1}{n!}\left[(\mathbf{x}-\mathbf{y})\cdot\boldsymbol{\nabla}_{\mathbf{y}}\right]^n J_{ij}(\mathbf{x}-\mathbf{y})\big|_{\mathbf{y}=\mathbf{x}^{\alpha}} \\ &= \sum_{n=0}^{\infty}\frac{(-1)^n}{n!}\left(x_{k_1}^{\alpha}-y_{k_1}\right)\ldots\left(x_{k_n}^{\alpha}-y_{k_n}\right) J_{ij,k_1\ldots k_n}. \end{aligned} \tag{3.24}$$

Substituting the expansion into Eq. (3.23) yields

$$u_i(\mathbf{x}) - u_i^{\infty}(\mathbf{x}) = \frac{1}{8\pi\eta}\sum_{\alpha=1}^{N}\sum_{n=0}^{\infty}\frac{(-1)^n}{n!} J_{ij,k_1\ldots k_n} Q_{jk_1\ldots k_n}^{\alpha}, \tag{3.25}$$

where $Q_{jk_1\ldots k_n}$ is the nth multipole moment of particle α such that,

$$Q^{\alpha}_{jk_1\ldots k_n} = -\int_{\partial D} \left(y_{k_1} - x^{\alpha}_{k_1}\right)\ldots\left(y_{k_n} - x^{\alpha}_{k_n}\right) f^{\alpha}_{j} dS. \tag{3.26}$$

Substituting the multipole moment into Eq. (3.25) gives

$$\begin{aligned} u_i\left(\mathbf{x}\right) - u^{\infty}_i\left(\mathbf{x}\right) = \frac{1}{8\pi\eta}\sum_{\alpha=1}^{N}\{\, & J_{ij}\left(\mathbf{x}-\mathbf{x}^{\alpha}\right) Q^{\alpha}_{j} \\ & + J_{ij,k_1}\left(\mathbf{x}-\mathbf{x}^{\alpha}\right) Q^{\alpha}_{jk_1} \\ & + \frac{1}{2} J_{ij,k_1k_2}\left(\mathbf{x}-\mathbf{x}^{\alpha}\right) Q^{\alpha}_{jk_1k_2} \\ & + \frac{1}{6} J_{ij,k_1k_2k_3}\left(\mathbf{x}-\mathbf{x}^{\alpha}\right) Q^{\alpha}_{jk_1k_2k_3} \\ & + \ldots\,\}\,. \end{aligned}$$

The zeroth moment or *monopole*, Q_j , corresponds to the total force on the particle such that

$$F^{\alpha}_{j} = Q^{\alpha}_{j} = -\int_{\partial D} f^{\alpha}_{j} dS. \tag{3.27}$$

The first moment or *dipole* can be decomposed into symmetric and antisymmetric parts.

The symmetric part corresponds to the *stresslet* and the antisymmetric part cor-

responds to the torque such that,

$$S_{jk}^{\alpha} = -\frac{1}{2}\int_{\partial D}\left\{\left(y_j - x_j^{\alpha}\right) f_k^{\alpha} + \left(y_k - x_k^{\alpha}\right) f_j^{\alpha} - \frac{2}{3}\delta_{jk}\left(y_\ell - x_\ell^{\alpha}\right) f_\ell^{\alpha}\right\} dS, \text{ and} \tag{3.28a}$$

$$T_{jk}^{\alpha} = -\frac{1}{2}\int_{\partial D}\left\{\left(y_j - x_j^{\alpha}\right) f_k^{\alpha} - \left(y_k - x_k^{\alpha}\right) f_j^{\alpha}\right\} dS, \tag{3.28b}$$

where the isotropic part is excluded from the stresslet as it has no influence on the flow of fluids, and the rotlet can be interpreted as the torque on the particle such as

$$T_{jk}^{\alpha} = \varepsilon_{jk\ell} L_{\ell}^{\alpha}, \tag{3.29}$$

where L_{ℓ}^{α} is the total torque on the particle such that

$$L_{\ell}^{\alpha} = \int_{\partial D} \varepsilon_{\ell mn}\left(y_m - x_m^{\alpha}\right) f_n^{\alpha} dS. \tag{3.30}$$

Spherical Particle We take a look at a specific case — a suspension of spherical particles. For spherical particles, the fourth-order tensor $J_{ij,k\ell}$ must be isotropic for spheres, so $J_{ij,k\ell}$ is equivalent to $\nabla^2 J_{ij}$. But, the simplification cannot be made for aspherical particles. After some algebra, we can rewrite Eq. (3.25) such like

$$\begin{aligned} u_i(\mathbf{x}) - u_i^{\infty}(\mathbf{x}) = \frac{1}{8\pi\eta}\sum_{\alpha=1}^{N}\Bigg(1 + \frac{1}{6}a^2\nabla^2\Bigg) J_{ij} F_j^{\alpha} \\ + R_{ij} L_j^{\alpha} + \Bigg(1 + \frac{1}{10}a^2\nabla^2\Bigg) K_{ijk} S_{jk}^{\alpha}, \end{aligned} \tag{3.31}$$

where R_{ij} is called *rotlet* such that

$$R_{ij} = \frac{1}{4}\varepsilon_{\ell kj}\left(\frac{\partial J_{i\ell}}{\partial x_k} - \frac{\partial J_{ik}}{\partial x_\ell}\right) \tag{3.32}$$

and

$$K_{ijk} = \frac{1}{2}\left(J_{ij,k} + J_{ik,j}\right). \tag{3.33}$$

Now, we assume a single sphere is translating under an external force $\mathbf{F}$. The torque, stresslet, and higher moments can be neglected. So,

$$u_i\left(\mathbf{x}\right) - u_i^{\infty}\left(\mathbf{x}\right) = \frac{1}{8\pi\eta}\left(1 + \frac{1}{6}a^2\nabla^2\right)J_{ij}F_j. \tag{3.34}$$

With

$$\nabla^2 J_{ij} = \frac{2\delta_{ij}}{r^3} - \frac{6x_i x_j}{r^5} \tag{3.35}$$

substituted, the disturbance velocity field caused by a single sphere subject to a force $\mathbf{F}$ is

$$u_i\left(\mathbf{x}\right) - u_i^{\infty}\left(\mathbf{x}\right) = \frac{1}{8\pi\eta}\left[\left(\frac{1}{r} + \frac{a^2}{3r^3}\right)F_i + \left(\frac{1}{r^3} - \frac{a^2}{r^5}\right)x_k F_k x_i\right], \tag{3.36}$$

which is essentially identical to Eq. (3.5a) if we make a comparison and note that

$$F_i = -6\pi\eta a u_i^{\infty}, \tag{3.37}$$

which is Stokes law!

3.2.5 The Far-Field Mobility Tensor — Faxen's Formulae

We have seen that by using the multipole expansion we can find the velocity field disturbed that is by the particles. For a spherical suspension, the moment is usually truncated at the stresslet level. Higher moments are included in other studies [66], but they are not in the scope of this study. Starting from here, we will focus on the discussion of spherical particle, because this study is built upon the knowledge of spherical suspensions.

We have used the multipole expansion to derive the velocity field of a single sphere moving under an external force. Now, we solve another problem — a force $\mathbf{F}^\alpha$ (the drag is then $-\mathbf{F}^\alpha$) is applied to a sphere that is immersed in a fluid upon which a point force $\mathbf{f}$ is acted at position $\boldsymbol{\xi}$. We want to calculate the velocity $\mathbf{U}^\alpha$ of the particle. By using the Lorentz reciprocal theorem, we can calculate $\mathbf{U}^\alpha$ while avoiding deriving the flow field. After we derive $\mathbf{U}^\alpha$, we are capable of obtaining the *far-field mobility tensor* — one of the most important ingredients in this chapter.

We look back at Eq. (3.18) and make the following assumptions

- Make $\mathbf{u}'$ the velocity field of a sphere (identical to sphere α) moving with a velocity $\mathbf{U}$ in a quiescent fluid so that the corresponding stress field $\boldsymbol{\sigma}'$ obeys that $\boldsymbol{\nabla} \cdot \boldsymbol{\sigma}' = 0$. Note that the drag force on this sphere is $-6\pi\eta\mathbf{U}$.

- Make $\mathbf{u}$ the velocity field subject to a point force $\mathbf{f}$ at position $\boldsymbol{\xi}$ so that the corresponding stress field $\boldsymbol{\sigma}$ obeys that $\boldsymbol{\nabla} \cdot \boldsymbol{\sigma} = \mathbf{f}\delta(\mathbf{x} - \boldsymbol{\xi})$.

Then, we substitute these assumptions into Eq. (3.18), and we get

$$-\mathbf{U} \cdot \mathbf{F}^{\alpha} - \mathbf{u}'(\boldsymbol{\xi}) \cdot \mathbf{f} = -\mathbf{U}^{\alpha} \cdot (6\pi\eta a \mathbf{U}). \tag{3.38}$$

We already know that

$$\begin{aligned} \mathbf{u}'(\boldsymbol{\xi}) &= \frac{1}{8\pi\eta}\left(1 + \frac{1}{6}a^2\nabla^2\right)\mathbf{J}(\mathbf{x}^{\alpha} - \boldsymbol{\xi}) \cdot \mathbf{F} \\ &= \frac{3a}{4}\left(1 + \frac{1}{6}a^2\nabla^2\right)\mathbf{J}(\mathbf{x}^{\alpha} - \boldsymbol{\xi}) \cdot \mathbf{U}. \end{aligned} \tag{3.39}$$

Substituting Eq. (3.37)into Eq. (3.38) and factoring $\mathbf{U}$ out, we have

$$\mathbf{F}^{\alpha} + \frac{3a}{4}\left(1 + \frac{1}{6}a^2\nabla^2\right)\mathbf{J}(\mathbf{x}^{\alpha} - \boldsymbol{\xi}) \cdot \mathbf{f} = 6\pi\eta a \mathbf{U}^{\alpha}. \tag{3.40}$$

Note that the velocity field, $\mathbf{v}$, subject to a point force is

$$\mathbf{v}(\mathbf{x}^{\alpha}) = \frac{1}{8\pi\eta}\mathbf{J}(\mathbf{x}^{\alpha} - \boldsymbol{\xi}) \cdot \mathbf{f}. \tag{3.41}$$

Thus, the velocity of particle α is

$$\mathbf{U}^{\alpha} = \frac{\mathbf{F}^{\alpha}}{6\pi\eta a} + \left(1 + \frac{1}{6}a^2\nabla^2\right)\mathbf{v}(\mathbf{x}^{\alpha}). \tag{3.42}$$

More generally, if an imposed flow field $\mathbf{u}^\infty$ exists, and $\mathbf{v}$ is the flow field that is caused by particles other than particle α given by Eq. (3.31), then we have

$$\mathbf{U}^\alpha - \mathbf{u}^\infty\left(\mathbf{x}^\alpha\right) = \frac{\mathbf{F}^\alpha}{6\pi\eta a} + \left(1 + \frac{1}{6}a^2\nabla^2\right)\mathbf{v}\left(\mathbf{x}^\alpha\right). \tag{3.43}$$

The same technique can be applied to derive the angular velocity and rate of strain. Now, we have the *Faxen's formulae*

$$\mathbf{U}^\alpha - \mathbf{u}\left(\mathbf{x}^\alpha\right) = \frac{\mathbf{F}^\alpha}{6\pi\eta a} + \left(1 + \frac{1}{6}a^2\nabla^2\right)\mathbf{v}\left(\mathbf{x}^\alpha\right) \tag{3.44a}$$

$$\boldsymbol{\Omega}^\alpha - \boldsymbol{\Omega}^\infty = \frac{\mathbf{L}^\alpha}{8\pi\eta a^3} + \frac{1}{2}\boldsymbol{\nabla}\times\mathbf{v}\left(\mathbf{x}^\alpha\right), \text{ and} \tag{3.44b}$$

$$-\mathbf{E}^\infty = \frac{\mathbf{S}^\alpha}{\frac{20}{3}\pi\eta a^3} + \left(1 + \frac{1}{10}a^2\nabla^2\right)\mathbf{e}\left(\mathbf{x}^\alpha\right), \tag{3.44c}$$

where $\mathbf{e} = \frac{1}{2}\left(\boldsymbol{\nabla}\mathbf{v} + \boldsymbol{\nabla}\mathbf{v}^{\mathrm{T}}\right)$.

If we write Eq (3.44) explicitly, we are able to construct a mobility tensor $\mathcal{M}$ that couples the translational and rotational velocity and rate of strain to the force, torque, and stresslet of all particles such that

$$\begin{pmatrix} \mathbf{U} - \mathbf{U}^\infty \\ -\mathbf{E}^\infty \end{pmatrix} = \mathcal{M}\cdot\begin{pmatrix} \mathbf{F} \\ \mathbf{S} \end{pmatrix}, \tag{3.45}$$

where

$$\mathcal{M} = \begin{pmatrix} \mathbf{M}_{\mathrm{UF}} & \mathbf{M}_{\mathrm{US}} \\ \mathbf{M}_{\mathrm{EF}} & \mathbf{M}_{\mathrm{ES}} \end{pmatrix}. \tag{3.46}$$

Here, $\mathbf{U}$ contains the translational and rotational velocity (a $6N$ vector), and $\mathbf{F}$ (a $6N$ vector), contains the force and torque. Because of the linearity of Stokes flow, we can reverse the roles of force/stresslet and velocity/rate of strain such that

$$\begin{pmatrix} \mathbf{F} \\ \mathbf{S} \end{pmatrix} = \mathcal{R} \cdot \begin{pmatrix} \mathbf{U} - \mathbf{U}^{\infty} \\ \mathbf{E}^{\infty} \end{pmatrix}, \tag{3.47}$$

where $\mathcal{R}$ is the so-called *resistance tensor*, and we can see that $\mathcal{M}^{-1} = \mathcal{R}$. We term Eq. (3.45) as the *mobility problem* and Eq. (3.47) as the *resistance problem*. In this subsection, we focus on the mobility problem and discuss the resistance problem later.

Mobility Problem. Since $\mathcal{M}$ is truncated at the level of stresslet and it includes only far-field interactions, $\mathcal{M}$ can be approximated as $\mathcal{M}^{\infty}$, the *far-field mobility tensor*. We follow the notations of Kim and Mifflin's paper [52] such that

$$\mathcal{M}^{\infty} = \begin{pmatrix} \mathbf{a} & \widetilde{\mathbf{b}} & \widetilde{\mathbf{g}} \\ \mathbf{b} & \mathbf{c} & \widetilde{\mathbf{h}} \\ \mathbf{g} & \mathbf{h} & \mathbf{m} \end{pmatrix}.$$

We will solve the tensor $\mathbf{a}$ of a two-particle system. The tensor $\mathbf{a}$ is also known as the *Rotne-Prager tensor*. We solve this problem as an example, which will later be an example of discussion of *Ewald summation* in Appendix B. Also, this example will be related to a discussion of the equivalence of inverting the mobility tensor

and the resistance tensor in later time.

We write the mobility problem of two spheres α and β such that

$$\begin{pmatrix} \mathbf{U}^{\alpha} \\ \mathbf{U}^{\beta} \end{pmatrix} = \begin{pmatrix} \mathbf{a}^{\alpha\alpha} & \mathbf{a}^{\alpha\beta} \\ \mathbf{a}^{\beta\alpha} & \mathbf{a}^{\beta\beta} \end{pmatrix} \cdot \begin{pmatrix} \mathbf{F}^{\alpha} \\ \mathbf{F}^{\beta} \end{pmatrix} \tag{3.48}$$

By applying Faxen's formula Eq. (3.44a) and the multipole expansion Eq. (3.31), we have

$$U_i^{\alpha} = \frac{F_i^{\alpha}}{6\pi\eta a} + \frac{1}{8\pi\eta}\left(1 + \frac{1}{6}a^2\nabla^2\right)\left(1 + \frac{1}{6}a^2\nabla^2\right) J_{ij} F_j^{\beta}. \tag{3.49}$$

If we non-dimensionalize the velocity by $6\pi\eta a$ and any length by sphere's radius a, we have the form

$$U_i^{\alpha} = F_i^{\alpha} + \frac{3}{4}\left(1 + \frac{1}{6}\nabla^2\right)\left(1 + \frac{1}{6}\nabla^2\right) J_{ij} F_j^{\beta}. \tag{3.50}$$

Obviously, we can make the following statement from a comparison between the above equation and Eq. (3.48) that

$$a_{ij}^{\alpha\alpha} = \delta_{ij}, \text{ and} \tag{3.51a}$$

$$a_{ij}^{\alpha\beta} = \frac{3}{4}\left(1 + \frac{1}{6}\nabla^2\right)\left(1 + \frac{1}{6}\nabla^2\right) J_{ij} \tag{3.51b}$$

By the symmetry of the equation, we can deduce that $a_{ij}^{\beta\alpha} = a_{ij}^{\alpha\beta}$ and $a_{ij}^{\beta\beta} = a_{ij}^{\alpha\alpha}$.

We can obtain $a_{ij}^{\alpha\beta}$ through some algebra such that (note that $\nabla^2\nabla^2 J_{ij} = 0$)

$$a_{ij}^{\alpha\beta} = \left(\frac{3}{2r} - \frac{1}{r^3}\right) e_i e_j + \left(\frac{3}{4r} + \frac{1}{2r^3}\right)(\delta_{ij} - e_i e_j), \tag{3.52}$$

where $e_i = \frac{x_i}{r}$ is the unit vector connecting the two particles. If we adopt the notation of Kim and Karrila [30] such that

$$a_{ij}^{\alpha\beta} = x_{\alpha\beta}^a e_i e_j + y_{\alpha\beta}^a (\delta_{ij} - e_i e_j) \tag{3.53}$$

and make a comparison, then we obtain that

$$x_{\alpha\beta}^a = \frac{3}{2r} - \frac{1}{r^3}, \text{ and} \tag{3.54a}$$

$$y_{\alpha\beta}^a = \frac{3}{4r} + \frac{1}{2r^3}. \tag{3.54b}$$

Here, $x_{\alpha\beta}^a$ represents the interaction along the line of center, and $y_{\alpha\beta}^a$ represents the interaction perpendicular to the line of center.

3.2.6 The Method of Reflection

We now look at a new technique that deals with the hydrodynamic interactions between particles, which may seem to be a bifurcation from our journey, but later, we will be shown that this technique is crucial to this study.

We suppose that two particles, α and β, are separated widely (much larger than

their size). Both particles move with a velocity $\mathbf{U}^\alpha$ and $\mathbf{U}^\beta$ respectively in an unbounded fluid. Let the flow-field disturbed by these two particles to be $\mathbf{u}^\alpha$ and $\mathbf{u}^\beta$. At the surface of these two particles, we have the following boundary conditions

$$\mathbf{u}_1^\alpha = \mathbf{U}^\alpha \text{ on } \partial D^\alpha \text{ and} \tag{3.55a}$$

$$\mathbf{u}_1^\beta = \mathbf{U}^\beta \text{ on } \partial D^\beta. \tag{3.55b}$$

We know that the boundary conditions are not accurate because at the vicinity of particle α, the flow field is also disturbed by particle β, and vice versa. So, we need to make corrections at the boundaries, and on each particle surface, we have

$$\mathbf{u}_2^\alpha = -\mathbf{u}_1^\beta \text{ on } \partial D^\alpha \text{ and} \tag{3.56a}$$

$$\mathbf{u}_2^\beta = -\mathbf{u}_1^\alpha \text{ on } \partial D^\beta. \tag{3.56b}$$

We can make the corrections infinitely. And the resulting flow field becomes

$$\mathbf{u}^\alpha = \mathbf{u}_1^\alpha + \mathbf{u}_2^\alpha + \mathbf{u}_3^\alpha + \dots \text{ and} \tag{3.57a}$$

$$\mathbf{u}^\beta = \mathbf{u}_1^\beta + \mathbf{u}_2^\beta + \mathbf{u}_3^\beta + \dots. \tag{3.57b}$$

Now, we look at an example. Suppose that the two particles are spherical. We fix α in the fluid and move β at a constant velocity $\mathbf{U}^\beta$ toward α. We wish to

calculate the force $\mathbf{F}^{\alpha}$ on α that keeps it fixed. The disturbance velocity that is caused by sphere β is

$$\mathbf{u} = \frac{3}{4}\left(1 + \frac{1}{6}\nabla^2\right)\mathbf{J}\left(\mathbf{x} - \mathbf{x}^{\beta}\right)\cdot\mathbf{U}^{\beta}. \tag{3.58}$$

The force on sphere α given by the Faxen's formula is then

$$\mathbf{F}^{\alpha} = -\frac{3}{4}\left(1 + \frac{1}{6}\nabla^2\right)\mathbf{J}\left(\mathbf{x}^{\alpha} - \mathbf{x}^{\beta}\right)\cdot\mathbf{U}^{\beta}. \tag{3.59}$$

This force is reflected back to the fluid to make the disturbance velocity

$$\begin{aligned}\mathbf{u} &= \frac{3}{4}\left(1 + \frac{1}{6}\nabla^2\right)\mathbf{J}\left(\mathbf{x} - \mathbf{x}^{\beta}\right)\cdot\mathbf{F}^{\alpha} \\ &= -\frac{3}{4}\left(1 + \frac{1}{6}\nabla^2\right)\mathbf{J}\left(\mathbf{x} - \mathbf{x}^{\beta}\right)\cdot\frac{3}{4}\left(1 + \frac{1}{6}\nabla^2\right)\mathbf{J}\left(\mathbf{x}^{\alpha} - \mathbf{x}^{\beta}\right)\cdot\mathbf{U}^{\beta}.\end{aligned} \tag{3.60}$$

Then, this disturbance velocity is reflected on sphere α again. These reflections continue infinitely, and the force that fixes α becomes

$$\begin{aligned}\mathbf{F}^{\alpha} = &-\frac{3}{4}\left(1 + \frac{1}{6}\nabla^2\right)^2\mathbf{J}\left(\mathbf{x}^{\alpha} - \mathbf{x}^{\beta}\right)\cdot\mathbf{U}^{\beta} \\ &-\left(\frac{3}{4}\right)^3\left(1 + \frac{1}{6}\nabla^2\right)^2\mathbf{J}\left(\mathbf{x}^{\alpha} - \mathbf{x}^{\beta}\right)\cdot\left(1 + \frac{1}{6}\nabla^2\right)^2\mathbf{J}\left(\mathbf{x}^{\alpha} - \mathbf{x}^{\beta}\right)\cdot\mathbf{U}^{\beta} \\ &-\ldots.\end{aligned} \tag{3.61}$$

Obviously, in this case we are solving a resistance problem such that

$$\begin{pmatrix} \mathbf{F}^{\alpha} \\ \mathbf{F}^{\beta} \end{pmatrix} = \begin{pmatrix} \mathbf{A}^{\alpha\alpha} & \mathbf{A}^{\alpha\beta} \\ \mathbf{A}^{\beta\alpha} & \mathbf{A}^{\beta\beta} \end{pmatrix} \cdot \begin{pmatrix} \mathbf{U}^{\alpha} \\ \mathbf{U}^{\beta} \end{pmatrix}, \tag{3.62}$$

and we are solving the $\mathbf{A}^{\alpha\beta}$ is this particular case. We write $\mathbf{A}^{\alpha\beta}$ in a similar form as $\mathbf{a}^{\alpha\beta}$ such that

$$A_{ij}^{\alpha\beta} = X_{\alpha\beta}^{A} e_i e_j + Y_{\alpha\beta}^{A} \left(\delta_{ij} - e_i e_j\right). \tag{3.63}$$

As sphere β moves along the line of center, we can solve for $X_{\alpha\beta}^{A}$ only. By completing the summation such that

$$\begin{aligned} X_{\alpha\beta}^{A} &= \sum_{n=1}^{\infty} \left(-\frac{3}{4}\right)^{2n-1} \left[\left(1 + \frac{1}{6}\nabla^2\right)^2 J_{ij}\right]^{2(n-1)} \\ &= \frac{\left(\frac{3}{2r} - \frac{1}{r^3}\right)}{\left(\frac{3}{2r} - \frac{1}{r^3}\right)^2 - 1}. \end{aligned} \tag{3.64}$$

The same method can be used to derive $X_{\alpha\alpha}^{A}$, and $X_{\alpha\alpha}^{A}$ is

$$X_{\alpha\alpha}^{A} = \frac{-1}{\left(\frac{3}{2r} - \frac{1}{r^3}\right)^2 - 1}. \tag{3.65}$$

Interestingly, if we invert the matrix

$$\begin{pmatrix} x_{\alpha\alpha}^{a} & x_{\alpha\beta}^{a} \\ x_{\beta\alpha}^{a} & x_{\beta\beta}^{a} \end{pmatrix} = \begin{pmatrix} 1 & \frac{3}{2r} - \frac{1}{r^3} \\ \frac{3}{2r} - \frac{1}{r^3} & 1 \end{pmatrix}, \tag{3.66}$$

we will obtain that

$$\begin{pmatrix} x^a_{\alpha\alpha} & x^a_{\alpha\beta} \\ x^a_{\beta\alpha} & x^a_{\beta\beta} \end{pmatrix}^{-1} = \begin{pmatrix} \frac{-1}{\left(\frac{3}{2r}-\frac{1}{r^3}\right)^2-1} & \frac{\left(\frac{3}{2r}-\frac{1}{r^3}\right)}{\left(\frac{3}{2r}-\frac{1}{r^3}\right)^2-1} \\ \frac{\left(\frac{3}{2r}-\frac{1}{r^3}\right)}{\left(\frac{3}{2r}-\frac{1}{r^3}\right)^2-1} & \frac{-1}{\left(\frac{3}{2r}-\frac{1}{r^3}\right)^2-1} \end{pmatrix} = \begin{pmatrix} X^A_{\alpha\alpha} & X^A_{\alpha\beta} \\ X^A_{\beta\alpha} & X^A_{\beta\beta} \end{pmatrix}, \tag{3.67}$$

which is not so surprising since it is just a result of the linearity of Stokes flow. Thus, the inverse of the mobility tensor is proven to be equivalent to the resistance tensor. Moreover, the resistance problem that we have solved includes an infinite number of reflections, which are the reflections of all particles. So, the inverse of the mobility tensor represents the *many-body* interactions among particles.

3.2.7 Stokesian Dynamics

We have used the method of reflections to solve the resistance problem where the particles are widely separated so that the point force approximation can be made, and we have also shown that this resistance problem is equivalent to the inverse of a far-field mobility problem. However, the *lubrication* force still lacks. The lubrication force arises when two boundaries come very close to each other, and as the boundaries squeeze the fluid, a thin layer of fluid generates a very large stress that keeps the boundaries from collapsing. To include the lubrication interaction, all the moments need to be included in the multipole expansion equation, which is not possible. In this study the multipole expansion is truncated at the level of stresslets, so we need to make a correction. Our goal is to construct a resistance tensor that includes both the far-field many-body interactions and the near-field lu-

brication interactions. The lubrication interaction is a two-body interaction which depends on the relative motion between the particles. As proposed by Durlofsky et al. [53], this two-body interaction can be added to the far-field many-body interaction, and since the far-field two-body interaction is already included in the inverse of the far-field mobility tensor, it has to be subtracted. Therefore, we have the resistance tensor $\mathcal{R}$ such that

$$\mathcal{R} = [\mathcal{M}^{\infty}]^{-1} + \mathcal{R}_{\mathrm{2B}} - \mathcal{R}^{\infty}_{\mathrm{2B}}, \tag{3.68}$$

where $\mathcal{R}_{\mathrm{2B}}$ is the two-body resistance tensor, which is an exact solution of two spheres (see Jeffrey and Onishi's work [51] or Kim and Mifflin's [52] work), and $\mathcal{R}^{\infty}_{\mathrm{2B}}$ is the far-field two-body interaction that is already included in $[\mathcal{M}^{\infty}]^{-1}$. So, $\mathcal{R}_{\mathrm{2B}} - \mathcal{R}^{\infty}_{\mathrm{2B}}$ is the lubrication interaction. This idea is the essential part of *Stokesian Dynamics*, a technique invented Brady [67]. Now, we rewrite the resistance problem in a form that is analogous to Eq. (3.46) such that

$$\begin{pmatrix} \mathbf{F} \\ \mathbf{S} \end{pmatrix} = \begin{pmatrix} \mathbf{R}_{\mathrm{FU}} & \mathbf{R}_{\mathrm{FE}} \\ \mathbf{R}_{\mathrm{SU}} & \mathbf{R}_{\mathrm{SE}} \end{pmatrix} \cdot \begin{pmatrix} \mathbf{U} - \mathbf{U}^{\infty} \\ -\mathbf{E}^{\infty} \end{pmatrix}. \tag{3.69}$$

Equation (3.69) is the essential part of solving the velocities and stresslets of particles such that

$$\mathbf{U} = \mathbf{U}^{\infty} + \mathbf{R}^{-1}_{\mathrm{FU}} \cdot (\mathbf{F} + \mathbf{R}_{\mathrm{FE}} : \mathbf{E}^{\infty}), \text{ and} \tag{3.70a}$$

$$\mathbf{S} = \mathbf{R}_{\mathrm{SU}} \cdot \mathbf{R}^{-1}_{\mathrm{FU}} \cdot \mathbf{F} + \left(\mathbf{R}_{\mathrm{SU}} \cdot \mathbf{R}^{-1}_{\mathrm{FU}} \cdot \mathbf{R}_{\mathrm{FE}} - \mathbf{R}_{SE}\right) : \mathbf{E}^{\infty}. \tag{3.70b}$$

Note that the $\mathbf{E}^\infty$ (and $\mathbf{S}$) is a symmetric and traceless second-order tensor, so there are 5 independent components, so is the stresslet S. We usually write $\mathbf{E}^\infty$ and $\mathbf{S}$ in vectorized forms as $E^\infty_{xx} - E^\infty_{zz}$, $2E^\infty_{xy}$, $2E^\infty_{xz}$, $2E^\infty_{yz}$, and $E^\infty_{yy} - E^\infty_{zz}$, and S_{xx}, S_{xy}, S_{xz}, S_{yz}, and S_{yy}. Now, we are set to model the hydrodynamic interactions among and between particles, and the flowchart of the simulation is shown in Appendix C. Equations (3.70a) and (3.70b) enable us to complete the simulation of dynamics of particles and the computation of the rheological properties of the fluid.

Once we have obtained the stresslets, we are able to compute the viscosity and first normal stress difference that is the indicator of elasticity of a fluid. We write the average stress of the fluid as

$$\langle \sigma_{ij} \rangle = \text{I.T.} + 2\eta E^\infty_{ij} + \frac{1}{V} \sum_{\alpha=1}^{N} S^\alpha_{ij}, \tag{3.71}$$

where I.T. stands for the isotropic part. Therefore, we can write down the effective shear viscosity, assuming that the shear rate is $\dot{\gamma}$ in the direction of xy, such that

$$\eta^{\text{eff}} = \eta + \frac{1}{V\dot{\gamma}} \sum_{\alpha=1}^{N} S^\alpha_{xy}. \tag{3.72}$$

Computing the rheological properties of the fluid requires a simulation of an infinite system, an infinite number of particles ($N \to \infty$) in an infinitely large space ($V \to \infty$), while keeping the density constant. *Periodic boundary conditions* are

often imposed to such system under the assumption that the system is homogeneous. However, due to the slow convergence rate of the hydrodynamic interaction $\sim r^{-1}$, interactions are impossible to terminate. This dilemma has been resolved by using *Ewald summation* [68,69]. Ewald summation is a commonly used technique that models the long-range interaction between particles, such as electrostatic interactions and dipole-dipole interactions, in a periodic system. Briefly speaking, Ewald summation decomposes the interaction into two parts, one converges fast in the real space and the other one converges fast in the Fourier space. The details of application of Ewald summation in hydrodynamic interactions can be found in the Appendix B.

3.3 Elements of Magnetic Interactions

We have discussed the hydrodynamic interactions so far. Because the magnetic field is the only external field applied in this study, we have to address the magnetic interactions here.

Under an external magnetic field, $\mathbf{B}$, a magnetic particle with volume V that is magnetized by the field will have an induced dipole such that

$$\mu_i^\alpha = \frac{V\chi^E}{\mu_0} B_i. \tag{3.73}$$

The induced dipole of particle α generates a potential vector in the space. At an arbitrary position $\mathbf{x}$, assuming that particle α is located at the origin for conve-

nience, in an arbitrary position other than the origin, the potential vector $\mathbf{A}$ is

$$A_k = \frac{\mu_0}{4\pi r^3}\varepsilon_{kmn}\mu_m^\alpha x_n. \tag{3.74}$$

The potential vector generates a magnetic flux density, $\widetilde{B}_i^\alpha$, which can also be termed as the magnetic field that is caused by the induced dipole of particle α, such that

$$\begin{aligned}\widetilde{B}_i^\alpha &= \varepsilon_{ijk}\frac{\partial}{\partial x_j}A_k \\ &= \frac{\mu_0}{4\pi}\left(\frac{3x_j\mu_j^\alpha x_i}{r^5} - \frac{\mu_i^\alpha}{r^3}\right).\end{aligned} \tag{3.75}$$

Suppose another magnetic particle β is located at position $\mathbf{x}$ with induced dipole moment μ_i^β, then the potential between α and β, Φ, is

$$\begin{aligned}\Phi &= -\mu_i^\beta \widetilde{B}_i^\alpha \\ &= -\frac{\mu_0}{4\pi}\left(\frac{3x_j\mu_j^\alpha x_i\mu_i^\beta}{r^5} - \frac{\mu_i^\alpha\mu_i^\beta}{r^3}\right),\end{aligned} \tag{3.76}$$

and the magnetic force, the gradient of the potential, is

$$\begin{aligned}F_i^M &= -\frac{\partial\Phi}{\partial x_i} \\ &= \frac{\mu_0}{4\pi}\left(\frac{3\mu_i^\alpha x_k\mu_k^\beta}{r^3} + \frac{3\mu_i^\beta x_k\mu_k^\alpha}{r^3} - \frac{15x_j\mu_j^\alpha x_k\mu_k^\beta x_i}{r^7} + \frac{\mu_j^\alpha\mu_j^\beta x_i}{r^5}\right).\end{aligned} \tag{3.77}$$

Typically, μ_i^α and μ_i^β are identical for spherical particles, but different for oblate

spheroids, since the induced dipole moment depends on the orientation of the particle.

For multiple particles (more than 2) the magnetic force on particle α is

$$F_i^{M,(\alpha)} = \frac{\mu_0}{4\pi} \sum_{\beta=1}^{N}{}' \left(\frac{3\mu_i^\alpha \xi_k \mu_k^\beta}{r^3} + \frac{3\mu_i^\beta \xi_k \mu_k^\alpha}{r^3} - \frac{15\xi_j \mu_j^\alpha \xi_k \mu_k^\beta \xi_i}{r^7} + \frac{\mu_j^\alpha \mu_j^\beta \xi_i}{r^5} \right), \qquad (3.78)$$

where the prime on the summation means that $\beta \neq \alpha$, $\xi_i = x_i^\alpha - x_i^\beta$, and $r^2 = \xi_i \xi_i$.

The magnetic force that is introduced above is based on a model called the *fixed dipole model*, which means the induced dipole of each particle is only a result of the external field. But, in fact, the induced dipole of one particle can further induce other particles, and this interaction can go on and on infinitely, an idea analogous with the method of reflections in hydrodynamics. But, due to limited knowledge of the author in electromagnetics, this simplest model will be used in this study. An accurate description of the magnetic interactions can be found in [70]. In Bonnecaze and Brady's study [36], they used a method that is analogous with the Stokesian dynamics to model the electrostatic interactions between particles. They constructed a grand capacitance tensor, which includes both the many-body far-field interactions and exact two-body near-field interactions.

3.4 An Approximated Method to Model Aspherical Particles

In the previous sections, we focus on the discussions of spherical particles. But the goal of this study is to model the oblate spheroids as described in Chapter 2. We have noticed that, during the derivation of the mobility or resistance problem, the mobility or resistance tensor depends on the configuration of the suspensions only. If the geometry of the particle becomes complicated, such as ellipsoids or other non-analytic surfaces, the description of the mobility or resistance tensor becomes intractable.

However, the hydrodynamic interactions among the spherical particles are well known. So, if we can configure sets of spheres to the shape that we want to model, we can approximate the hydrodynamic interactions among spherical particles to be the hydrodynamic interactions among aspherical particles. For example, we can approximate a rod as a line of spheres and a disk as a plane of spheres as shown in Fig. 3.1(a) and 3.1(b). We need to force the constituent spheres to stay in rigid-bodies. This constraint can be made by imposing a rigid-body tensor [54, 55, 71] or a constraint force [63, 72]. We will adopt the former method, and the rigid-body

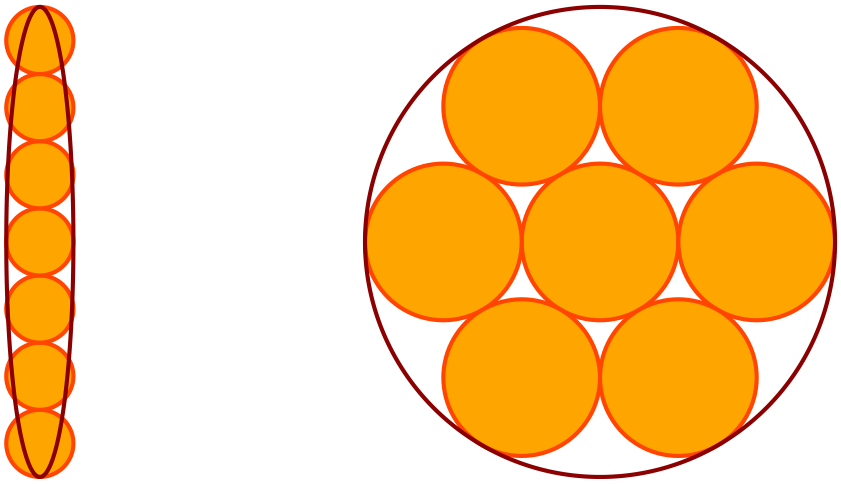

(a) Spherical representation of rod (b) Spherical representation of disk

Figure 3.1: Spherical representations of aspherical shapes.

tensor $\boldsymbol{\Sigma}$ is [71]

$$\boldsymbol{\Sigma}^{A\alpha} = \begin{pmatrix} 1 & 0 & 0 & 0 & 0 & 0 \\ 0 & 1 & 0 & 0 & 0 & 0 \\ 0 & 0 & 1 & 0 & 0 & 0 \\ 0 & r_3^{\alpha A} & -r_2^{\alpha A} & 1 & 0 & 0 \\ -r_3^{\alpha A} & 0 & r_1^{\alpha A} & 0 & 1 & 0 \\ r_2^{\alpha A} & -r_1^{\alpha A} & 0 & 0 & 0 & 1 \end{pmatrix}, \tag{3.79}$$

where A stands for the center of rigid-body A, α stands for sphere α, and $\mathbf{r}^{\alpha A} = \mathbf{x}^{\alpha} - \mathbf{x}^{A}$. The total force on a rigid body, given the forces of the constituent spheres,

is

$$\mathbf{F}^A = \boldsymbol{\mathcal{Z}}^{A\alpha} \cdot \mathbf{F}^\alpha. \tag{3.80}$$

So, rewriting Eq. (3.70a) in the rigid-body manner, we have the velocity, $\mathbf{U}^\infty$, of rigid body such that

$$\mathbf{U}^A - \mathbf{U}^\infty = \left[\boldsymbol{\mathcal{Z}} \cdot \mathbf{R}_{\mathrm{FU}} \cdot \boldsymbol{\mathcal{Z}}^T\right]^{-1} \cdot \boldsymbol{\mathcal{Z}} \cdot \mathbf{F}^\alpha, \tag{3.81}$$

where $\left[\boldsymbol{\mathcal{Z}} \cdot \mathbf{R}_{\mathrm{FU}} \cdot \boldsymbol{\mathcal{Z}}^T\right]^{-1}$ is the "rigid-body resistance tensor" that sums the hydrodynamic interactions among spheres while keeping the spheres of each assembly in a rigid-body fashion. In other words, it includes the hydrodynamic interactions among rigid bodies that are approximated by the hydrodynamic interactions among spheres, and $\mathbf{F}^\alpha$ is the prescribed external force on each sphere. In this study, magnetic forces are prescribed to disks, and the forces can be distributed on each sphere by deducing an effective susceptibility of each sphere where the summation of the susceptibility of the spheres should be equivalent to the effective susceptibility of the original disk. This part of work is still under investigation. We are going to use an alternative method.

Suppose that a single disk is moving in an unbounded fluid under an external magnetic force $\mathbf{F}^{\mathrm{MOP}}$ and the velocity of the disk is simply a product of the magnetic force and a single-disk mobility tensor such that $\mathcal{M}^{\mathrm{MOP},\infty} \cdot \mathbf{F}^{\mathrm{MOP}}$. We then distribute this velocity to each sphere by multiplying it by the transpose of $\boldsymbol{\mathcal{Z}}$. By multiplying a resistance tensor $\mathcal{R}^\infty$ to the distributed velocity, we obtain the

drag on each sphere. Because the magnetic force is balanced by the drag on the disk, the drag on each sphere should be equivalent to the magnetic force that is distributed on each sphere. In the equation form, we rewrite Eq. (3.81) such that

$$\mathbf{U}^A - \mathbf{U}^\infty = \left[\boldsymbol{\Sigma} \cdot \mathbf{R}_{\mathrm{FU}} \cdot \boldsymbol{\Sigma}^T\right]^{-1} \cdot \boldsymbol{\Sigma} \cdot \mathcal{R}^\infty \cdot \boldsymbol{\Sigma}^T \cdot \mathcal{M}^{\mathrm{MOP},\infty} \cdot \mathbf{F}^{\mathrm{MOP}}. \tag{3.82}$$

Here, $\mathcal{R}^\infty$ is an approximation of $\mathbf{R}_{\mathrm{FU}}$ without lubrication interactions since lubrication interactions arise from the relative motion between particles, and no relative motion exists between spheres that are in the same rigid body.

Now, we have a method to model the dynamics of aspherical particles that have hydrodynamic interactions included, at least approximately and the precision depends on the resolution of the decomposition. The results of the simulations will be shown later in the Results and Discussion section (Section 3.6). First, I am going to derive a parameter that governs the motions of oblate spheroids.

3.5 Derivation of Timescales

We are not able to model the hydrodynamic interactions between true oblate spheroids, and thus, we are unable to simulate realistic dynamics of true oblate spheroids. But, we can obtain scalings of timescales that dictate the motions of oblate spheroids.

We have a look back at the force and torque balance equations, assuming no

Brownian force or inertia,

$$\mathbf{F}^M + \mathbf{F}^H = 0, \text{ and} \tag{3.83a}$$

$$\mathbf{T}^M + \mathbf{T}^H = 0. \tag{3.83b}$$

In Chapter 2, we have already solved the torque balance part, and we can write down the angular velocity such that

$$\Omega_i^\alpha = \frac{3}{32\eta a^3}\varepsilon_{ijk}\mu_j B_k, \tag{3.84}$$

and we also have derived a characteristic timescale, t_R, that is associated with the rotational motion such that

$$t_R = \frac{32\eta a^3 \mu_0}{3V\chi_\perp^E B^2\left(1-\alpha\right)}, \tag{3.85}$$

where $\alpha = \chi_\parallel^E/\chi_\perp^E$ which is smaller than 1. Similarly, we can derive a characteristic timescale, t_T, that is associated with the translational motion. First, we write down the hydrodynamic force of an oblate spheroid from a first-order approximation:

$$F_i^H = A_{ij}U_j, \tag{3.86}$$

where [30]

$$A_{ij} = 6\pi\eta a\left(X^A p_i p_j + Y^A\left(\delta_{ij} - p_i p_j\right)\right), \tag{3.87}$$

where X^A and Y^A are resistance functions. When the aspect ratio is high, $X^A \approx$

$\frac{8}{3\pi}$, and $Y^A \approx \frac{16}{9\pi}$. By combining the magnetic force Eq. (3.77) and assuming only two particles exist, we have the following equation for the velocity of oblate spheroid α

$$\left(p_i^\alpha p_j^\alpha + 2\delta_{ij}\right) U_j = \frac{3\mu_0}{64\pi\eta a}\left(\frac{3\mu_i^\alpha x_k \mu_k^\beta}{r^3} + \frac{3\mu_i^\beta x_k \mu_k^\alpha}{r^3} - \frac{15 x_j \mu_j^\alpha x_k \mu_k^\beta x_i}{r^7} + \frac{\mu_j^\alpha \mu_j^\beta x_i}{r^5}\right). \tag{3.88}$$

We then can obtain t_T by choosing the initial separation, r_0, between particles as the characteristic lengthscale such that

$$t_T = \frac{64\pi\eta a \mu_0 r_0^5}{3\left[V\chi_\perp^E B\right]^2}. \tag{3.89}$$

We do a comparison between Eq. (3.85) and (3.89) and take the ratio, β, between them:

$$\beta = \frac{t_R}{t_T} = \frac{2}{3}\frac{a^2}{r_0^2}\frac{a^2 c}{r_0^3}\frac{\chi_\perp^E}{1-\alpha}. \tag{3.90}$$

We can see that this ratio is a function of a planar area function $\psi \sim \frac{a^2}{r_0^2}$, a volume fraction $\phi \sim \frac{a^2 c}{r_0^3}$, and a magnetic property function $\frac{\chi_\perp^E}{1-\alpha}$. If $\beta \gg 1$, the translational motion happens much faster than the rotational motion; in contrast, if $\beta \ll 1$, the rotational motion happens much faster than the translational motion.

3.6 Results and Discussions

In this section, we discuss the results of simulations. We first show some benchmarks that validate the methods we have introduced so far and also the programs that we have developed. Then, we show the results of simulations of spherical particles and aspherical particles under magnetic fields.

3.6.1 Spherical Suspension

We first show the benchmarks of a finite suspension of spheres. Suppose that seven spheres initially placed in a line and equally separated. The spheres sediment in a direction that is perpendicular to the line of center. We calculate the drag coefficient $\lambda = F/6\pi\eta aU$ of the instantaneous configuration with three different separations, $r = 2.005$, $r = 2.2$, and $r = 2.6$. Because of the symmetry, only four spheres are plotted (Fig. 3.2). Comparison with Durlofsky et al. [53] has shown good agreement. Difference arises from the error of extracting data from the plot of Durlofsky's paper [53]. The $r = 2.005$ data is closer to other data because this set of data is tabulated in the paper.

We then show the benchmark of infinite suspension of spheres, and we compute the shear viscosity of such suspension (Fig. 3.3). We compare our result with Batchelor and Green's model [73]. It has also shown good agreement.

We now move to dynamic simulations of spheres under external fields. We sim-

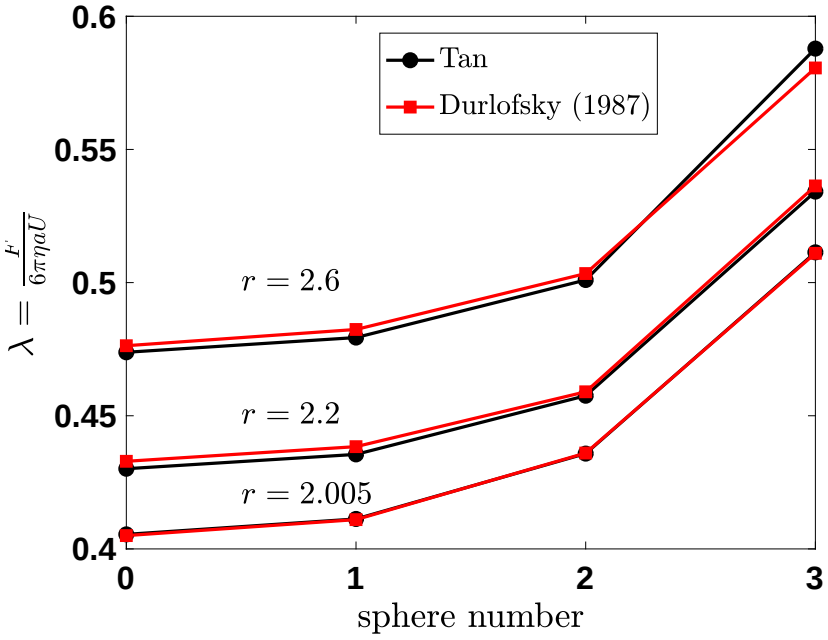

Figure 3.2: A comparison of the drag coefficient $\lambda = F/6\pi\eta aU$ with Durlofsky's paper. Three horizontal lines of seven spheres sedimenting in the vertical direction with three different separation distances, $r = 2.005$, $r = 2.2$, and $r = 2.6$. The drag coefficient is calculated using the instantaneous configuration.

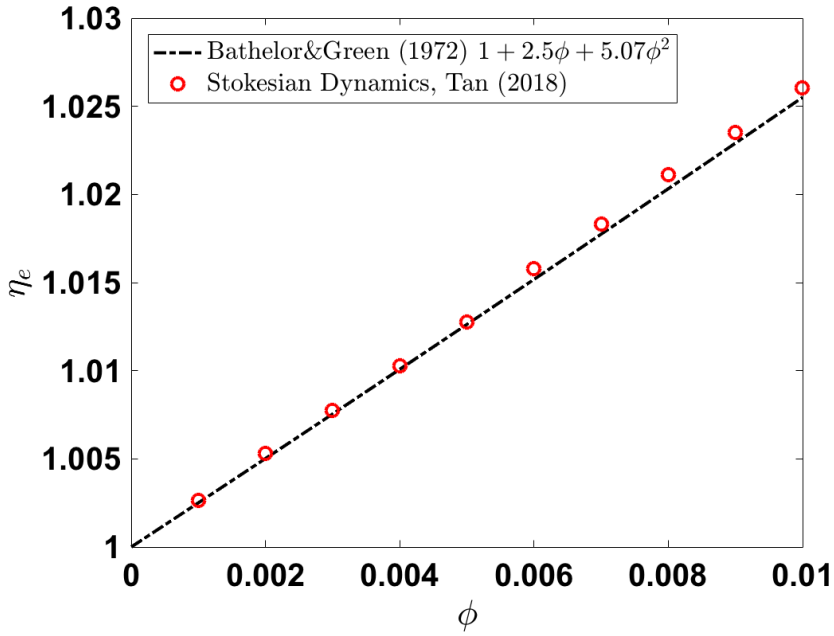

Figure 3.3: A benchmark of viscosity compared to Batchelor and Green. The calculation is completed by simulating a random suspension of 27 spheres in one simulation cell.

ulated the coarsening of spheres under a rotating magnetic field. The spheres are initially randomly positioned, and we see that hexagonal packing is formed (Fig. 3.4) at equilibrium state, which is consistent with other works and the experimental observations in our previous work.

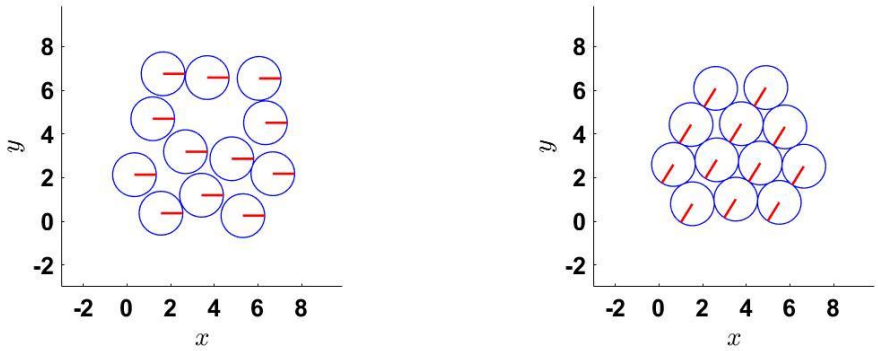

(a) Initial configuration of spheres before magnetic is field applied.

(b) Equilibrium configuration of spheres after magnetic is field applied.

Figure 3.4: A rotating magnetic field that is applied to spheres. Hexagonal packing is formed at the equilibrium state.

3.6.2 Aspherical Suspension

Again, we first show a benchmark of our result. Suppose a rod is approximated by a line of spheres. The "rod" is suspended in an unbounded fluid and translates with a velocity U, along and perpendicular to its orientation vector. We compute the drag coefficient of each case with different aspect ratio of rods. We compare the computational results with the drag coefficients from the *slender-body theory* [75],

which is

$$C_{F_1} = \frac{2}{3}\frac{1}{\log[2a/b] - 1/2}\left(1 + \mathcal{O}\left[\frac{b}{a}\right]^2\right), \text{ and} \tag{3.91a}$$

$$C_{F_2} = \frac{4}{3}\frac{1}{\log[2a/b] + 1/2}\left(1 + \mathcal{O}\left[\frac{b}{a}\right]^2\right), \tag{3.91b}$$

where C_{F_1} is the drag coefficient for flow that is directed along the orientation vector, C_{F_2} is the drag coefficient for flow that is directed perpendicular to the orientation vector, b is half the minor axis (the radius of sphere in our simulation), and a is half the major axis (the number of spheres in our simulation). The comparison is shown in Fig. 3.5. We can see that the computational result using the Stokesian dynamics combined with Eq. (3.81) agree well with the slender-body theory, and as the aspect ratio increases, the comparison becomes better.

We then simulate the chaining of two "disks" using the assembly of spheres under two different values of β. The initial and final configurations of two disks can be found in Fig. 3.6. The magnetic field rotates in the (x, y)-plane. Initially, we put the right disk out of plane and the left disk in plane. After the magnetic field is applied, both disks are aligned in the plane, and they are linked up by magnetic attraction. Figure 3.7 shows the dynamics of rotation (Fig. 3.7(a)) and translation (Fig. 3.7(b)) at $\beta = 0.1$. We see that, at a low value of β, the rotational motion dominates, and the translational motion is about 3 orders of magnitude slower. Figure 3.8 shows the dynamics of rotation (Fig. 3.8(a)) and translation (Fig. 3.8(b)) at $\beta = 10$. We see that, at a high value of β, the timescales of both

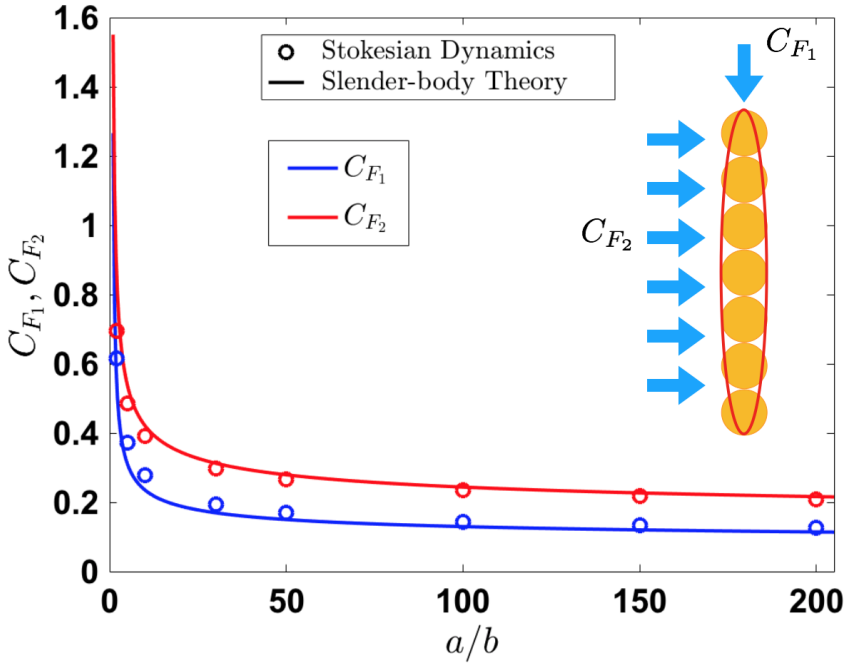

Figure 3.5: A comparison of drag coefficients between computation and slender-body theory. A range of aspect ratios is shown, and computational results agree well with the slender-body theory.

the rotational and translational motions are at the same order of magnitude.

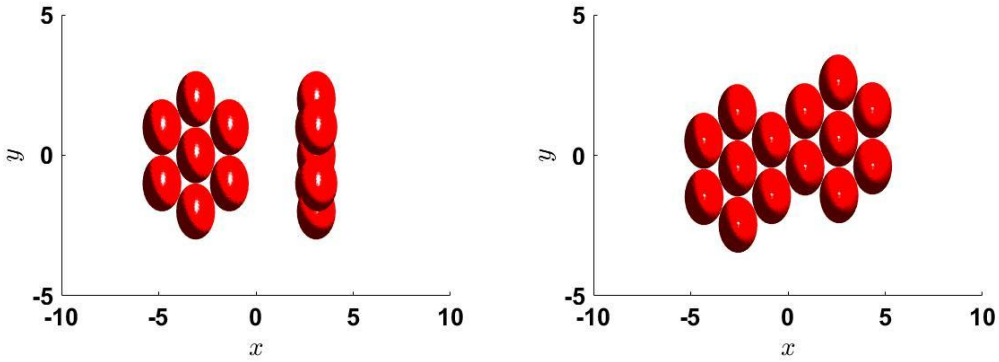

(a) Initial configuration of two disks. (b) Final configuration of two disks.

Figure 3.6: Configurations of two disks under a rotating magnetic field. Initially, the right disk is aligned out of plane and the left disk is aligned in plane. Finally, both disks are aligned in the plane, and they become linked.

This part is still under investigation. For example, a method of large-scale simulation needs to be developed to simulate a system of high-aspect-ratio particles and/or a high-volume-fraction of particles.

3.7 Conclusions

In this chapter, we first introduced the hydrodynamic interactions between particles. We discussed the elements required for building the code of Stokesian dynamics. Then, we compared our results of simulations with the results of other researchers who used the Stokesian dynamics to validate our method. With confidence of our code, we simulated the dynamics of spherical particles in magnetic

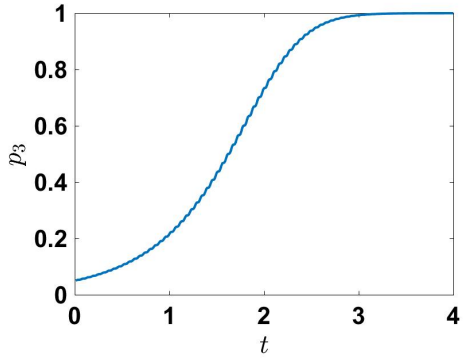

(a) Orientation vector, p_3, as a function of time at $\beta = 0.1$.

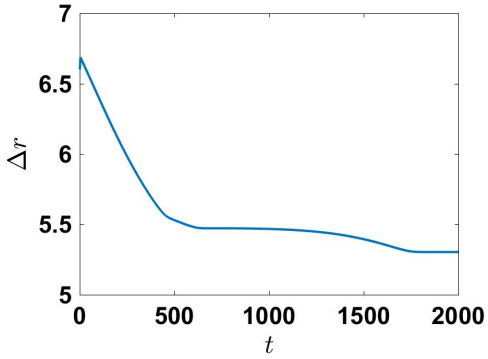

(b) Separation between disks as a function of time at $\beta = 0.1$.

Figure 3.7: The change of orientation and separation as a function of time at $\beta = 0.1$. At a low value of β, the rotational motion dominates, and the chaining is much slower than the alignment.

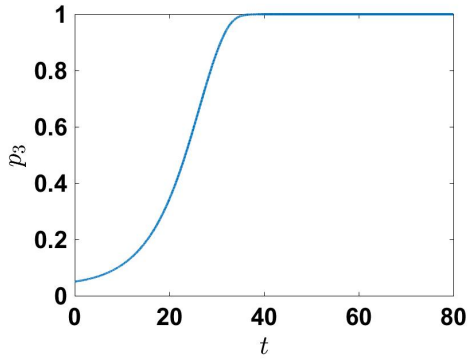

(a) Orientation vector, p_3, as a function of time at $\beta = 10$.

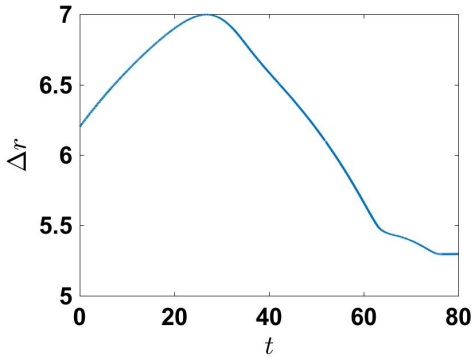

(b) Separation between disks as a function of time at $\beta = 10$.

Figure 3.8: The change of orientation and separation as a function of time at $\beta = 10$. At a high value of β, the translational motion dominates, and the chaining and the alignment are at about the same timescale.

fields. Finally, we extend our simulation of spherical suspensions to aspherical suspensions by using spheres as constituting components of other geometries. This method is validated by comparison with slender-body theory.

Chapter 4

Microrheological Study of Artificial Sputum Medium + Xanthan Gum

4.1 Introduction to Microrheology

In this chapter, we will move to a new topic that focuses on the experimental aspect of rheology, however, the fundamental physics are the same with the previous

chapters.

Rheology is a study of the mechanical properties of complex fluids. The conventional rheology usually places the sample between two solid boundaries and *steadily shear* or *oscillate* one boundary, and a responding stress is obtained. For example, if a steady shear, $\dot{\gamma}$, is applied and the responding stress, σ, is measured, the viscosity can be obtained such that

$$\eta = \frac{\sigma}{\dot{\gamma}}. \tag{4.1}$$

Or, an oscillatory strain, $\gamma(t) = \gamma_0 e^{i\omega t}$, is applied and the responding oscillatory stress, $\sigma(t) = \sigma_0 e^{i(\omega t+\delta)}$, is measured, the complex modulus, $G^*(\omega)$, is obtained such that

$$G^*(\omega) = \frac{\sigma}{\gamma}. \tag{4.2}$$

We can write the complex modulus as a real part plus an imaginary part such that

$$G^*(\omega) = G'(\omega) + iG''(\omega), \tag{4.3}$$

where $G'(\omega)$ is the *elastic* or *storage* modulus that represents the part of stress that is recoverable in the material, and $G''(\omega)$ is the *viscous* or *loss* modulus that represents the part of stress that is dissipated in the material. We can write the

modulus as

$$G'(\omega) = \frac{\sigma_0}{\gamma_0} \cos\delta(\omega), \text{ and} \tag{4.4a}$$

$$G''(\omega) = \frac{\sigma_0}{\gamma_0} \sin\delta(\omega), \tag{4.4b}$$

where $\delta(\omega)$ is the *phase lag*. For a Newtonian fluid, $\delta = \frac{\pi}{2}$, and for a Hookean solid, $\delta = 0$. Conventional rheology uses the probe whose lengthscale is of centimeters, which is significantly larger than the characteristic lengthscale (ranging from nanometer to micrometer) of complex fluids' microstructures. Thus, it probes the *averaged* properties. Conventional rheology fails to map out the *heterogeneity* of the material therefore. Moreover, conventional rheological measurement usually requires the sample size to be milliliters, which can be prohibitive to obtain for expensive materials like biological fluids.

Microrheology, however, is able to probe the heterogenous environment of the material, and only requires microliters of sample. Microrheology investigates the rheological properties of the materials using nano or microparticles that are embedded in the materials. The motion of the probing particles can be driven by the thermal energy of the fluid, called *passive microrheology*, or by an external field like magnetic or optical field, called *active microrheology*. The motion of the particles can be related to the rheological properties of the materials by using *generalized Stokes-Einstein relation* (GSER) [76] which will be discussed later. The early microrheological study can date back to about one century ago, when researchers

applied magnetic field to move magnetic fillings in the material. Heilbronn [77] measured the viscosity of protoplast by using a magnetic field to drive iron particles. Seifriz used the similar technique to measure the mechanical responses of gelatin [78] and sand dollar eggs [79]. The fundamentals of the passive microrheology, on the other hand, can date back to a even earlier time, when Einstein [80] published his paper on a theoretical treatment of the *Brownian* motion, which was observed by Robert Brown [81]. Einstein's theory was later confirmed by Jean Perrin's painstaking experiments with his students [82], which led to his Nobel Prize in physics.

4.1.1 Generalized Stokes Einstein Relation

Generalized Stokes Einstein relation (GSER) is an extension of the Stokes Einstein relation to relating the diffusion of the particles to the viscoelastic properties of the materials. Before discussing GSER, we start with Einstein's theory that relates particles' Brownian motions to the viscosity of the fluid.

Suppose that a species is concentrated at the origin at time $t = 0$. After an amount of time, the paticles will diffuse into the space, and we can build a conservation equation such that

$$\frac{\partial \mathcal{P}(\mathbf{x}, t)}{\partial t} + \boldsymbol{\nabla} \cdot \mathbf{j}_D(\mathbf{x}, t) = 0, \tag{4.5}$$

where $\mathcal{P}(\mathbf{x}, t)$ is the probability of finding the particle at position $\mathbf{x}$ and at time t, and $\mathbf{j}_D$ is the flux of mass due to diffusion. We can write the flux as the gradient

of concentration according to *Fick's law* such that

$$\mathbf{j}_D = -\boldsymbol{\nabla}\mathcal{P}, \tag{4.6}$$

and substituting the flux into the conservation equation yields

$$\frac{\partial \mathcal{P}\left(\mathbf{x}, t\right)}{\partial t} - \nabla^2 \mathcal{P}\left(\mathbf{x}, t\right) = 0, \tag{4.7}$$

with the initial condition $\mathcal{P}\left(\mathbf{x}, t = 0\right) = \delta\left(\mathbf{x}\right)$. The probability can be solved to be a Guassian distribution such that

$$\mathcal{P}\left(\mathbf{x}, t\right) = \frac{1}{\left[4\pi D t\right]^{\mathbb{d}/2}} \exp\left[-\frac{\Delta r^2}{4Dt}\right], \tag{4.8}$$

where $\mathbb{d}$ is the dimensionality, and Δr is the displacement such that $\Delta r = \|\mathbf{x}\|$. Note that the probability is imposed to be normalized such that

$$\int_{-\infty}^{+\infty} \mathcal{P}\left(\mathbf{x}, t\right) d\mathbf{x} = 1, \tag{4.9}$$

and the mean displacement is zero,

$$\left\langle \Delta r\left(t\right)\right\rangle = \int_{-\infty}^{+\infty} \Delta r\left(t\right) \mathcal{P}\left(\mathbf{x}, t\right) d\mathbf{x} = 0. \tag{4.10}$$

In fact, the mean squared displacement (MSD) is the quantity that is needed.

Multiplying Eq. (4.7) by $\Delta r^2(t)$ and integrating over the whole space gives

$$\frac{\partial}{\partial t}\int_{-\infty}^{+\infty}\Delta r^2\left(t\right)\mathcal{P}\left(\mathbf{x},t\right)d\mathbf{x}=D\int_{-\infty}^{+\infty}\Delta r^2\left(t\right)\nabla^2\mathcal{P}\left(\mathbf{x},t\right)d\mathbf{x}. \tag{4.11}$$

The LHS of the equation is simply $\frac{\partial\left\langle \Delta r^2(t)\right\rangle}{\partial t}$. Applying partial integration to the RHS, we can obtain

$$\frac{\partial\left\langle \Delta r^2\left(t\right)\right\rangle}{\partial t}=2\mathbb{d}D, \tag{4.12}$$

or,

$$\left\langle \Delta r^2\left(t\right)\right\rangle =2\mathbb{d}Dt. \tag{4.13}$$

The diffusivity D can be found by using the Stokes Einstein relation of Newtonian fluid,

$$D=\frac{k_BT}{6\pi\eta a} \tag{4.14}$$

By relating Eqs. (4.13) and (4.14) we have built a relationship between the motion of the particle $\langle\Delta r^2\left(t\right)\rangle$ and the property of the fluid η.

Now we move to deriving the GSER. We start with the Langevin equation considering translational motion only,

$$m\frac{d\mathbf{U}}{dt}=\mathbf{F}^H+\mathbf{F}^B. \tag{4.15}$$

In an isotropic viscoelastic fluid, we can write the hydrodynamic force $\mathbf{F}^H$ as [76]

$$\mathbf{F}^H = -\int_0^t \zeta\left(t-t'\right)\mathbf{U}\left(t'\right)dt', \tag{4.16}$$

where $\zeta\left(t-t'\right)$ is a memory function that describes the local viscoelastic responses at time t as the stress imposed on the fluid prior to the time t. Then, the Langevin equation in a viscoelastic fluid becomes,

$$m\frac{d\mathbf{U}}{dt} = --\int_0^t \zeta\left(t-t'\right)\mathbf{U}\left(t'\right)dt' + \mathbf{F}^B. \tag{4.17}$$

Taking a unilateral Fourier transform to Eq. (4.17) we have

$$-m\mathbf{U}\left(0\right) + mi\omega\widetilde{\mathbf{U}}\left(\omega\right) = \widetilde{\mathbf{F}}^B\left(\omega\right) - \widetilde{\zeta}\left(\omega\right)\widetilde{\mathbf{U}}\left(\omega\right). \tag{4.18}$$

Rearranging the equation and isolating $\widetilde{\mathbf{U}}\left(\omega\right)$ gives

$$\widetilde{\mathbf{U}}\left(\omega\right) = \frac{\widetilde{\mathbf{F}}^B\left(\omega\right) + m\mathbf{U}\left(0\right)}{\widetilde{\zeta}\left(\omega\right) + mi\omega}. \tag{4.19}$$

Multiplying the equation by $\mathbf{U}\left(0\right)$ and taking average, we obtain the Fourier transform of the velocity autocorrelation function (VAC) such that

$$\left\langle \mathbf{U}\left(0\right)\cdot\widetilde{\mathbf{U}}\left(\omega\right)\right\rangle = \frac{\left\langle \widetilde{\mathbf{F}}^B\left(\omega\right)\cdot\mathbf{U}\left(0\right)\right\rangle + m\left\langle \mathbf{U}\left(0\right)\cdot\mathbf{U}\left(0\right)\right\rangle}{\widetilde{\zeta}\left(\omega\right) + mi\omega}. \tag{4.20}$$

Because the Brownian force is assumed to have zero mean and uncorrelated with the velocity of particle, $\left\langle \widetilde{\mathbf{F}}^B\left(\omega\right)\cdot\mathbf{U}\left(0\right)\right\rangle = 0$. In thermal equilibrium, the equipartition theorem states that the kinetic energy of each independent degree of freedom

is equal to $\frac{1}{2}k_BT$, therefore,

$$m\left\langle \mathbf{U}\left(0\right)\mathbf{U}\left(0\right)\right\rangle = \mathbb{d}k_BT. \tag{4.21}$$

The inertia of the particles can be neglected for small particles and so $mi\omega = 0$. The Fourier transform of VAC becomes

$$\left\langle \mathbf{U}\left(0\right)\cdot\widetilde{\mathbf{U}}\left(\omega\right)\right\rangle = \frac{\mathbb{d}k_BT}{\widetilde{\zeta}\left(\omega\right)}. \tag{4.22}$$

Analogous to a spherical particle suspended in a Newtonian fluid, we can define the memory function of a spherical particle in a viscoelastic fluid to be

$$\widetilde{\zeta}\left(\omega\right) = 6\pi a\eta^*\left(\omega\right), \tag{4.23}$$

where η^* is the complex viscosity which is related to the complex modulus such that

$$G^*\left(\omega\right) = i\omega\eta^*\left(\omega\right). \tag{4.24}$$

By substituting Eqs. (4.23) and (4.24) into Eq. (4.22) and isolating the complex modulus gives

$$G^*\left(\omega\right) = \frac{\left(i\omega\right)\mathbb{d}k_BT}{6\pi a\left\langle \mathbf{U}\left(0\right)\cdot\widetilde{\mathbf{U}}\left(\omega\right)\right\rangle}. \tag{4.25}$$

The VAC can be expressed in terms of the Fourier transform of MSD such that

$$\mathscr{F}_u\left\{\left\langle \Delta r^2\left(t\right)\right\rangle\right\} = \frac{2}{\left(i\omega\right)^2}\left\langle \mathbf{U}\left(0\right)\cdot\widetilde{\mathbf{U}}\left(\omega\right)\right\rangle, \tag{4.26}$$

and substituting it into Eq. (4.25) yields the GSER

$$G^*\left(\omega\right) = \frac{\mathbb{d}k_BT}{3\pi a\left(i\omega\right)\mathscr{F}_u\left\{\left\langle \Delta r^2\left(t\right)\right\rangle\right\}}. \tag{4.27}$$

In this study $\mathbb{d}$ is chosen to be 2 as the positions of particles are projected on a two-dimensional image, so that

$$G^*\left(\omega\right) = \frac{2k_BT}{3\pi a\left(i\omega\right)\mathscr{F}_u\left\{\left\langle \Delta r^2\left(t\right)\right\rangle\right\}}. \tag{4.28}$$

Now we need a model for the MSD that can be transformed from the time domain to the frequency domain. A commonly used model is the power-law function. The MSD can be expanded locally at a frequency of interest, ω_0 [83], such that

$$\left\langle \Delta r^2\left(t;\omega_0\right)\right\rangle = \left\langle \Delta r^2\left(\omega_0\right)\right\rangle\left[\omega_0 t\right]^{\alpha(\omega_0)}, \tag{4.29}$$

where α is the diffusive exponent [84]. In a Newtonian fluid, $\alpha = 1$; in a Hookean solid, $\alpha = 0$, and in a viscoelastic fluid, $0 < \alpha < 1$, as shown in Fig. 4.1. The unilateral Fourier transform of MSD thus becomes

$$\mathscr{F}_u\left\{\left\langle \Delta r^2\left(t\right)\right\rangle\right\} = \frac{\mathit{\Gamma}[1+\alpha(\omega_0)]}{i\omega}\left\langle \Delta r^2(t_0)\right\rangle\exp\left[\frac{i\pi\alpha(\omega_0)}{2}\right]. \tag{4.30}$$

Therefore, Eq. (4.28) becomes

$$G^*(\omega_0) = \frac{2k_BT}{3\pi a \left\langle \Delta r^2(t_0) \right\rangle \Gamma[1+\alpha(\omega_0)]} \exp\left[\frac{i\pi\alpha(\omega_0)}{2}\right]. \tag{4.31}$$

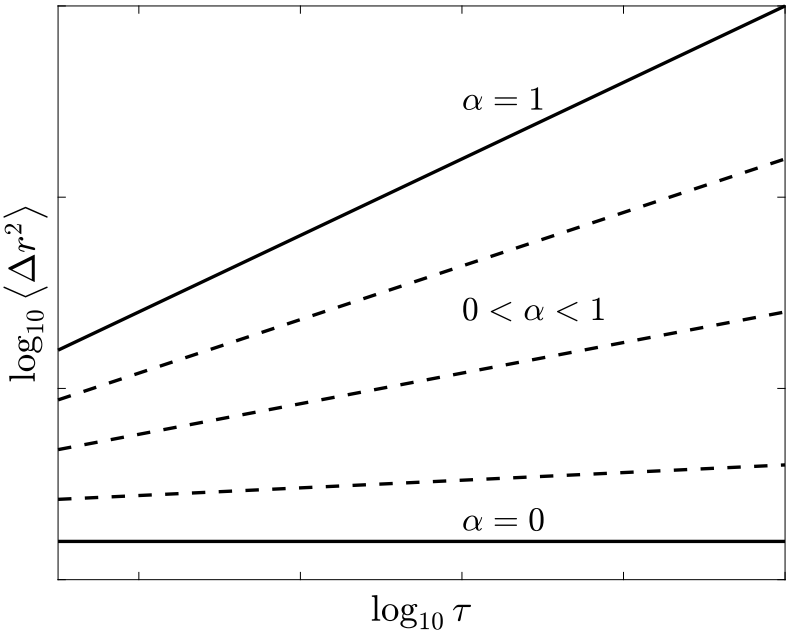

Figure 4.1: The MSD of different kinds of materials. For a Hookean solid, the diffusive exponent α is 0. For a Newtonian fluid, the diffusive exponent α is 1. For a viscoelastic fluid, the diffusive exponent α is between 0 and 1.

The GSER builds a relationship between the rheological property $G^*(\omega)$ and a experimentally measurable quantity, $\langle \Delta r^2(t) \rangle$. The GSER has been widely used microrheological studies of viscoelastic materials. However, here are a few things

need to be noted in using GSER.

First, the assumption underlying the Einstein's part is that the system is at equilibrium. If a material is continuously driven out of equilibrium by external force, by active materials such as molecular motors in biopolymers, or by evolving of the material itself, Eq. (4.21) may fail. However, if the active changing of the state is much slower than the sampling window, the system can be treated as *quasi-steady*, and the equilibrium state is assumed to be valid during the sampling window.

Second, the assumption underlying the Stokes' part is that the material behaves like a continuum relative to the particle. The particle's size should be much larger than the lengthscale of the microstructure of the material so the probed properties are bulk properties (see Fig. 4.2(a)). Many viscoelastic materials are heterogeneous, and the microstructures can have different lengthscales. The particle can probe the heterogeneous properties when the particle's size is larger than the lengthscale of any microstructure, but when the particle's size is smaller than the lengthscale of the microstructure, the particle may just diffuse through the void space of the networks (see Fig. 4.2(c)). Beside the effect of particle's size, the surface chemistry of the particle can also have an effect on the continuum surrounding the particle. The microstructure can be depleted or accumulated around the particle, depending on the interactions between the microstructure and the particle's surface chemistry. A systematic microrheological study usually requires using a range of sizes and surface chemistries of particles and comparing the results

with the bulk rheological measurements. Whether the continuum assumption is broken down or not, the microrheological measurement can be always useful. In developing targeting drug-delivery vehicle, the vehicle should be able to diffuse through the fluid to the desired site. The efficient transport phenomena is for the vehicle to diffuse through the interstitial space like diffusing in a Newtonian fluid. Besides, if the material exhibits anisotropic properties, like liquid-crystal, the use of GSER becomes more complicated. Although the Stokes' part is still valid, the construction of the memory function ζ should take the orientation of the material into account.

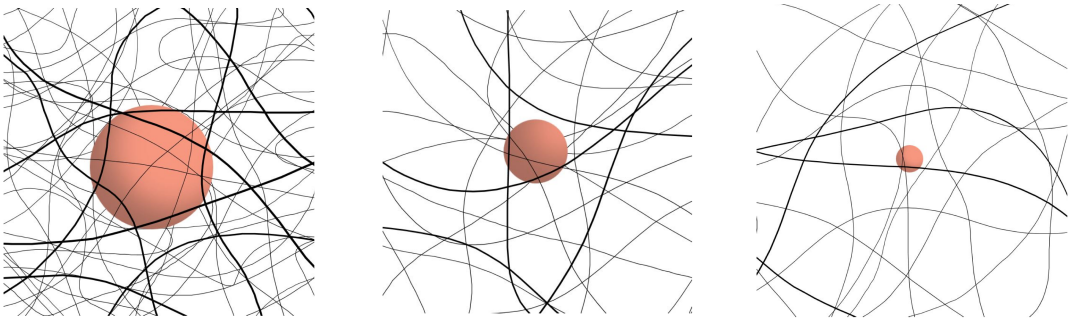

(a) Particle size much greater than mesh size.

(b) Particle size approximates mesh size.

(c) Particle size much smaller than mesh size.

Figure 4.2: The relative size of the probe's size and the size of the mesh.

4.1.2 Techniques of Microrheology

Depending on the driven force on the probing particle, microrheology can be categorized into two aspects — *passive* and *active*, as mentioned before. Passive microrheology is mainly used in this chapter and active microrheology, or specifi-

cally *magnetic tweezers*, is applied in the study in Chapter 5. In this section, we will discuss the techniques used in microrheological measurements.

We have discussed the fundamental theories underlying the passive microrheology. A passive microrheological measurement usually tracks the motions of the particles and obtain the MSD. Several techniques are used in passive microrheology, such as multiple particle tracking [84,85], diffusing wave spectroscopy [76,86], and laser tracking [83], the later two of which can have high-frequency (kHz – MHz) measurements. Multiple particle tracking is used in this study and will be introduced in details later.

The two most widely used active microrheology techniques are *magnetic tweezers* and *optical tweezers*. Magnetic tweezers apply an external magnetic field, which can be constant, impulsive, or oscillatory, to magnetic microparticles embedded in the materials. A beam of photons is exerted on the particles and the momentum carried by the photons can move the particles. The forces generated by the optical tweezers are usually weaker than the magnetic tweezers, while the positions captured by the optical tweezers can be more precise when combined with interferometric technique. Magnetic tweezers are used in Chapter 5 to measure the microscopic *yield-stress*, and this technique will be discussed in details later.

Multiple Particle Tracking

A multiple particle tracking setup usually includes a light microscope, a CCD camera attached to the microscope to record the positions of the particles, and a computer that stores the captured frames and carries out image analysis (see Fig. 4.3, reprinted with the permission of Mao [87]). Because of its easy implementation, multiple particle tracking is widely used in microrheology. Fluorescent microscopy is preferred to bright-light microscopy because a clearer brightness distribution can be obtained from fluorescent microscopy and can be easier for image analysis. Improved techniques such as confocal microscopy or near-field illumination have been used to obtain the location of particles with higher precision by reducing the background fluorescence noise. In this study, fluorescent microscopy is used where microparticles tagged with yellow/green fluorescence are embedded in the materials.

In a multiple particle tracking measurement, hundreds of particles can be recorded simultaneously to ensure the statistical accuracy, or the sampling time can be made longer if fewer particles are located in each frame because of the ergodicity of the system. After the images are captured, the post-process usually includes *image filtering*, *centroid locating*, and *trajectories linking* following the methods proposed by Crocker & Grier [85].

Image Filtering A typical image of captured by the CCD camera on a fluorescent

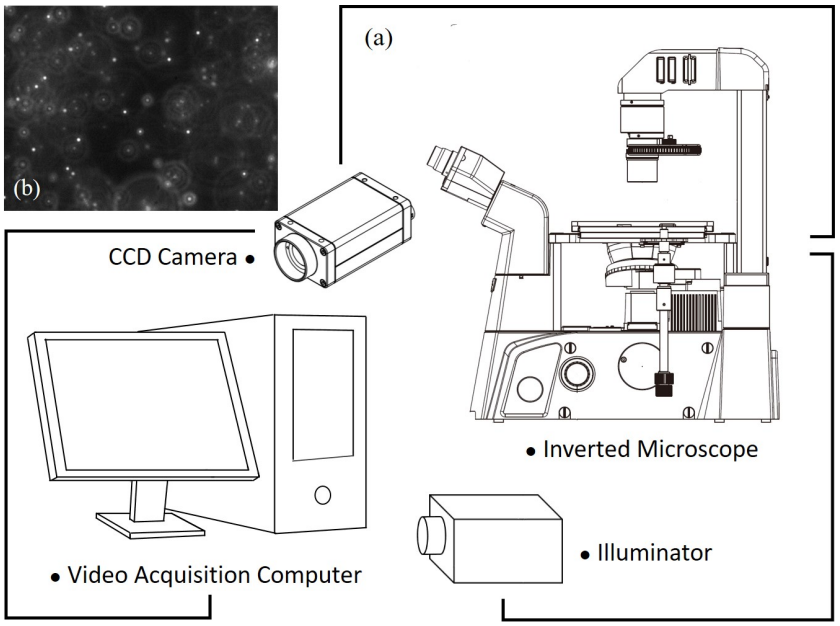

Figure 4.3: A typical setup of multiple particle tracking experiment. It includes a microscope, a camera connected to the microscope, and a computer.

microscope contains bright circles as the fluorescent particles, dark background, and noise. The sources of noise usually includes the imperfect transfer from photon to electron of CCD camera's sensor and independent readout noise [88]. First, a background image is constructed by convoluting the raw image with a constant kernel of size $2w_1+1$, where w_1 is slightly larger than the particle's radius in pixels and smaller than the interparticle's separation. Let $A_{i,j}$ represent the brightness value located at (i,j) on the original image matrix, and $B_{i,j}$ is the background after the convolution

$$B_{i,j} = \frac{1}{(2w_1+1)^2} \sum_{|m|\leq w_1} \sum_{|n|\leq w_1} A_{i+m,j+n}. \tag{4.32}$$

Second, the raw image is convoluted with a Gaussian kernel. The smoothed image $G_{i,j}$ after the convolution is

$$G_{i,j} = \left[\sum_{|m| \le w_1} e^{-m^2/4} \right]^{-2} \sum_{|m| \le w_1} \sum_{|n| \le w_1} A_{i+m,j+n} e^{-\left(m^2+n^2\right)/4}. \tag{4.33}$$

The final image ready for next processing is thus the Gaussian smoothed image subtraction the background image

$$\widetilde{A}_{i,j} = G_{i,j} - B_{i,j}. \tag{4.34}$$

The original and filtered images are shown in Fig. 4.4.

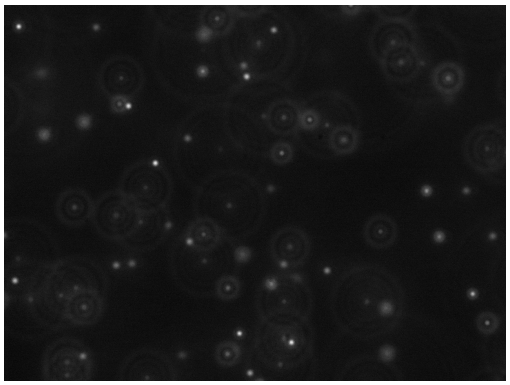

(a) Original picture taken by a CCD camera.

(b) Image processed by two low-pass filters.

Figure 4.4: A comparison of two images — original image taken by a CCD camera and filtered image.

Centroid Locating The local maxima of brightness are assumed to be close to the centroids of the particles. The location of the estimated centroid is denoted by

(x_0, y_0). A pixel is adopted as the centroid if the brightness value of no other pixels within a distance w_2 is larger, where w_2 is larger than the radii of the particles and smaller than the interparticle's separation. In reality, however, the brightness distribution is not perfectly symmetric with respect to the local maxima. We need to carry out a brightness-weighted calculation to refine the centroids of the particles. The calculated offset (ϵ_x, ϵ_y) is given by

$$\begin{pmatrix} \epsilon_x \\ \epsilon_y \end{pmatrix} = \frac{1}{\sum_{m^2+n^2 \le w_2^2} \widetilde{A}_{x_0+m, y_0+n}} \sum_{m^2+n^2 \le w_2^2} \begin{pmatrix} m \\ n \end{pmatrix} \widetilde{A}_{x_0+m, y_0+n}. \tag{4.35}$$

Then, the refined location (x, y) is the initial estimate (x_0, y_0) plus the offset (ϵ_x, ϵ_y).

Trajectories Linking Next we need to link the located centroids into trajectories. A located particle is assigned with a label in a frame, and the same label is assigned to this particle in the next frame, if the particle moves within a distance w_3 relative to the previous frame. The positions of the particle with the same label will later be linked together. The value of w_3 should be chosen smaller than the interparticle's separation; otherwise, the labels of two particles may be exchanged.

In multiple particle tracking experiments, the positions of the particles are projected on a two-dimensional image and a two dimensional ($\mathbb{d} = 2$) MSD is calculated. With the knowledge of the positions of particles, we are now able to

calculate the MSD. To increase the statistical accuracy, we calculate the ensemble average MSD for a time step Δt such that

$$\left\langle \Delta r^2 \left(\Delta t; t \right) \right\rangle = \frac{1}{N} \sum_{\alpha=1}^{N} \left[x^\alpha \left(t + \Delta t \right) - x^\alpha \left(t \right) \right]^2 + \left[y^\alpha \left(t + \Delta t \right) - y^\alpha \left(t \right) \right]^2 . \quad (4.36)$$

Magnetic Tweezers

The earliest microrheological study utilized the magnetic tweezers [77–79]. While the modern experiements were carried out by Ziemann [89], who used both constant and oscillatory fields to move the *paramagnetic* microparticles. A typical magnetic-tweezers setup includes a coil made of an iron core wrapped with electrical wires, a function generator that generates different signals, an amplifier, paramagnetic particles, and a microscope setup that observes and records the motions of particles.

Based on the number of coils, the magnetic tweezers can be categorized into single-pole, double-pole and higher number of poles. Single-pole magnetic tweezers, as the name suggests, involves one set of coil. Single-pole coil imposes a constant or impulsive force to the magnetic particle, and the *creep compliance* can be measured [90, 91]. The yield stress of a material can also be measured by gradually increasing the strength of the field until a motion of the particles is observed [4, 92] . Double-pole coils can oscillate the particles with different frequen-

cies [89]. In opposite with the oscillatory measurement in conventional rheology and passive microrheology, where an frequency-dependent strain is imposed and the frequency-dependent stress is measured, oscillatory magnetic tweezers impose a frequency-dependent stress and the strain is measured. But essentially they are the same.

A calibration of the magnetic tweezers is usually carried out in a viscosity-standard Newtonian fluid. The force is calculated by tracking the motion of the particles and then using the Stokes law. Voltages or currents are changed to obtain the voltage- or current-dependent magnetic force. The magnetic force also depends on the positions of the particles relative to the electromagnetic coils, so a map of force is obtained. After the calibration, the voltage or current and the position are the input parameters to get the magnetic forces in a microrheological measurement.

At this point, we have discussed the fundamental theories underlying the microrheology and the techniques used to do the experiments. The rest of this chapter focuses on the application of passive microrheology to study the rheological properties of artificial sputum medium (ASM) plus xanthan gum (XG). ASM plus XG is a mixture that our lab developed to be a cheap substitute of mucus of *cystic fibrosis* (CF) patients such that their bulk rheological properties are comparable. The application of magnetic tweezers will be applied in Chapter 5.

4.2 Introduction to the Rheology of Mucus

Mucus is a biological fluid secreted in different sites of body, such as respiratory, gastrointestinal, urogenital, visual, and auditory systems of mammals, as well as the epidermis of amphibians, the gills of fish, and the external coating of snails and slugs. This complex fluid provides protection by humidifying and lubricating surfaces and by selectively obstructing transport of particles through a permeable film. Mucus is often found to be a viscoelastic conglomeration at a macroscopic lengthscale (> 1 mm). Mucus is composed of water ($\geq 95\%$), mucins ($\geq 2\%$), salts and cellular debris [93]. Mucins, which contribute to 80% of the dry weight in mucus [94], are secreted by the goblet cells of the surface epithelium and by the mucous and serous cells of the submucosal glands [95]. The microstructure of mucus is formed primarily by the entanglement of mucin fibers and other constituents of mucus [96], along with waker non-cavalent [97] and stronger disulfide bonds [98], creating a weak hydrogel.

Macroscopic (or bulk) rheological studies of mucus that use measure the properties at a lengthscale on the order of centimeters have shown that its viscosity is usually very high at low shear rates, 10^4- to 10^6-times larger than the viscosity of water. At high shear rates near the physiological maximum, the viscosity of mucus was shown to decrease drastically to a value close to the viscosity of water [98]. Chen et al. [99] used a double-tube capillary viscoelastometer to characterize the sputa of bronchitic patients, finding the viscosity to be 100 to 300 Pa·s, and the elastic

modulus to be 1 to 2.5 Pa [100].

Compared with the bulk rheology of mucus, studies of microrheology have reported significantly different rheological properties. Since mucus has a heterogeneous micro- or nano-environment, nanoparticles have shown to diffuse through the interstitial space that is surrounded by the microstructure of mucin at rates that are significantly higher than the predictions that are based on the bulk rheology. For instance, the Norwalk virus (*Norovirus*) with a size of 38 nm and the *human papillomavirus* (HPV) with a size of 55 nm were found to diffuse in human cervical mucus with the same diffusion rate as in water. It shows that a size on the order of 10 nm, the continua of the microstructure of mucus break down. In contrast, the herpes simplex virus (HSV) with a size of 180 nm diffuses 100- to 1000-times slower in mucus than in water [101]. When the size of the particle is about the same with the lengthscale of the microstructure, particles were found to be able to hop between elastic cages [102], which was also observed in this study.

As mentioned in the previous section, beside the effect of the size of probing particles, the surface chemistry is another important factor that would affect the measurement. For instance, 200 nm particles of polystyrene that were coated with low-molecular-weight polyethylene glycol (PEG) were found to diffuse through sputum of a CF patient with a rate 90 times the uncoated particles with the same size. The viscosity calculated according to the diffusion rate was found to be 0.00005 times the bulk rheological measurement [103]. The result shows that PEG on the

surface creates depleted space by pushing the microstructure of mucins away.

Cystic fibrosis is a genetic disease that is caused by mutations in the cystic fibrosis transmembrane conductance regulator (CFTR) gene, which leads to an improper regulation of ions and to reduced water content [104].The respiratory mucus of CF patients has unusually high rheological properties, resulting in the obstruction of mucociliary clearance, the colonization of bacteria, and finally severe infection [105,106], which is exacerbated by difficulty of delivering antibiotics to the infected site or genetic medicine to the epithelium.

The transport of particles to the underlying tissue is largely hindered by the microstructure of the mucus, which presents rheologically at the macroscopic scale as a high viscoelastic modulus. However, detailed characterization of the viscoelastic properties of CF mucus at a microscopic lengthscale should promote the development of efficient drug-delivery vehicles. By probing with 100 nm and 200 nm particles, Dawson et al. [2] found that the viscosity of CF sputum at the microscale was at least an order of magnitude lower than the bulk viscosity that was measured by a cone-and-plate rheometer. Using the data from Dawson et al., we compared the bulk and microscopic rheological properties of CF sputum, as shown in Fig. 4.5. The discrepancy in diffusivity and subsequent rheology between the bulk rheology and the microscopic rheology increased to more than two orders of magnitude as the particle size decreased to 100 nm. Thus, the range in the rates of particle transport indicated that the mesh size of the CF sputum was not homogeneous.

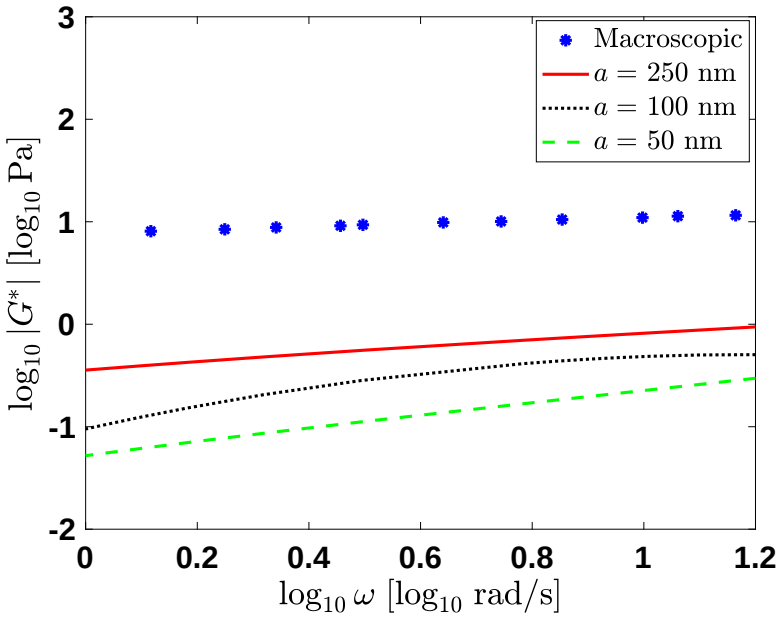

Figure 4.5: Comparison of $|G^*|$ between macroscopic and microscopic rheology from Dawson et al. A torsional rheometer with cone-and-plate geometry was used. Multiple particle tracking was used for the microrheology.

Interestingly, some researchers have shown that nanoparticles can diffuse more easily through CF sputum with a higher viscoelastic modulus [107]. The authors hypothesized that an increased viscoelastic moduli indicated an increase in biopolymer concentration and a subsequent increase in the number of junctions between the biopolymer chains. Further, they theorized that this structural change in the biogel could lead to local phase separation in the microstructural environment, which resulted in porous voids that provided paths for decreased resistance to diffusion.

These documented observations provide evidence for the need to design drug-delivery vehicles that are engineered to efficiently navigate the microstructure. Unfortunately, samples of CF sputum that are obtained from the pulmonary system of patients are difficult to obtain. The invasive collection of CF sputum can be harmful to the donors, while noninvasive methods of collection can result in contamination of the sample or in altering of the microstructure. To enable continued research into techniques of delivery while overcoming this inaccessibility of CF sputum, this study investigated a recipe for a synthetic biofluid that had consistent rheological properties of pulmonary mucus from a patient with CF.

Synthetic biofluids provide a cheaper and less-invasive alternative to real biofluids for conducting a variety of research activities. However, consistency of critical mechanical properties between the synthetic biofluids and the real biofluids is essential for properly staging a number of biophysical processes.

A variety of recipes for synthetic mucus can be found in the literature. To mimic tracheal mucus, Hamed et al. [108] used phosphoglycerate mutase (PGM) type III and a solution of albumin with glutaraldehyde as a cross-linking agent to tune the viscoelasticity of the synthetic fluid. Hassan et al. [109] crosslinked locust bean gum (LBG) solution with Borax of two concentrations to make liquid-like mucus and solid-like mucus. However, since actual mucus is composed primarily of entangled fibers of mucins with associative bonds instead of cross-linked polymers, mucus will recover rapidly and reversibly upon shear [96, Chapter 4]. Schenck

et al. [110] used Carbopol poly(acrylic acid) to create hydrogels that mimic lung mucus. Dynamic oscillatory shear tests show that both elastic and viscous moduli have a sharp increase at a frequency of 10 rad/s. This erratic behavior indicates that the structure of the gel degrades at a high frequency, which is inconsistent with CF sputum. Sriramulu et al. [1] made artificial sputum medium (ASM) to emulate CF mucus. In Sriramulu's study, ASM served as a growth medium for *Pseudomonas aeruginosa* to simulate the infected status of CF mucus [1]. However, the viscoelastic moduli of ASM can easily be shown to be 3 to 4 orders of magnitude lower than the viscoelastic moduli of the real CF sputum that was reported by Dawson et al. [2]

In this chapter we investigate both the bulk and microscopic rheological properties of an enhanced recipe of ASM that includes varying concentrations of xanthan gum (XG), an exocellular heteropolysaccharide that is produced by the bacterium, *Xanthomonas campestris*. The conformation of xanthan gum in solution depends on the salt concentration and temperature. At low salt concentrations and high temperatures, the XG has a disordered form with a single-stranded structure [111–115]. The goal of this study was to develop a standardized protocol for creating a cheap synthetic biofluid for CF sputum that is rheologically consistent at both the bulk and the microscopic lengthscales.

Table 4.1: The ingredients of ASM. Adapted from Sriramulu [1].

Ingredients of ASM	
porcin mucin	5 g
fish sperm DNA	4 g
casamino acid	5 g
NaCl	5 g
KCl	2.2 g
Tris	15 ml (1 M)
DTPA	15 ml (1 mM)
egg yolk emulsion	5 ml
DI water	1 l

4.3 Experimental Methods and Materials

ASM +XG. Solutions of ASM were made by following Sriramulu et al. [1], which is reproduced in Table 4.1. All of the ingredients except egg yolk emulsion were dissolved in DI water and autoclaved for 30 minutes. After the solution cooled to room temperature, the egg yolk emulsion was added. Xanthan gum (T622, CP Kelco) in powdered form was added into ASM with concentrations of 0.1%, 0.2%, 0.3%, 0.4%, 0.5.% and 1.0%. These solutions were mixed thoroughly until the powder was dissolved.

Bulk rheology. We performed the bulk rheological measurements by using a standard rotational rheometer (DHR-3, TA Instruments) with a 2°, 40 mm stainless steel cone-and-plate geometry. We completed dynamic oscillatory strain sweeps at a frequency of $\omega_0 = 0.16$ rad/s for strains of $\gamma \in [10^{-4}, 0.5]$. The linear viscoelastic region was found to be below 10% deformation ($\gamma < 1$), and all subsequent fre-

quency sweeps were completed at a strain of $\gamma_0 = 0.01$. The frequency-dependent elastic modulus, G', and viscous modulus, G'', were found by performing an oscillatory shear sweep with frequencies of $\omega \in [0.01, 50]$ rad/s. Finally, the shear viscosity was found by completing steady-shear flow sweeps with shear rates of $\dot{\gamma} \in [0.01, 100]$ 1/s.

Microrheology. The microscopic rheological experiments were conducted by suspending one-micron particles of polystyrene in the medium. These particles are surface modified with carboxylate groups, and they are labeled with yellow/green fluorescence (F8823, Thermo Fisher). The medium was loaded into a micro-channel slide (Sticky Slide Luer, Ibidi) with both ends sealed. The Brownian motion of the fluorescent microparticles was imaged with a $40\times/0.6$ NA objective using an inverted microscope (Eclipse Ti-S, Nikon). The transient positions of approximately 50 in-frame particles were captured for a total of 5,000 frames at 31 frames per second with a CCD camera (Guppy Pro 125B, Allied Vision).

The MSD is calculated from the recorded frame using the method introduced previously and the modulus is calculated using the GSER of Eq. (4.31). The errors associated with the experiments are characterized by the method proposed by Savin [84]. There are two types of errors, static error and dynamic error. The static error rises from the experimental system such as vibration of the setup. The dynamic error arises from the finite acquisition time of the image. The position that is acquired at a certain time includes the history of successive positions of the

particles during this time interval that the shutter of the camera is open. Thus, the acquired position in each frame is the averaged positions over the shutter time. We characterized the static error in the typical way by fixing particles in an agarose gel and measuring the subsequent MSD. The dynamic error was minimized by choosing a smaller shutter time, while ensuring that the particles were visible.

4.4 Results and Discussion

The rheological properties of ASM+XG are tailored by using different concentrations of XG, and they are compared with the properties of CF sputum at the macroscopic lengthscale. The microscopic rheology focuses on the change in MSD and on the dependence of the relaxation time, the cage size, and the diffusive exponent on XG concentrations. A compilation of the macroscopic and microscopic rheological data can be found in Table 4.2.

4.4.1 Macroscopic Rheology

The macroscopic rheology of solutions of ASM and XG with different concentrations of XG were studied using a commercial rotational rheometer. The dynamic oscillatory strain-sweep (Fig. 4.6(a)) and frequency-sweep (Fig. 4.6(b)) tests showed that the ASM+XG mixtures became more elastically dominated with an increase in concentration of XG. The crossover frequency decreased with increasing concentration of XG from 0.1% to 0.4%. For 0.5% to 1.0%, the elastic modulus

dominated over all frequencies. The steady-shear tests showed that ASM+XG mixtures were shear thinning, as expected for many polymer solutions.

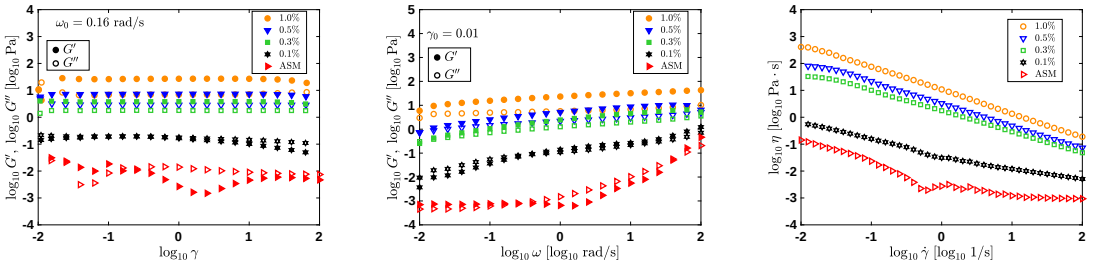

(a) Strain sweep. (b) Frequency sweep. (c) Flow sweep.

Figure 4.6: Rheology of ASM+XG for different concentrations of XG, $C_{\mathrm{XG}} \in \{0.1, 0.3, 0.5, 1.0\}\%$. (a) The strain-dependent elastic modulus (G', closed symbols) and viscous modulus (G'', open symbols). Strain sweeps were completed at a frequency $\omega_0 = 0.16\,\mathrm{rad/s}$. (b) The frequency-dependent elastic modulus (G', closed symbols) and viscous modulus (G'', open symbols). Frequency sweeps were completed at a strain of $\gamma_0 = 0.01$. (c) The apparent shear viscosities as a function of shear rate.

A comparison with data of CF sputum from Dawson et al. [2] in Fig. 4.7 has shown that the enhancement of ASM by the addition of XG at a concentration of 0.5% created a synthetic biofluid with rheological properties that agreed well with the rheological properties of CF sputum.Fig. 4.7 also shows plots of elastic modulus, the viscous modulus, and the viscosity of pure ASM, which were approximately two orders of magnitude smaller than the values of CF sputum in all three sweeps.

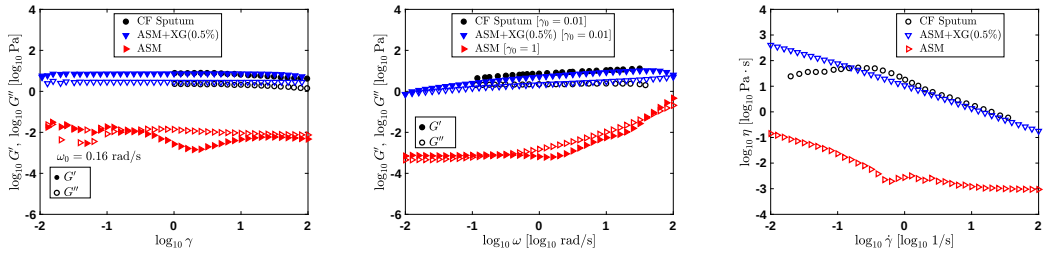

(a) Strain sweep. (b) Frequency sweep. (c) Flow sweep.

Figure 4.7: Comparison of rheological properties of ASM and ASM+XG(0.5%) to CF sputum from Dawon et al. (a) The strain-dependent elastic modulus (G', closed symbols) and viscous modulus (G'', open symbols). Strain sweeps were completed at a frequency $\omega_0 = 1\,\text{rad/s}$. (b) The frequency-dependent elastic modulus (G', closed symbols) and viscous modulus (G'', open symbols). Frequency sweeps were completed at a strain of $\gamma_0 = 0.01$ for CF sputum and ASM+XG and at a strain of $\gamma_0 = 1.0$ for ASM. (c) The apparent shear viscosities as a function of shear rate.

4.4.2 Microscopic Rheology

The microscopic rheological results show that particles that are suspended in ASM have dramatically different behavior depending on the concentration of XG (Fig. 4.8). The random trajectory of particles in ASM with no XG demonstrated a purely diffusive motion (Fig. 4.8(a)), which is indicative of a viscous, inelastic material. The MSD of purely diffusive motion scales as t^1, as exemplified in Fig. 4.9. The viscosity of ASM that was obtained by using the Stokes-Einstein relation was found to be 1.6×10^{-3} Pa·s. Although ASM consists of some macromolecules (porcine mucin, fish DNA, etc. [1]), the concentrations of these materials are too low to exhibit any elastic contributions. When XG was added to ASM, the thermal motions of the particles were altered. As shown in Figs. 4.8(b)-(c), particles that are diffusing in samples of ASM with the addition of 0.1% and 0.2% of XG

displayed two regions of dynamics. At short times the particles were constrained inside an elastic "cage", where a blob of trajectories can be seen. At long times the particles "hopped" from one elastic cage into another elastic cage, which can be seen in the trajectories as "blobs" that a re connected to each other. As the concentration of XG in ASM was increased, the size of the blobs became smaller in size and more dense in trajectories, and the paths that connect the blobs became shorter. As shown in Fig. 4.8(d), in a concentration of 1.0%, the particles were not able to diffuse, and they became trapped in a single environment.

Particles that are suspended in a more concentrated mixture of XG in ASM needed to expend more energy to escape the cages. The hopping behavior can also be seen in the plots of MSD versus time (Fig. 4.10(a)-(b)). At short times the diffusive exponent was less than one, when the particles were constrained inside the elastic cage, and they exhibited subdiffusive motion. At long times when the particles escaped their current cage and moved to their next cage, their overall motion again became random, resulting in an overall diffusive motion. The intersection of the subdiffusive region and the diffusive region indicated a characteristic relaxation time, t_r, of the polymer and a characteristic cage size, ℓ_c. As shown in Fig. 4.10 and plotted explicitly in Fig. 4.11, as the concentration of XG (C_{XG}) was increased, the relaxation time increased, scaling as $C_{\mathrm{XG}}^{1.40}$, and the cage decreased, scaling as $C_{\mathrm{XG}}^{-2.07}$.

When the concentration of XG was increased above 0.4% to 0.5%, the particles ap-

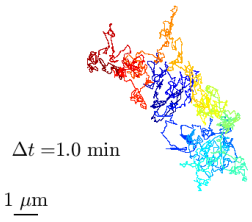

(a) ASM.

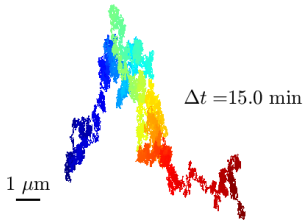

(b) ASM+XG(0.1%).

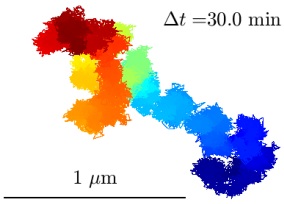

(c) ASM+XG(0.2%).

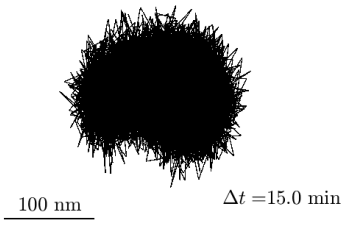

(d) ASM+XG(1.0%).

Figure 4.8: Trajectories of a single 1-μm particle. (a) In ASM, the particle is diffusive, traveling over 10 μm in 1.0 min. (b) In ASM+XG(0.1%), the particle is subdiffusive at short times, but the particle is diffusive at long times, traveling over 10 μm in 15.0 min. (c) In ASM+XG(0.2%), again, the particle is subdiffusive at short times, and the particle is diffusve at long times, traveling over 1 μm in 30.0 min. (d) In ASM+XG(1.0%), the particle is no longer diffusive, as the particle only samples its local environment of $\sim$ 200 nm in 15.0 min.

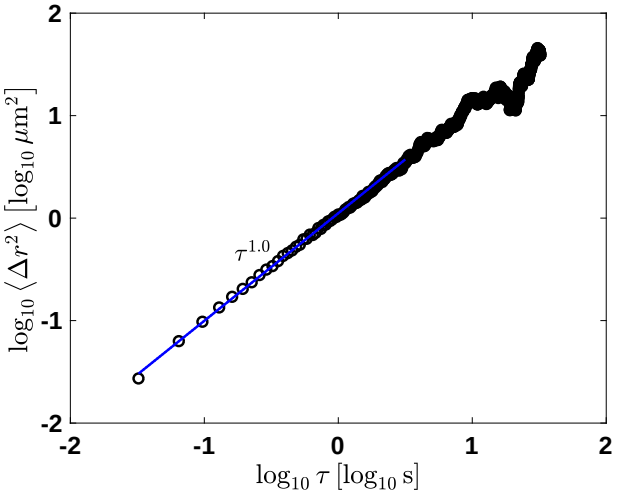

Figure 4.9: MSD of particles that were suspended in ASM. The MSD scales as t^1, and the viscosity was measured to be 1.6×10^{-3} Pa·s.

peared to become permanently constrained inside the elastic cage, and the resulting diffusive exponent became approximately zero. This general trend in constrained motion as a function of concentration of XG can be seen in Fig. 4.11(c), where the diffusive exponent decreased with an increase of the concentration of XG. The transition of the motion of the particles from diffusing in a viscous fluid to being constrained in an elastic gel can be seen in Fig. 4.12. The diffusive exponent changes from 1 to 0 as the concentration of XG was increased to 0.5%.

From the same plots of MSD (Fig. 4.10), the elastic and viscous moduli were obtained as a function of frequency by using the GSER. These values are compared with the bulk moduli that were obtained from standard rotational rheometry in Fig 4.13. The complex modulus is shown for samples of concentration of XG of 0.5% and 1.0%, as the microscopic rheological data did not provide a measurable

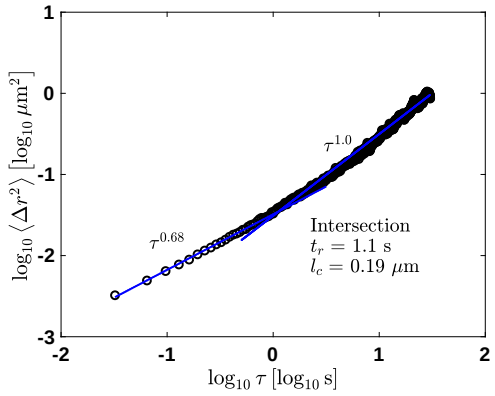

(a) ASM+XG(0.1%).

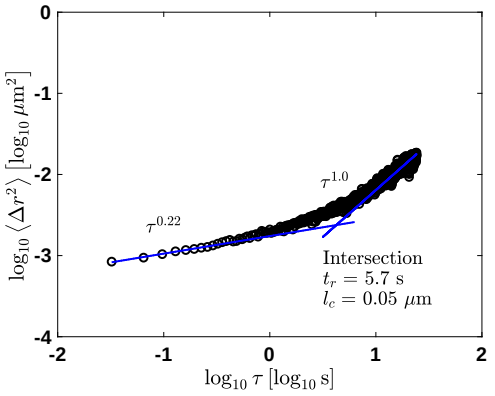

(b) ASM+XG(0.3%).

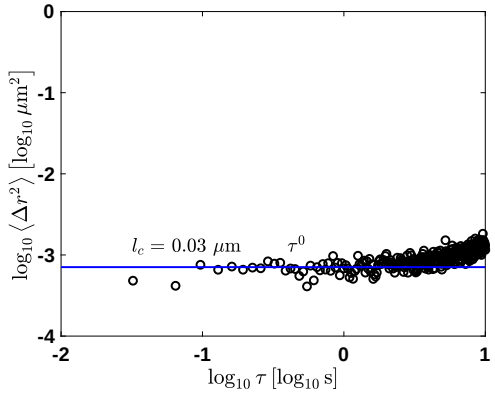

(c) ASM+XG(0.5%).

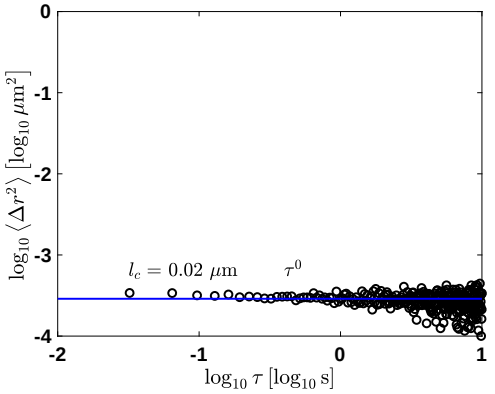

(d) ASM+XG(1.0%).

Figure 4.10: MSD of particles that were suspended in ASM at varying concentrations of XG, $C_{\text{XG}} \in \{0.1, 0.3, 0.5, 1.0\}$%. (a) The intersection of subdiffusion and diffusion is at $(t_r, \ell_c) = (1.1\text{ s}, 0.19\ \mu\text{m})$. (b) The intersection of subdiffusion and diffusion is at $(t_r, \ell_c) = (5.7\text{ s}, 0.05\ \mu\text{m})$. (c) The MSD scales as τ^0, and $\ell_c = 0.03\ \mu$m. (d) The MSD scales as τ^0, and $\ell_c = 0.02\ \mu$m. With an increase of the concentration of XG, the motion of the particles become more subdiffusive, the relaxation time becomes longer, and the cage size becomes smaller. Ultimately, the particles are bounded inside an elastic cage at the concentrations of 0.5% and 1.0%, where the motion implies that the media was a viscoelastic solid.

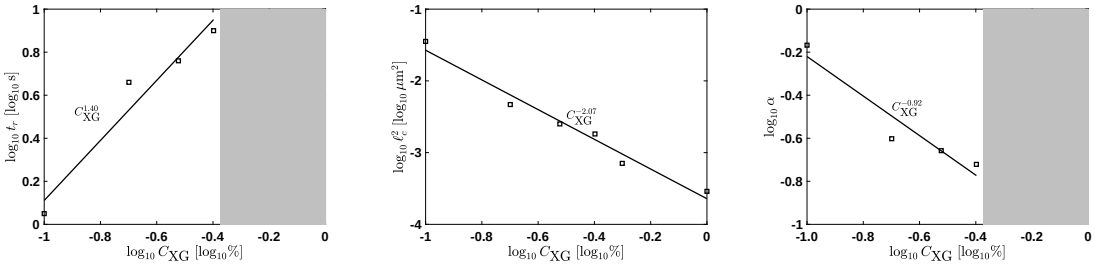

(a) Relaxation time. (b) Cage size. (c) Diffusive exponent.

Figure 4.11: Diffusive properties as a function of the concentration of XG. (a) The relaxation time t_r versus concentration. The relaxation time increases with the concentration of XG with the scaling of $C_{\mathrm{XG}}^{1.4}$. The gray area shows that, at a concentration of 0.5% and higher, the particles are permanently captured in the elastic cage, and the relaxation time cannot be obtained. (b) The cage size ℓ_c versus concentration. The cage size decreases with the concentration of XG with the scaling of $C_{\mathrm{XG}}^{-2.07}$. (c) The diffusive exponent α versus concentration. With an increase of the concentration of XG (from 0.1% to 0.4%), the motion of the particles become more subdiffusive, and the diffusive exponent, α, scales as $C_{\mathrm{XG}}^{-0.92}$. The gray area shows that, at a concentration of 0.5% and higher, the diffusive exponent is zero, and the ASM+XG mixtures are purely elastic.

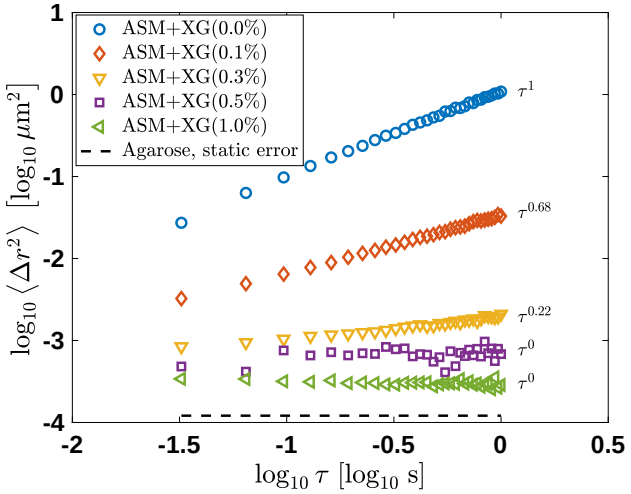

Figure 4.12: MSD of particles that were suspended in ASM with different concentrations of XG. The slope of MSD shows that the ASM is purely viscous $\left(\mathrm{MSD} \sim \tau^1\right)$. With an increase in concentration of XG, the mixture becomes elastically dominated, and eventually, it becomes a pure solid $\left(\mathrm{MSD} \sim \tau^0\right)$. The agarose that was used to characterize the static error of the experimental system is shown for comparison of the cage size.

viscous modulus. In Fig 4.13(a)-(b), the crossover frequency (ω_c, the reciprocal of the characteristic "relaxation" time) obtained from the microscopic rheological measurements generally decreased as the concentration of XG increased, which is in agreement with the macroscopic rheological measurements. However, the moduli that were obtained microscopically at high frequencies (>10 rad/s) were consistently about one order of magnitude smaller than the moduli that were obtained macroscopically, which is consistent with the results from Dawson *et al.* in Fig. 4.5. Thus, the solutions of XG appear to have a hierarchy of structures that is similar to CF sputum.

These results can be described by considering that the particles could have been constrained inside a small first-order structure that was itself contained inside a larger second-order structure. Since the size of the particle may have been small when compared wit the second- or higher-order structures, the rheological properties at higher order would not have been probed. The macroscopic rheological techniques, however, averaged the properties of the material at lengthscale that are greater than a millimeter. The viscosities that were obtained in this diffusive region at long times were compared with the zero-shear viscosities that were obtained from standard rotational rheometry. Figure 4.14 shows that the builk viscosities were again consistently about an order of magnitude larger than the viscosities that were obtained from the microscopic rheological technique. However, the scale of the viscosity with concentration was close between the macroscopic and microscopic methods, which is consistent with the theoretical scaling prediction from

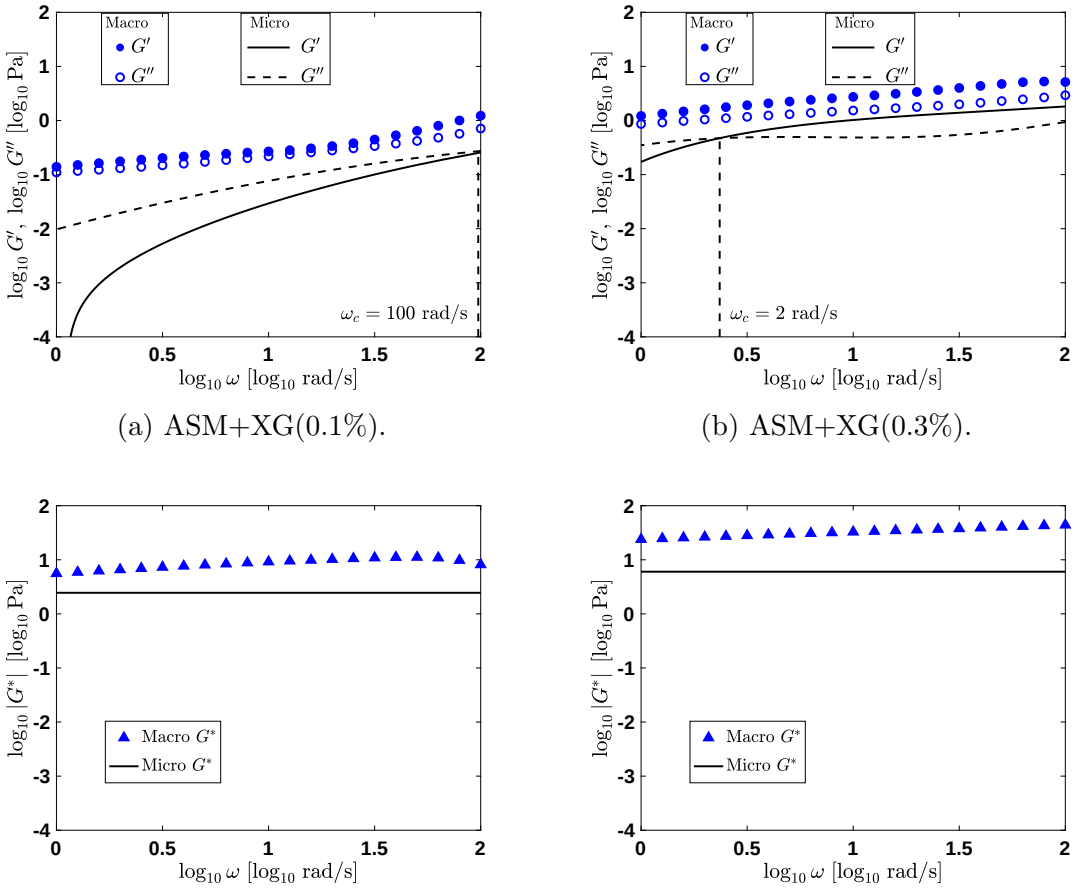

(a) ASM+XG(0.1%).

(b) ASM+XG(0.3%).

(c) ASM+XG(0.5%).

(d) ASM+XG(1.0%).

Figure 4.13: Comparison between microscopic rheology and macroscopic rheology for varying concentrations of XG. (a), (b) Elastic modulus G' and viscous modulus G'' for concentrations of XG of 0.1% and 0.3%. Lines are used for microscopic rheology, and spheres are used for macroscopic rheology. Solid lines or filled symbols are used for G' and dashed lines or open symbols are used for G''. (c), (d) Comparison of $|G^*|$ of concentrations of XG of 0.5% and 1.0%. Lines are used for microscopic rheology and triangular symbols are used for macroscopic rheology.

reptation theory ($\eta_0 \sim C_{\mathrm{XG}}^{3.75}$) [116].

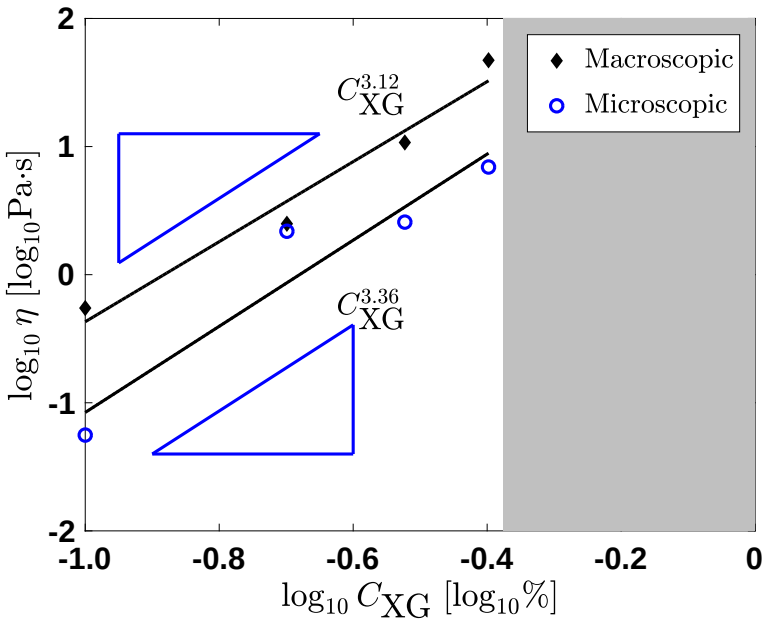

Figure 4.14: Viscosity of ASM as a function of different concentrations of XG, $C_{\mathrm{XG}} \in \{0.1, 0.2, 0.3, 0.4\}$%. The gray area shows the concentration of XG that cannot be used to calculate the viscosity because the particles are permanently captured in the elastic cage. The microscopic viscosities were obtained from the long-time diffusive region. The macroscopic viscosity was found using the zero-shear viscosity.

4.5 Conclusion

The rate of diffusion of 1-μm particles in ASM was found to be only 0.63 times the diffusion rate in water. The low concentration of polymers in ASM had trivial influence on the elastic properties at a microscopic lengthscale. The addition of XG, however, created weakly-associated elastic cages that bounded the probe particles. The ionic environment of the ASM solution causes XG to conform to a fivefold helix, and the intermolecular associations cause the formation of networks, or elastic

"cages" of XG. At lower concentrations ($C_{XG} \leq 0.4\%$), the particles were observed to escape the cages at long times. At higher concentrations ($C_{XG} \geq 0.5\%$), the resulting material appeared gel-like, and the particles were observed to be restrained inside the cages. This study provides preliminary microrheological data by using less costly materials and directs future studies, for instance, on the dependence of particle size and surface functionality. To study the discrepancy between macroscopic and microscopic rheology of ASM+XG, larger particles should be used.

Table 4.2: Macroscopic and microscopic data of ASM, ASM+XG, and CF sputum [2].

ASM+XG	Macroscopic Rheology ($\omega = 1$rad/s, $\gamma_0 = 0.01$)				Microscopic Rheology		
[% XG]	G' [Pa]	G'' Pa]	ω_c [rad/s]	η_0 [Pa·s]	α [-]	t_r [s]	l_c [μm]
0%	6.5×10^{-4}	1.5×10^{-3}	—	—	1	∞	—
0.1%	0.14	0.11	0.62	0.55	0.68	1.1	0.19
0.2%	0.39	0.40	2.6	2.50	0.25	4.6	0.068
0.3%	1.2	0.86	10.8	10.76	0.22	5.8	0.050
0.4%	3.2	1.6	48.9	47.18	0.19	7.9	0.043
0.5%	5.1	2.2	—	78.45	0	—	0.027
1.0%	23.2	2.2	—	401.50	0	—	0.017
CF	7.3	2.2	—	50.98	—	—	—

Chapter 5

Suppressed Coarsening of Particles in Yield-Stress Fluids

So far we have discussed the suspensions of particles in Newtonian fluids (Chapters 2 and 3) and microrheological study of non-Newtonian fluids (Chapter 4). We have shown that the rotational and translational of magnetic microdisks under a rotating magnetic field cannot be decoupled if the microdisks are suspended in a Newtonian fluid. If the microdisks are suspended in a non-Newtonian fluid, specifically a fluid with yield stress, we have shown that we are able to suppress

the translational motion while allowing the rotational motion, which is the main topic of this chapter. Moreover, the yield stress at a microscopic lengthscale of the fluid is characterized by the microrheological technique discussed in Chapter 4.

5.1 Motivation and Background

Inkjet printing is a deposition technique used for fabrication of a variety of novel materials via using functionalized fluids, such as solar cells that are printed with poly(methyl methacrylate) polypyridyl ruthenium (II) copolymer and C_{60} fullerene with heptyl viologen derivatives [119], DNA microarrays [120], active proteins [121], tissue structures, and magnetic materials [122, 123]. The inkjet printing can be combined with an external magnetic field to create construct complex configurations inside the droplets and so control the properties. For instance, anisotropy can be achieved by aligning MOPs, and the configurations can be fixed by polymerization of the droplets. One-dimensional and two-dimensional anisotropy have been obtained by using rod-like MOPs [124] and disk-like MOPs [3, 19, 29] respectively.

The external magnetic field can induce magnetic particles which subsequently will attract neighbor particles to create column-like or sheet-like structures [29,125] (see Fig. 5.1). Although the chaining can be exploited in magnetorheological (MR) fluids for magnetically activated devices [126], such coarsening of the particles can

be unfavorable in areas like high-frequency applicationsm as it increases the eddy-current loss in the material. Thus, to obtain a composite with a high concentration of aligned magnetic microdisks and a homogeneous distribution, a race occurs among three events: (1) the alignment of the magnetic particle, (2) the coarsening of the particles through particle-particle interactions, (3) the freezing of the particles into place through phase transition (e.g., polymerizing the suspending medium). The ideal suspending medium for processing these composites would therefore be a fluid with a high translational viscosity that restricts chaining and with a low rotational viscosity that allows alignment.

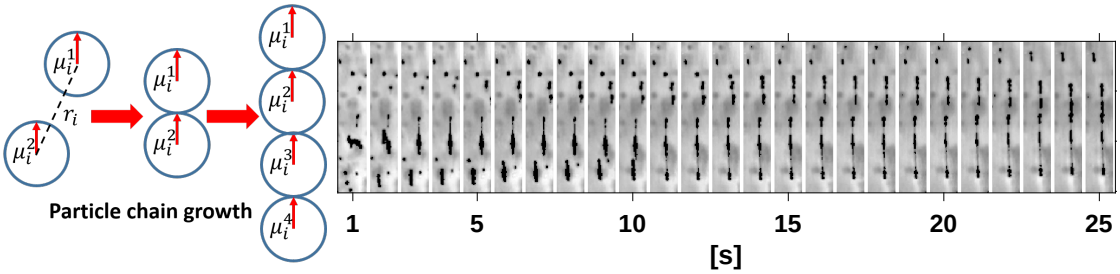

(a) Cartoon of spheres chaining.

(b) Time sequence of disk chaining.

Figure 5.1: (a) Cartoon showing coarsening of chains of spherical particles in a constant magnetic field directed up relative to the page. (b) Experimental sequence of NiFe disks (5 μm diameter, 0.05 vol%) chaining in a 10-mT constant magnetic field directed up relative to the page.

To prevent the migration of particles, nonlinear fluids, especially fluids that exhibit a yield stress, have been successfully introduced. Associated gel networks of gum solutions (e.g., xanthan, gellan) have been shown to prevent sedimentation in particle suspensions [127, 128]. Rich et al. postulated [129] and confirmed [130] that such materials could arrest magnetic particles. Since these fluids have relatively

quick reformation time of their yield stress, they make ideal candidates for allowing rotational alignment while preventing translational chaining in a fluid that can still be successfully ejected from an inkjet printhead.

In our previous work, we have shown that two-dimensional sheets of particles are formed under a rotating magnetic field when microdisks are suspended in a linear fluid. In this study, microdisks were suspended in solutions of gellan gum to utilize its nonlinear rheological properties. The concentration of the gellan gum was tuned to obtain a yield stress that was strong enough to prevent the particles from migrating (or sedimenting), but the alignment of particles was still obtained. We present a theoretical comparison of the characteristic timescales that are associated with the rotational and translational motions in a linear fluid, validating the necessity for such an elaborate system, and an experimental comparison between the yield stress of a suspending fluid and the stresses that are caused by rotational and translational motions, as a proof of concept for future development. We also provide a detailed characterization of our suspending media to exemplify the ability to tune the value of yield stress for this concept.

5.2 Theoretical Scalings

For particles with induced dipoles, most of the available work in the literature focused on rods that have a director or orientation vector, $\mathbf{p}$, that is in the direction of the axis of extension of the particle (the axis of rotation or the axis of symmetry).

When researchers have made progress on the dynamics that are associated with disks, they have almost always been interested in oblate spheroids that have a permanent dipole that is directed in the axis of symmetry. In this study, we study the oblate spheroids that have an induced dipole as introduced before. The influence of rotational fields on distribution of oblate spheroids with induced dipoles has been rarely discussed in the literature to date.

5.2.1 Equilibrium Configuration in A Linear Fluid

Our preliminary efforts to study suspensions of disks with induced dipoles under rotating magnetic fields have provided insight into the creation of layered structures, as shown in Fig. 5.2(b). The dynamics of sheet formation and sheet coarsening are actively being investigated, but we have recently developed a simple geometric argument to discuss the long-time equilibrium state of a hexagonal packing that will arise. These sheets are found to form layers that are single-particle thick, which is a direct result of the magnetization that induces the magnetic dipole. Since the dipole is dynamic in its direction, two sheets that are stacked in close proximity with their surface normals pointing parallel (as is forced by the rotating magnetic field) will initially repel each other as their overall magnetization creates a situation where the north and south poles of the sheets are in close proximity.

Therefore, if we assume that a single layer of spheres will pack in an ideal hexagonal configuration, we can estimate the separation distance that exists between two layers by simply using the overall volume fraction of the particles and some geome-

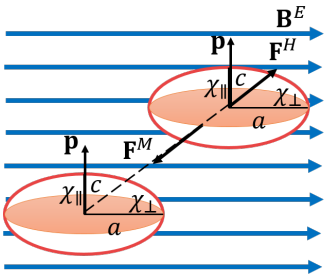

(a) Particle-particle geometry.

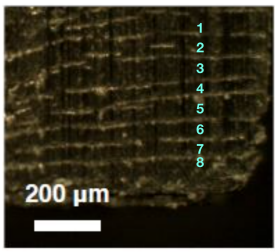

(b) Sheets formation.

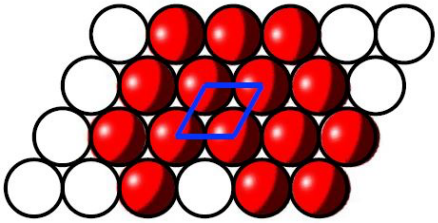

(c) Hexagonal sheet.

Figure 5.2: Geometric arrangements of chaining events. (a) Two oblate spheroids with induced dipoles. (b) Sheets formed by a rotating magnetic field taken from experiments. The magnetic field rotates in the plane that is perpendicular to the plane of view. The dimension of the particle is $a = 2.5\,\mu$m and $c = 75\,$nm, and the volume fraction is $\phi = 0.001$. Eight sheets are identified with a sheet spacing of $d_{\text{exp}} = 80 \pm 37\,\mu$m. (c) Ideal hexagonal sheet formation under a rotating magnetic field. A unit cell is chosen in the blue rhombus.

try. For a hexagonal lattice (Fig. 5.2(c)), if one cuts a unit cell (parallelogram-type prism) from the lattice that connects the centers of four neighbor spheroids, then one full spheroid will exist inside the unit cell with a volume, V_c, of

$$V_c = 2\sqrt{3}a^2 d, \tag{5.1}$$

where d is the separation distance of the layers. By defining the volume fraction to be $\phi = \frac{V}{V_c}$, where volume of an oblate spheroid is $V = \frac{4\pi a^2 c}{3}$, the spacing can be predicted to be

$$d = \frac{2\pi c}{3\sqrt{3}\phi}. \tag{5.2}$$

A quick calculation of the experiment in Fig. 5.2(b) shows that, for $a = 2.5\ \mu$m, $c = 75$ nm, and $\phi = 0.001$, the sheet spacing should be approximately $d = 90\ \mu$m.

The actual measured value is $d_{\text{exp}} = 80 \pm 37$ μm, which confirms the geometry scaling. Microtome slices in the (x, y)-plane, which is perpendicular to the axis of rotation of the magnetic field, show that the assumption of hexagonal packing was not fulfilled. Thus, a nonideal random packing exists, which will reduce the number of particles that can exist in a sheet, increase the total number of sheets that are present, and decrease the sheet-to-sheet spacing. This simple geometric scaling provides an excellent estimate if bulk composites are attempting to be made with well-controlled sheet spacing. This configuration shows the potential for control of anisotropic diffusivities in metamaterials with controlled diffusivity ratios.

5.2.2 Timescales of Rotation and Translation in A Linear Suspending Liquid

We have seen the two characteristic timescales associated with the rotational and translational motions in Chapter 2 and 3. Let's reaffirm them here

$$t_R = \frac{32\eta a^3 \mu_0}{3V\chi_\perp^E B^2 (1-\alpha)}, \text{ and} \tag{5.3a}$$

$$t_T = \frac{64\pi\mu_0 r_0^5 \eta a}{3\left[V\chi_\perp^E B\right]^2}. \tag{5.3b}$$

The ratio, β, between these two timescales dictates which motion dominates,

$$\beta = \frac{t_R}{t_T} = \frac{2}{3}\frac{a^4 c}{r_0^5}\frac{\chi_\perp^E}{1-\alpha}. \tag{5.4}$$

If $\beta \gg 1$, then the timescale for rotation is much greater than the timescale for translation, and the particle will chain before orienting. In contrast, if $\beta \ll 1$, then the timescale for rotation is much smaller than the timescale for translation, and the particle will orient long before chaining occurs. The time ratio can be treated as a product of the volume fraction, $\phi \sim \frac{a^2 c}{r_0^3}$, the planar area fraction, $\psi \sim \frac{a^2}{r_0^2}$, and the magnetic property of the particle, $\frac{\chi_\perp^E}{1-\alpha}$. Once the particle shape, size, material, and volume fraction are chosen for a given experiment, the timescales for orientation and translation are no longer independent. If an even distribution of the center of mass of the aligned particles is sought, β must be kept low. Yet, β grows in magnitude as the volume fraction, ϕ, the planar area fraction, ψ, or the perpendicular susceptibility, $\chi_\perp^E$, grow in magnitude, and β also grows as the susceptibility ratio, α, approaches unity.

5.2.3 Stress Scales of Motion in A Nonlinear Suspending Fluid

By sparsely distributing the particles in a linear fluid, the translational motion can be slowed; however, translation and orientation cannot be decoupled, and the translational motion can lead to significant chaining in a densely distributed fluid. To suppress the translational motion, a nonlinear fluid can be introduced in an attempt to arrest the particles. If we return to the idea that an ideal suspending medium would would have a high translational viscosity that restricts chaining an a low rotational viscosity that allows alignment, then a fluid that exhibits a yield stress with a fast reformation time would be a prime candidate. Some materials

require an applied force before flow is achieved (e.g., ketchup, toothpaste). The associated stress of this force is called a yield stress. Not all non-Newtonian fluids exhibit a yield stress, but they are common in hydrocolloids, crosslinked polymers, gels, and colloidal dispersions, where a significant microstructure can withstand an external force.

The magnitude of the yield stress, τ_y, needs to be carefully adjusted to allow rotational motion while suppressing translational motion. Therefore, we compare the yield stress with the magnetic force and torque to obtain a proper parametric scaling that permits the alignment while preventing the migration. Similar to the dimensionless parameter, Y_g, that is used in the work of Beris *et al.*, which is the ratio between the yield stress and the gravitational stress, we use two dimensionless parameters, Y_T and Y_R, that are the ratio between the yield stress and the stresses that are created by the magnetic force and the magnetic force, respectively. A quick derivation of the scaling is shown below.

The magnitude of the magnetic forece, F^M, and the magnetic torque, T^M, are found in previous chapters, and reaffirmed here

$$F^M \sim \frac{\left[V\chi_\perp^E B\right]^2}{\mu_0 r_0^4}, \text{ and} \tag{5.5a}$$

$$T^M \sim \frac{V\chi_\perp^E B^2}{\mu_0}. \tag{5.5b}$$

The magnitude of magnetic force represent an upper bound on the pairwise in-

teractions for a given separation distance as the particles are fully aligned and in-plane. Similarly, the magnitude of the traction on the surface of the particle that is caused by the yield stress is given by

$$F^Y \sim \tau_y a^2 \left(\frac{1-e^2}{e} \right) \tanh^{-1} e, \tag{5.6}$$

where e is the eccentricity of the microdisk, such that $[ea]^2 = a^2 - c^2$. The magnitude of the torque that is caused by the yield stress scales like

$$T^Y \sim \tau_y a^3. \tag{5.7}$$

Thus, the dimensionless parameters Y_T and Y_R can be found to scale like

$$Y_T = \frac{F^Y}{F^M} \sim \frac{r_0^4}{a^4} \frac{\mu_0}{\left[B\chi_\perp^E\right]^2} \tau_y, \text{ and} \tag{5.8a}$$

$$Y_R = \frac{T^Y}{T^M} \sim \frac{a}{c} \frac{\mu_0}{B^2 \chi_\perp^E} \tau_y, \tag{5.8b}$$

which will hold at leading order for most practical particles with aspect ratios, $\rho = \frac{c}{a} > 1 \times 10^{-2}$. In the case of $Y_T > 1$ and $Y_R < 1$, the particle alignment can be achieved, while the translation of particles is obstructed. An inequality can then be written that bounds the yield stress, setting the necessary property of suspending fluid, such that

$$k_T \frac{a^4}{r_0^4} \frac{\left[B\chi_\perp^E\right]^2}{\mu_0} < \tau_y < k_R \frac{c}{a} \frac{B^2 \chi_\perp^E}{\mu_0}, \tag{5.9}$$

where k_T and k_R are proportionality constants that are only dependent on geometry and susceptibility. The left side of this inequality can be considered τ_T, the maximum stress on the body that is associated with translation, and the right side of this inequality can be considered τ_R, the minimum stress on the body that is associated with rotation. This inequality can be immediately simplified to produce a criteria for the packing density of the material such that

$$k_T a^5 \chi_\perp^E < k_R c r_0^4. \tag{5.10}$$

This criteria is independent of the field strength, which again makes manipulating external variables of the process unavailable. If the type of particles are set for a specific experiment such that $\{a, c, \chi_\perp^E\}$ are known, then r_0 is set by this criteria. Thus, this criteria can be written in a form that sets a bound on the volume fraction $\left(\phi \sim \frac{a^2 c}{r_0^3}\right)$ that can be used in practice without experiencing chaining, where the maximum volume, $\widehat{\phi}$, assuming an even distribution, scales like

$$\widehat{\phi} \sim \rho \left[\frac{\rho}{\chi_\perp^E}\right]^{3/4}. \tag{5.11}$$

Finding the exact proportionality constant would require numerically solving for Y_R and Y_T; however, in practice, empirical fitting to experimental data for a specific system would still be necessary. Thus, this expression provides a general design heuristic for manufacturing as the volume fraction of the composite is increased.

5.3 Experimental Methods and Materials

Building on the insight that was developed from the theoretical scalings in the previous sections that allowed for the development of bounded regimes for relating particle volume fraction, yield stress, and field strength, we identified experimental strategies for magnetically aligning filler particles while preventing chaining through the use of a fluid with a yield stress. We hypothesized that, at sufficient magnetic fields, altering the concentration of the constituents of the fluid and thus the strength of the yield stress would allow adjustment of the cages of stress so that the particles would be able to align without migrations.

5.3.1 Gellan Gum

In this study, we used CG-HA gellan gum from CP Kelco for our suspending medium. CG-HA is a pharmaceutical-grade, high acyl gellan gum that forms soft, elastic, non-brittle gels. Solutions at certain concentrations of gellan gum present as Bingham plastics (i.e., non-Newtonian, shear thinning fluid with a yield stress), which have the ability to indefinitely suspend particles, depending on the yield stress. Polymer systems that contain gellan gum are capable of exhibiting a given yield stress at much lower shear viscosities than most hydrocolloids, allowing the system to suspend materials of dissimilar density while maintaining manageable flow behavior.

Gellan gum is an industrially relevant biopolymer that is utilized in food, personal-

care, and pharmaceutical industries for its ability to gel, texturize, stabilize, form films and suspensions, and act as a structuring agent. Gellan gum has also been utilized in bioink for bioprinting of living cells, including tissue scaffolds, as it allows for filament deposition with a larger operating range, less fine-tuning of parameters, and reduced optimization of printing temperatures and settings.

To reduce the time-dependent, thermoreversible development of aggregates in the solutions of gellan gum, all samples were made one day in advance, stored in the refrigerator at 4℃overnight, brought to room temperature, and mixed in a centrifuge at 1000 rpm prior to being used. All concentrations are presented as a percent, where the percent is the weight of gellan gum per volume solute (w/v%).

5.3.2 Bulk Rheology

In an effort to connect the microscopic properties being probed by the particles to the macroscopic properties, we investigated the concentration dependence of the bulk yield stress for gellan gum. A protocol for measuring yield stress was developed using a standard rotational rheometer (TA Instruments DHR-3) with a 60 mm, 1° cone and plate to complete a stress sweep (0.001 to 1 Pa) under steady shear. The sample holding time was set to 30 s with an equilibrium time of 5 s and measurement time of 60 s.

A weak yield stress was determined on the order of 1×10^{-2} Pa. Figure 5.3(a) shows the results of the yield stress as a function of concentration of gellan gum

from $C_{\mathrm{GG}} = [0.001, 0.1]\%$ for $C_{\mathrm{NaCl}} = 1\%$. A monotonic relationship between the addition of gellan gum and an increase in yield stress is observed over this range of concentrations with good reproducibility for replicate concentrations. Variations in the reproducibility increase above $C_{\mathrm{GG}} = 0.065\%$, as the timescale of reformation after loading the sample increases beyond the limited time that is available to ensure that evaporation is not affecting the sample. Further, multiple batches of gellan gum were used throughout the study, and the sensitivity of the yield stress these concentration is quite pronounced, as seen in Fig. 5.3(a).

5.3.3 Microrheology

Polystyrene (PS) particles (SpherotechSphero$^{\mathrm{TM}}$, $d = 4.3\,\mu$m, $\rho = 1.22\pm0.02\,\mathrm{g/cm^3}$) with ferromagnetic inclusions were used in two different experiments to determine the concentration dependence of the microscopic yield stress of the solutions of gellan gum.

Suppresion of Gravitational Sedimentation. Longtime suspension of particles has been a consistent roadblock in maintaining a homogeneous distribution of the center of mass in suspensions of magnetic particles. We initially utilized the high density of the particles to determine the lowest concentration of gellan gum that allowed particles to stay indefinitely suspended within the bulk fluid, identifying a concentration such that the microscopic yield stress of the fluid was a greater than the gravitational stress. The experimental setup consisted of a Nikon D90 DLSR that was secured to a z-axis platform. A digital timer remote was used to capture

experimental photographs every hour for 24 hours. Experimental fluids were prepared by pipetting 1 mL of solution into a 1.5 mL centrifuge tube. A 2.5% bulk solution of 4.3 μ, PS particles with ferromagnetic inclusions was vortexed on the highest speed for 30 s to ensure a homogeneous concentration of particles throughout the bulk solution. Immediately after vortexing, 20 μL of the bulk particle solution was pipetted into the 1 mL aliquots in centrifuge tubes. Figure 5.3(b) shows the dispersed particles at $t = 0$ h, while Fig. 5.3(c) shows the dispersed particles at $t = 24$ h.

A concentration was deemed to have an inadequate yield stress if the particles completely settled to the bottom of the tube. Complete sedimentation of PS particles with magnetic inclusions occurred after 24 h for all concentrations below 0.02%. Concentrations above 0.025% were able to suspend particles indefinitely. This method served to determine lower concentration bounds for gravitational stress scalings. Calculating the stress that is exerted on the lower half of the particle by associated buoyancy force, τ_g, such that

$$\tau_g = \frac{2\Delta\rho g a}{3}, \tag{5.12}$$

the yield stress can be calculated via a simple stress balance, $\tau_y = \tau_g$, to be $\tau_y(C_{GG} = 0.025\%) > 3.1 \times 10^{-3}$ Pa, which is displayed in Fig. 5.3(a) for comparison.

Suppression of Magnetic Migration. To measure the microscopic yield stress of

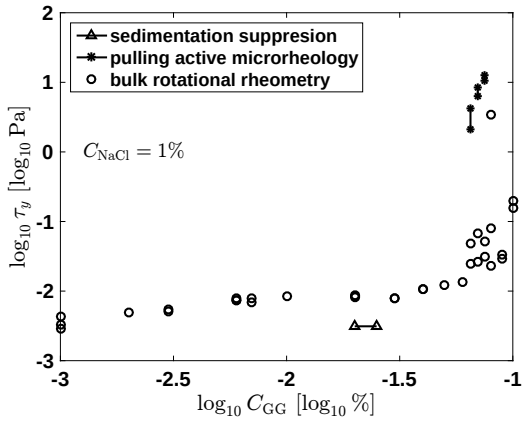

(a) Bulk and microscopic measurements of yield stress.

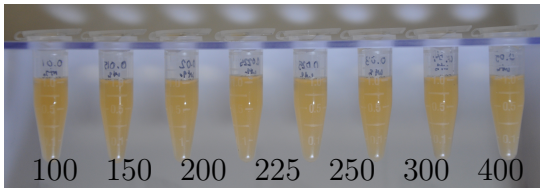

(b) Initial photograph, $t = 0\,\mathrm{hr}$.

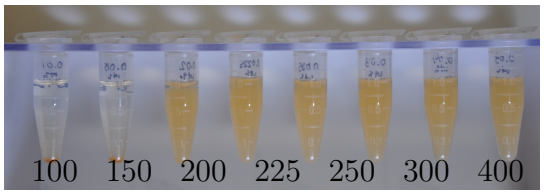

(c) Final photograph, $t = 24\,\mathrm{hr}$.

Figure 5.3: Yield stress as a function of concentration of gellan gum. (a) Bulk rheological results for concentration of gellan gum from 0.001 to 0.1% in 1% NaCl. The triangle ($\triangle$) indicates the value for the microscopic yield stress that was calculated from the sedimentation suppression. The asterisks ($*$) indicate the values of the microscopic yield stress that was obtained from pulling active microrheology. (b)-(c) Time-lapse sedimentation experiment. Polystyrene particles with magnetic inclusions ($d = 4.3\,\mu$m, $\rho = 1.22 \pm 0.02\,\mathrm{g/cm}^3$) were injected into various concentrations of gellan gum (CG-HA). From left to right, $C_{\mathrm{GG}} = \{0.0100, 0.0150, 0.0200, 0.0225, 0.0250, 0.0300, 0.0400, 0.0500\}$ % in $C_{\mathrm{NaCl}} = 1\%$ (note that concentrations in the photos are shown as weight per volume percent times 10^4). Values from the microscopic rheological results are included. (b) Suspensions immediately after they were vortexed for 30 seconds for particle suspension. (c) Complete sedimentation of polystyrene particles with magnetic inclusions occurs after 24 hours for all concentrations below 0.02%. Concentrations above 0.025% were able to suspend particles indefinitely.

the solutions of gellan gum above concentrations that can suppress sedimentation, we utilized a magnetic bead microrheometer (Fig. 5.4(a)), the so-called *magnetic tweezers* [90–92] that has been mentioned before. The magnetic tweezers used in this study is a single-pole magnetic tweezers which has a very fine tip. It is mounted on an independent stage so that it can externally apply a magnetic body force ($\mathbf{F}^M$) to control the motion of paramagnetic particles within viscoelastic fluids. The force that is exerted by the magnetic field is $\mathbf{F}^M = \nabla [\boldsymbol{\mu} \cdot \mathbf{B}]$. However, the field strength of the fine magnetic tip is very difficult to measure explicitly, with the gradient of the magnetic field near the tip being very sharp. A region of 155 μm $\times$ 155 μm that was centered 150 μm from the tip was chosen as the region of interest for this experiment. A force map is constructed by pulling the particles through a Newtonian fluid of known viscosity. Two different dilutions of corn syrup were prepared and measured on a rheometer. Suspensions of Spherotech particles were prepared with both dilutions, and the motion at relevant input voltages was captured via video. The trajectory of the particles in the fluid was used to calculate the body force that was experienced by a particle at a particular location. Trajectories in the region of interest were selected and used to calculate the average force in the region. From this force map, an estimate can be made for the force that is required to induce translation for each concentration gellan gum.

The electromagnetic was driven with a Kepco bipolar operational power supply/amplifier (BOP 20-10M), which was controlled using a RIGOL DG1022 func-

tion generator. An inverted microscope (Nikon Eclipse Ti-S) with transmitted light and either a 4× magnification or a 10× magnification (Fig. 5.4(a)) was used to track the motion of the particles in time throughout the experiment. By completing a simple force balance ($F^H = F^M$), the viscosity of the fluid can be measured from knowledge of the magnetic body force (input stress) and the tracking of the bead (output strain) [131].

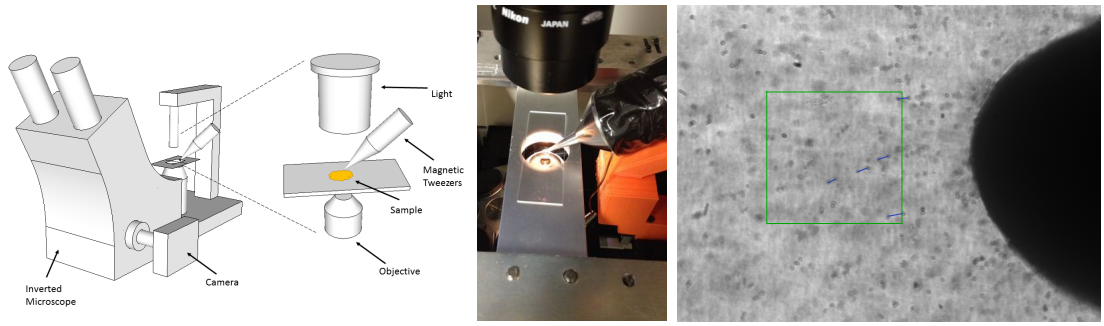

(a) Magnetic tweezers setup. (b) Apparatus. (c) Microscopic yield experiment.

Figure 5.4: (a) Horizontal slide containing the complex fluid that was seeded with magnetic particles is placed on an inverted transmission microscope (left), allowing precise control of the magnetic body force (right: closeup of magnetic tweezers). (b) A pulling magnetic-tweezer apparatus with sharpened soft-iron rods is positioned directly above an inverted microscope objective. (c) Microscopic image of tip of magnetic tweezers. The image is a composite of the initial and final state of the particles with nonrecoverable displacements that are marked in blue. The region of interest ($155\,\mu\text{m} \times 155\,\mu\text{m}$) for the tweezers is bounded in green.

For each experiment, approximately 100 μL of the solution was placed in a small well on the microscope stage. The fine tip of the electromagnet was brought into the field of view and lowered into the solution without contacting the bottom of the well. Using the function generator, a constant voltage was applied to the Kepco amplifier input, and the response of the particles in the field of view was captured

in a video. If more than three particles within the plane of focus and region of interest were determined to have moved more than 1.5× the particle diameter, then the voltage as determined to generate a field which results in a force at or above the yield stress. The results are shown in Tabel 5.1.

Table 5.1: Input voltage, calibrated yield force, and calculated yield stress for each concentration.

C_{GG} [%]	V [mV]	F^Y [pN]	τ_y [Pa]
0.065	200	120	4.2
0.070	400	250	8.4
0.075	600	370	12.7
0.080	> 800	–	–

At low voltage, particles moved slightly in the weak hydrogel, but they recovered fully once the power was removed from the magnet. As the power was increased, a small number of particles very near the tip eventually began to overcome the yield stress and translate toward the magnet. As the power was increased further, this translation occurred at greater distances until the motion occurred within the calibrated region. The minimum force that was required to induce displacement of the particles that did not fully recover once the magnetic field was removed was interpreted as the local yield stress of the fluid.

The particles experiencing critical voltage in the lowest concentration moved short distances along predictable trajectories. More erratic motion was observed as the yield stress exceeded in the other trials. In the 0.07% solution, some particles broke free and displayed characteristic flow behavior, while others remained bound

but followed a path not perfectly aligned with the magnetic field. The 0.075% solution required the strongest body force to surpass the yield stress. At that intensity, nearly all particles that showed non-recoverable displacement exhibited rapid movement to the magnetic tip. With the current setup, the power supply could nod deliver enough current to the magnet to induce translation in the 0.08% solution. Further support that this body force is on the order of the yield stress is that the particles in each concentration undergo flow behavior at voltages above the critical voltage. This behavior is particularly evident in the 0.070% and 0.075% solutions.

5.3.4 Microdisk Alignment

Directed alignment experiments in a rotating magnetic field were conducted using ferromagnetic microdisks to provide a proof of concept that a fluid with yield stress can allow rotation while preventing translation. These experiments utilized a three-axis electromagnetic coil system that has been discussed in detail in Chapter 2 and Tan et al. [3] (Figure 1(c)).

Magnetic microdisks were created by laser milling (ESI 5330 UV Laser uVIA Drill, Electro Scientific Industries, Inc.) a 1.15 mil cast ribbon of Metglas 2826MB3 (Metglas, Inc.). The disks were approximately 360 μm in diameter and 29 μm in thickness, and their effective in-plane and out-of-plane susceptibilities were measured in previous work to be 12 and 1, respectively [29].

Single Disk Alignment. The three-axis electromagnetic coil system can be mounted on an inverted microscope (Nikon Eclipse, Ti-S). A single disk was suspended in a clear sample well that contained 3 mL of gellan gum of a known concentration. The sample well was placed in the induction device on the microscope with a 4× objective. The particle was aligned orthogonally to the field of view by manipulating the sample with a stir rod. Once the initial alignment was set, a rotating magnetic field at a frequency of 60 Hz was applied at various intensities, and the response of the disk was captured via video.

Multi-Disk Alignment. To see the transition from a magnetic field that would allow rotation while preventing translation to a field that would allow both modes of motion, the three-axis electromagnetic coil system was mounted on a workbench. Backlit with an LED lamp, a Nikon D90 DSLR with a macroscopic lens was mounted above the system to veiw the dynamics from above, providing adequate resolution for analysis of the alignment of these larger disks.

Multiple disks were suspended in a clear sample well that contained 5 mL of gellan gum with a concentration of 0.065%, which was found to be the lowest concentration that would prevent sedimentation. Random alignment was achieved via manual stirring. Magnetic fields at a constant frequency of 60 Hz and varying intensity were applied, and the response of the disks was captured via video.

5.4 Results and Discussion of Microdisk Alignment

Going into the experimental portion of this study, we assumed that, for a given particle of size $a > c$, we could create a suspending medium with a concentration of gellan gum $\left(\widehat{C}_{GG}\right)$ such that the yield stress of the medium would equal the gravitational stress of the particle, that is $\tau_y\left(\widehat{C}_{GG}(a,c)\right) = \tau_G$, implying $Y_G = 1$. The value of $\widehat{C}_{GG}$ can be found for any size and shape of particle in a similar manner to the procedure that was outline in the section on suppression of gravitational sedimentation. Assuming that the yield stress of the suspending media grows monotonically with the concentration of gellan gum, which is supported by the bulk results in Fig. 5.3(a), we could then choose a concentration of gellan gum that exceeds this lower limit of suppresion, $C > \widehat{C}_{GG}$.

Next, assuming that the particle has susceptibility $\chi_{\perp}^{E}$ and $\chi_{\parallel}^{E}$ and that all of our previous assumptions from our theoretical scalings held, our efforts turned to identifying two critical values of our field strength, B, that are predicted by Eq. (5.9). The first critical value, denoted by B^*, sets the lower limit of strength of the external field that is necessary to obtain alignment. The particles cannot be fully aligned at a magnetic field that is weaker than the critical value; or in other words, below this critical value, the yield stress is stronger than the stress that is necessary to align the particle. The mathematical description is shown below,

$$\exists B^* \ni \forall B < B^*,\ \tau_R < \tau_Y, \tag{5.13}$$

which can also be restated such that $Y_R < 1$.

The second critical value, denoted by B^{**}, set the upper limit of the strength of the external field. It is the maximum external field that can align the particles while preventing the translation of the particles; or in other words, above this critical value , the stress caused by the magnetic interaction between particles is stronger than the yield stress. The mathematical description is shown below,

$$\exists B^{**} \ni \forall B > B^{**},\ \tau_T < \tau_Y, \tag{5.14}$$

which can also be restated that $Y_T > 1$. Since we were interested in a proof of concept, we used the volume fraction, ϕ, to our advantage to manipulate the minimum separation distance, $\widehat{r}_0$, between suspended particles. The Eq. (5.9), which assumed that $Y_T < 1 < Y_R$, can be restated such that, for certain values of $\widehat{r}_0$, the upper limit of suppressed translation will be greater than the lower limit for the onset of rotation, $B^{**} > B^*$. Thus, we can write that a regime must exist where $B^* < B < B^{**}$.

5.4.1 Alignment of A Single Disk

Generally speaking, each concentration exhibited similar characteristics. At low field intensity, the magnetic microdisks would vibrate locally, but the did not experience any rotation. As the intensity increased, the microdisks began to rotate into planar alignment. However, upon removal of the external field, the microdisks

were found to sometimes rotate back to their initial alignment to varying degrees. This response showed that the suspending medium had a natural deformation prior to yielding that is typical of soft solids, which can allow the microdisks to rotate without causing the medium to flow. At high field intensity, the particles aligned very quickly, "snapping" into place as soon as the field is applied, and they remained aligned when the external field was removed.

The minimum magnetic field, B^*, that was required for planar alignment, regardless of the degree of recovery, was determined from the videos. Table 5.2 shows the strength of the magnetic field that was required for each concentration of gellan gum. The 0.060% concentration of gellan gum was not able to suspend microdisks, and data for this concentration is presented to identify the lower bound of bulk yield stress that allowed for microdisk suspension. The microdisks required a minimum concentration of 0.065% to stay suspended. The maximum field strength of the induction device was 7 mT, which was unable to achieve full planar alignment at concentration above 0.080%. The value of B^* increases monotonically with concentration, as expected. For fields greater than B^*, once the field was removed, the amount of recovery was loosely correlated with field intensity. In other words, microdisks that were aligned with a high field strength recovered recovered less than microdisks that were aligned with a lowered field strength. Analyzing the speed or acceleration of the rotation is hypothesized as possible avenues for describing the disruption of the local structure of gel.

Table 5.2: Values of bulk yield stress of fluids that were used in directed particle assembly experiments. The field strength that was required to induce complete orientation into the plane of the magnetic field is also presented.

C_{GG} [%]	τ_y [mPa]	B^* [mT]
0.060	23	–
0.065	25	3
0.070	26	3
0.075	31	4
0.080	33	5

The heterogeneous behavior, which was slightly evident in the tweezer experiment, was more pronounced at this larger lengthscale. In some cases, the microdisks appeared to rotate clearly about the center of mass. In others, a disk seemed to become bound to some invisible structure in the gel, and the disk would ratchet into place slightly offset from the enter of mass. For instance, on occasion, the lowest concentration, 0.065% was not as well aligned at 3 mT when compared to 0.07%.

While attempting to reset the particle alignment during experiments, relaxation motion was observed to form in the wake of the stir bar that was used to manipulate the gel. Visually, tensions that had developed specifically in the path of the stir bar within the fluid appeared to drive the fluid. In some cases, these structures were on the scale of the well, that is, much longer than the diameter of the microdisk. Though detailed characterization of these events would require a well-organized investigation, formation of such structures near a around a microdisk would likely have a significant influence on alignment.

5.4.2 Alignment of Multiple Microdisks

The investigation of the alignment of multiple disks demonstrated that translation that is caused by the induced magnetic field between microdisks is dependent on the external field and that the resulting body force can be suppressed when particles are separated by a distance of $\widehat{r}_0 \sim 10a$.

Figure 5.5 shows a sequence of photographs as the field strength was increased. At a field strength of 1 mT, a few particles were rotating into alignment. At both 3 mT and 5 mT, all particles are observed to fully align with no translational motion. This observation was consistent with the results from the previous section that determined the minimum field strength that was needed for complete alignment for an isolated particle was $B^*\left(C_{GG} = 0.065\%\right) = 3$ mT. At 7 mT, particle 3 began to spin substantially, migrating from its initial position and sedimenting to the bottom of the well.

Figure 5.5 shows a second sequence of photographs as the field strength was increased. At 5 mT, all particles were observed to fully align with no translational motion. This observation was again consistent with the results from the previous section that determined that minimum field strength that was needed for complete alignment was $B^*\left(C_{GG} = 0.065\%\right) = 3$ mT for a single particle. At 7 mT, translation and eventual sheeting with other microdisks was observed; thus $B^{**}\left(C_{GG} = 0.065\%, \widehat{r}_0 \sim 10a\right) = 7$ mT. At higher concentrations of suspending

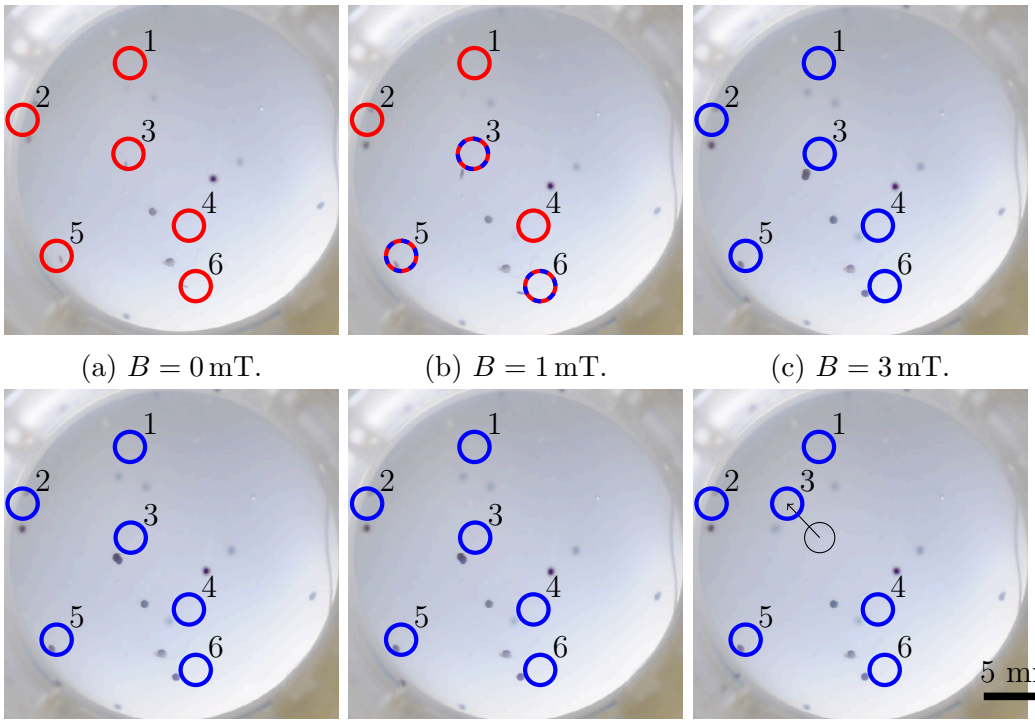

(a) $B = 0\,\mathrm{mT}$. (b) $B = 1\,\mathrm{mT}$. (c) $B = 3\,\mathrm{mT}$.

(d) $B = 5\,\mathrm{mT}$. (e) $B = 7\,\mathrm{mT}$. (f) $B = 7\,\mathrm{mT}$.

Figure 5.5: Directed alignment of Ni-Fe microdisks (360-μm diameter) in 0.065% gellan gum. Field strength was increased sequentially from 0 to 7 mT. (a) Initial particle positions before an induced, rotating magnetic field was applied. (b) A field strength of 1 mT was applied. Particles 3, 5, and 6 exhibited vibrational motion without full rotation or translation. (c) A 3-mT field strength was applied. Particles 2, 3, and 6 snapped into the plane of the magnetic field. Particles 1 and 4 also snapped into the plane, as they are now evident. Another particle has translated to the location of particle 3, as they were most likely very close before the field strength was increased. (d) Little change exists after the field strength was increased, aside from the obvious rotation of particle 3 and its partner. (e) At 7 mT, rotation of particle 3 and its partner was substantial, leading to translation as they spun through the fluid. (f) After a time of 15 s, particle 3 had moved laterally in the sample, as well as sedimenting to the bottom of the well.

medium, we were able to align the particles at various field strengths that were consistent with the results from the alignment of single particles. However, we were unable to produce large enough magnetic fields to induce chaining and identify B^{**}.

From these results, we can calculate a quick approximation for the proportionality constants from the inequality in Eq.(5.9) at the concentration of $C_{GG} = 0.065\%$. From Table 5.1 we see that the microscopic yield stress is $\tau_Y = 4.2$ Pa. Thus, the necessary field strength for rotation, $B^* = 3$ mT, implied that the proportionality constant for rotation is $k_R = 0.6$. Finally, the necessary field strength for translation, $B^{**} = 7$ mT, implied that the proportionality constant for translation is $k_T = 7.5$.

5.5 Conclusions and Future Works

Nanocomposites, made of ferromagnetic nanoparticles in a dielectric, non-magnetic matrix, offer unparalleled opportunities for innovation in electromagnetic materials — the size, shape, concentration, and orientation of the particles in the matrix can be readily varied to realize a wide range of magnetic and dielectric characteristics. Voxel-by-voxel alignment of fillers would allow the creation of functionalized gradient materials with potentially important opportunities for new applications, including diffusion and conduction [132–134].

This formulation could, at a minimum, allow bulk composites with even distribu-

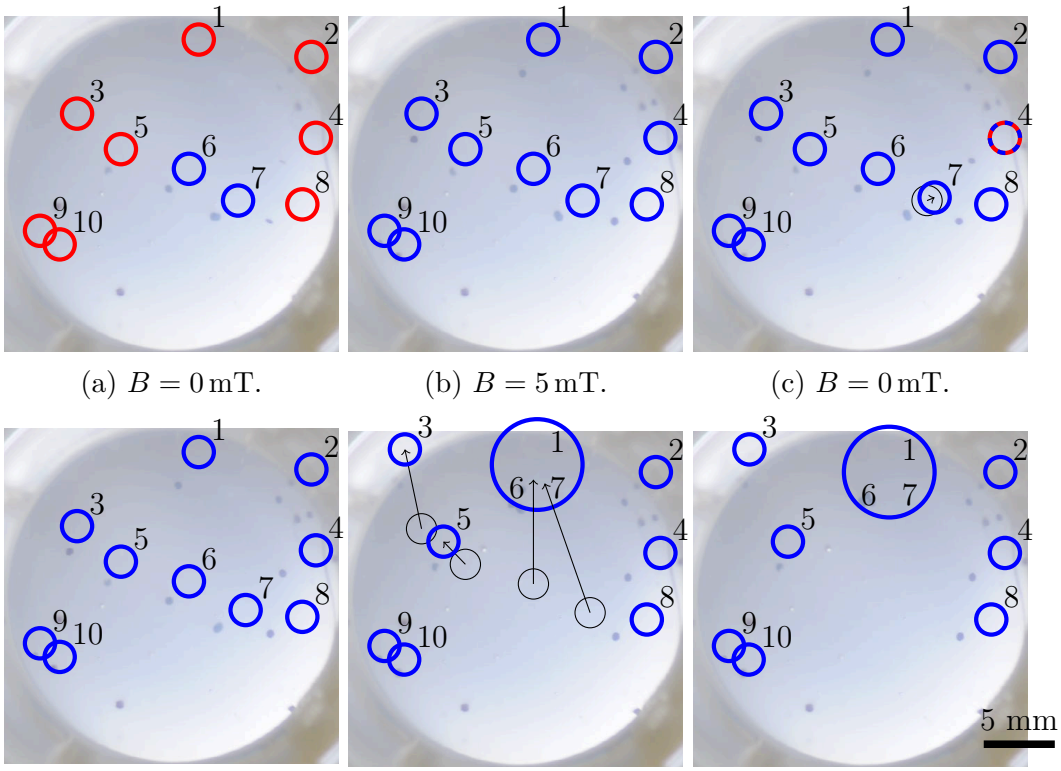

(a) $B = 0\,\mathrm{mT}$. (b) $B = 5\,\mathrm{mT}$. (c) $B = 0\,\mathrm{mT}$.

(d) $B = 7\,\mathrm{mT}$. (e) $B = 7\,\mathrm{mT}$. (f) $B = 7\,\mathrm{mT}$.

Figure 5.6: Directed alignment of Ni-Fe microdisks (360-μm diameter) in 0.065% gellan gum. Field strength was increased from 0 to 7 mT. (a) Initial particle positions before an induced, rotating magnetic field was applied. (b) A field strength of 5 mT was applied. All particles became aligned. (c) The external field was removed. Some particles (e.g., particle 4) experienced some rotation back out of alignment. Particle 7, which seemed to consist of two particles that were stuck together, migrated slightly, as the particle slowly rotated. (d) A field strength of 7 mT was applied. All particles became aligned again. (e) While the field strength was held at 7 mT, multiple particles began migrating. After a time of 39 s, Particles 6 and 7 chained before migrating towards particle 1. (f) Particles 1, 6, and 7 formed a sheet of particles.

tion of the center of mass to be formed. Further, this strategy should be easily incorporated into layer-by-layer deposition of material to form composites with layer-dependent orientation. Obviously, the addition of this strategy to voxel-by-voxel efforts will bring added complexities in terms of distributing the droplets, but, given the difficulties in preventing chaining when it is unwanted, the potential for success is worth investigating. The use of inkjet printing technologies allows for the incorporation of voxel-by-voxel filler alignment and effects of *filler concentration* to be leveraged. These technological opportunities drove our interest in using a suspending medium with a yield stress that can prevent chaining but allow orientation of filler particles while still be processable.

5.5.1 Theoretical Scalings

Within this manuscript, we sought validation for our experimental efforts by deriving a number of scalings that guided our choice for our suspending medium. First, we outlined a scaling for the spacing of sheets of magnetic particles that are a single particle in thickness, which could be used as a design parameter for creating composites with defined interstitial spacing in two dimensions. Next, we derived a ratio between the timescales of rotation and translation of an oblate spheroid in a linear fluid, which justifies the overall need for using a more complicated suspending medium to suppress chaining. Then, we derived the relevant scales of stress for rotation and translation of an oblate spheroid. These stress scalings, combined with the idea of a fluid with a yield stress, allowed the deriva-

tion of the necessary inequality to ensure that rotation is allowed and translation is suppressed. Finally, we derived a scaling for the maximum volume fraction that could maintain this inequality, given a disk-like filler particle with a given shape and susceptibility.

5.5.2 Suppression of Magnetic Migration

The experimental results show that, as the concentration of gellan gum was increased, a higher magnetic field was required to induce translation, implying that the yield stress of the fluid at the microscopic scale grows monotonically with the polymer concentration. However, the behavior was somewhat heterogeneous. In some cases, particles experiencing translation appeared to migrate past particles that seem to still be bound by the yield stress. This observation is reasonable considering that a moving particle will have already exceeded the yield stress, and its local environment will flow. Further, weakness in the polymer microstructure could create local environments that are unable to resist flow relative to another location.

5.5.3 Alignment of A Single Microdisk

The experimental results from the alignment of a single microdisk showed that the critical value, B^*, that is necessary for alignment grows monotonically with the concentration of gellan gum in the suspending medium and with the yield stress of the medium, as expected. When the process was viewed at low frequencies, com-

plex behavior in the far field was observed in the gellan gum. Thorough analysis of this process via particle image velocimetry could provide unique insight into these complex materials. The nonlinear and heterogeneous behavior of this gellan gum ultimately made rotational dynamics difficult to determine. A large number of independent trials would be required to tell a detailed story. In this case, the number of available microdisks was limited, which prevented a more statistically rigorous design of experiments. The addition of a high-speed camera would aid observations of any complex motion (e.g., ratcheting) that would promote permanent rotation.

5.5.4 Alignment of Multiple Microdisks

The proof of concept that a fluid with a yield stress can allow rotation to orient filler particles that are subject to an external body force while preventing their translation was a success. Although detailed experiments at smaller lengthscales are necessary to identify the limitations of this concept, this framework could lead to new processes that are based on aligning filler particles in a fluid that can be molded in any shape. Coupled with an event to permanently solidify the shape, novel composites that incorporate voxel-level orientation (and concentration) of filler particles for gradient materials could soon be reality.

The field strength that was required to induce complete orientation into the plane of the magnetic field is also presented.

Chapter 6

Future Work

In this study, we investigated the dynamics of single microdisk, dynamics and rheology of multiple spheres and microdisks, experimental characterization of a complex fluids using microrheological properties, and a proof-of-concept study that combines the knowledge of dynamics that was developed earlier and the knowledge of microrheological properties.

Some parts of this study is still under investigation, i.e., improve the performance of Stokesian dynamics and a new method of microrheology.

6.1 Modification of Stokesian Dynamics

Our goal is to establish dynamics and rheology of particles with various geometries that are suspended in a fluid with or without external field. It requires an accurate model of magnetic interactions among spheres. To our knowledge, we haven't seen any work that includes both the accurate magnetic interactions and hydrodynamic interactions of spherical particles, not to mention the more complicated geometries. Bonnecaze's [36, 135] works established an accurate electrostatic interactions among spheres in an ER fluid, but no one has done MR fluid yet. Also, our current simulation is limited to small scale due to the high computational cost of our current code. The most time-consuming part of the code is the inverse of the mobility tensor $\mathcal{M}^{\infty}$ of which the operation is at the order of N^3. If we wish to simulate particles with high aspect ratio or in a high-volume fraction, we need to include many particles in our system so the simulation cell is significantly larger than the particle's size, which makes the simulation costly to run. But, the simulation can be accelerated by using iterative inversion of the tensors and the computational scaling can be reduced to the order of N^2. Sierou and Brady's [136] work has accelerated the simulation to an order of $N \log N$ by using particle mesh ewald (PME). We are in the process of developing the codes using these methods.

6.2 Magnetic Nanorheology

The microrheolgy, or specifically the multiple particle tracking microrheology, provides a useful way of characterizing fluids. However, this technique and other microrheological techniques require samples that can be visualized by microscope. Also, it can only do in vitro detection. If the sample is opaque, or needs to be monitored in vivo. Microscopy cannot be used. For example, if we want to measure the rheological properties of synovial fluids of an injured knee and want to monitor the change of properties over a period of time, it is not practical to draw the fluid out repeatedly. The conventional microrheological techniques are not convenient in this case. In this section, a new technique will be introduced and the application to rheology will be discussed. This is a project that just takes off. We would like to show some results we have so far.

The magnetic resonance spectroscopy of Brownian relaxation (MSB) is a new technique of magnetic sensing [117]. Under an external magnetic field, the moments of magnetic particles tend to be aligned with the field, as introduced earlier, but the thermal energy will drive the particle out of alignment. The time between the unaligned state to the aligned state is called the *Brownian relaxation time*. If the magnetic particle's size decreases below a critical size, the direction of magnetization will randomly flip due to the thermal energy of the atoms. We call the time between two flips the *Néel relaxation time.* In this study, the Néel relaxation time is assumed to be much larger than the Brownian relaxation time. In other words,

when a magnetic field is applied, the magnetic particle will be aligned mechanically instead of the flipping of magnetization.

In a specific experiment, an in-phase susceptibility χ' and out an out-of-phase susceptibility χ'' are measured, and the susceptibility is related to the property of the fluid. This measurement does not request a clear sample.

In the rest of this section, we will discuss some models regarding the relationship between the rheological properties of the fluid and the measured susceptibility. We start with the Germant-DiMarzio-Bishop model [118]

$$\frac{\chi^* - \chi_\infty}{\chi_0 - \chi_\infty} = \frac{1}{1 + KG^*}, \tag{6.1}$$

where χ^* is the complex susceptibility such that $\chi^* = \chi' - i\chi''$, χ_∞ is the susceptibility measured at an infinitely-large frequency, χ_0 is the susceptibility measured in a DC field, K is a parameter given by $K = \frac{4\pi a^3}{k_B T}$.

By decoupling the in-phase part and out-of-phase part of both χ^* and G^*, we obtain

$$G' = \frac{1}{K}\left(\frac{\chi'_N}{\chi'^2_N + \chi''^2_N} - 1\right), \text{ and} \tag{6.2a}$$

$$G'' = \frac{1}{K}\frac{\chi''_N}{\chi'^2_N + \chi''^2_N}, \tag{6.2b}$$

where

$$\chi'_N = \frac{\chi' - \chi_\infty}{\chi_0 - \chi_\infty}, \text{ and} \tag{6.3a}$$

$$\chi''_N = \frac{\chi''}{\chi_0 - \chi_\infty}. \tag{6.3b}$$

6.2.1 Newtonian Fluid

For a Newtonian fluid, $G' = 0$, and $G'' = \omega\eta$, substituting them into Eq. (6.2a) and (6.2b) we obtain

$$\chi'_N = \frac{1}{1 + K^2\omega^2\eta^2}, \text{ and} \tag{6.4a}$$

$$\chi''_N = \frac{K\omega\eta}{1 + K^2\omega^2\eta^2}. \tag{6.4b}$$

Figure 6.1 plots the susceptibilities as functions of frequency ω with arbitrarily chosen parameters $K = 1$ and $\eta = 1$.. The peak of χ''_N is shown to be $\frac{1}{K\eta}$. Thus, the viscosity of a Newtonian fluid can be found by finding the critical frequency, ω_c that corresponds to the peak of χ''_N.

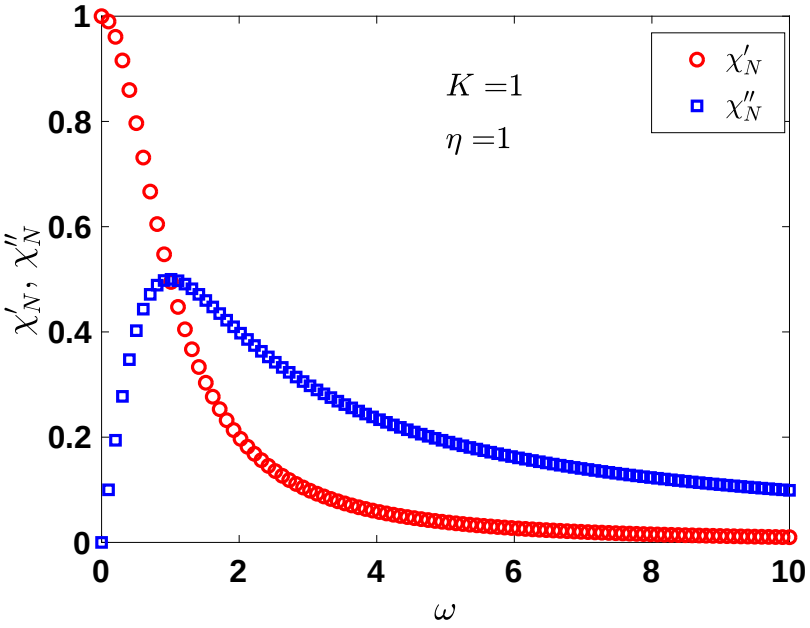

Figure 6.1: Susceptibility χ'_N and χ''_N versus frequency ω. The parameters are chosen arbitrarily that $K = 1$ and $\eta = 1$. The peak of χ''_N happens at $\omega_c = \frac{1}{K\eta}$.

6.2.2 Hookean Solid

For a Hookean solid, $G'' = 0$, and $G' = G$, substituting them into Eq. (6.2a) and (6.2b) we obtain

$$\chi'_N = \frac{1}{1 + KG}, \text{ and} \tag{6.5a}$$

$$\chi''_N = 0. \tag{6.5b}$$

Both the in-phase and out-of-phase susceptibilities are constant in this case. When the particle is embedded in a solid, the particle is not able to rotate, thus the susceptibilities do not change with frequency.

Next, we will discuss the cases of suspending particles in viscoelastic fluids. We discuss two specific cases — Kevin-Voigt fluid and Maxwell — two simplest models that describe viscoelastic fluids.

6.2.3 Kevin-Voigt Model

Kevin-Voigt model describes a viscoelastic fluid in terms of a dashpot paralleled with a spring, as shown in Fig. 6.2. The mathematical description of Kevin-Voigt model is

$$G^* = G\left(1 + i\omega\tau\right), \tag{6.6}$$

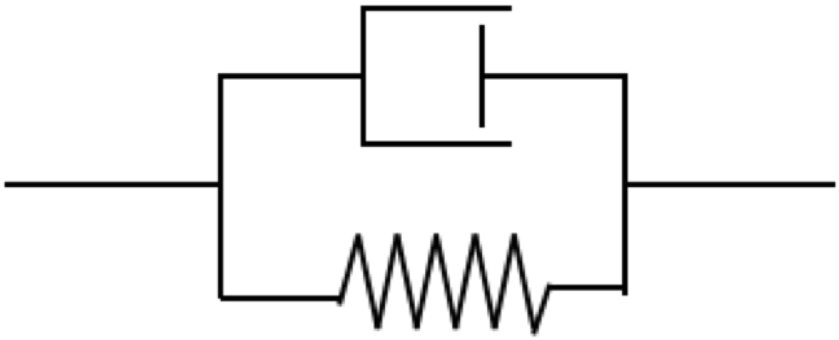

Figure 6.2: Kevin-Voigt model of viscoelastic fluid. A dashpot is paralleled by a spring.

and

$$G' = G, \text{ and} \tag{6.7a}$$

$$G'' = G\omega\tau \tag{6.7b}$$

where G is the relaxation modulus and τ is the relaxation time, two parameters depending on the material. Substituting the modulus into Eq. (6.2a) and (6.2b) we obtain

$$\chi'_N = \frac{KG+1}{(KG+1)^2 + (KG\omega\tau)^2}, \text{ and} \tag{6.8a}$$

$$\chi''_N = \frac{KG\omega\tau}{(KG+1)^2 + (KG\omega\tau)^2}. \tag{6.8b}$$

We can find the critical frequency, ω_c, that corresponds to the peak of χ''_N, as shown in Fig. 6.3, that

$$\omega_c = \frac{1+KG}{KG\tau}. \tag{6.9}$$

We also note that as the frequency goes to zero,

$$\chi'_N(\omega \to 0) \to \frac{1}{KG+1}, \text{ and} \tag{6.10a}$$

$$\chi''_N(\omega \to 0) \to 0. \tag{6.10b}$$

Thus, by fitting χ'_N and χ''_N data, and so by finding the critical frequency, ω_c, and zero-frequency in-phase susceptibility, χ'_N, we are able to obtain the properties, G and τ, of Kevin-Voigt fluid.

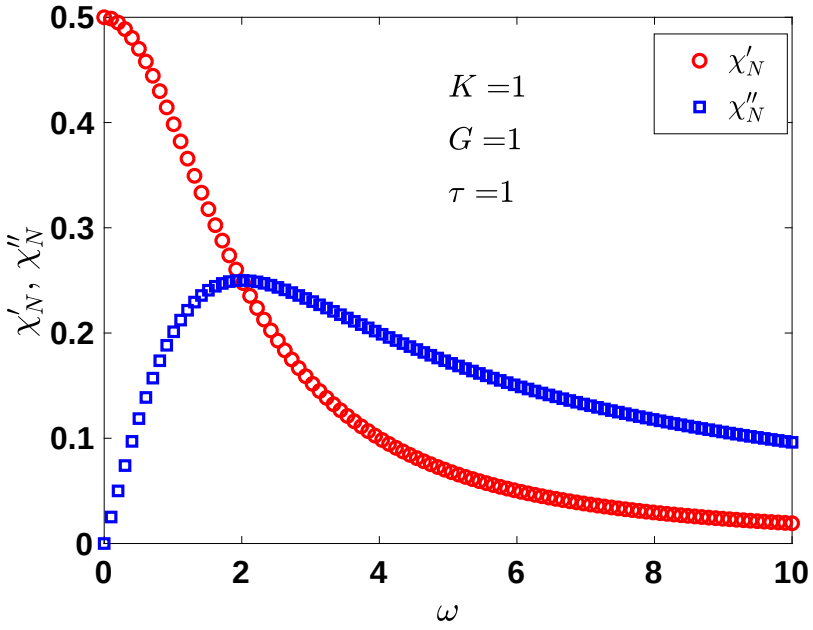

Figure 6.3: Susceptibility χ'_N and χ''_N versus frequency ω of a Kevin-Voigt fluid. The parameters are chosen arbitrarily that $K = 1$, $G = 1$, and $\tau = 1$. The peak of χ''_N happens at $\omega_c = \frac{1+KG}{KG\tau}$.

6.2.4 Maxwell Model

Maxwell model describes a viscoelastic fluid in terms of a dashpot connected with a spring, as shown in Fig. 6.4. The mathematical description of Maxwell model is

$$G^* = \frac{Gi\omega\tau}{1 + i\omega\tau}. \tag{6.11}$$

We write it in terms of the elastic and viscous modulus such that

$$G' = \frac{G\omega^2\tau^2}{1 + \omega^2\tau^2}, \text{ and} \tag{6.12a}$$

$$G'' = \frac{G\omega\tau}{1 + \omega^2\tau^2}. \tag{6.12b}$$

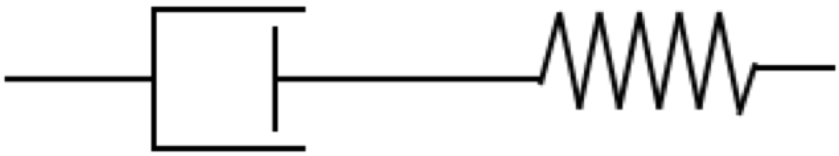

Figure 6.4: Maxwell model of viscoelastic fluid. A dashpot is connected with a spring.

Similarly, we can obtain the susceptibilities by combining with Eqs. (6.2a) and (6.2b) that

$$\chi'_N = \frac{\frac{KG\omega^2\tau^2}{1+\omega^2\tau^2} + 1}{\left(\frac{KG\omega^2\tau^2}{1+\omega^2\tau^2} + 1\right)^2 + \left(\frac{KG\omega\tau}{1+\omega^2\tau^2}\right)^2}, \text{and} \tag{6.13a}$$

$$\chi''_N = \frac{\frac{KG\omega\tau}{1+\omega^2\tau^2}}{\left(\frac{KG\omega^2\tau^2}{1+\omega^2\tau^2} + 1\right)^2 + \left(\frac{KG\omega\tau}{1+\omega^2\tau^2}\right)^2}, \tag{6.13b}$$

and the susceptibilities are plotted in Fig. 6.5.

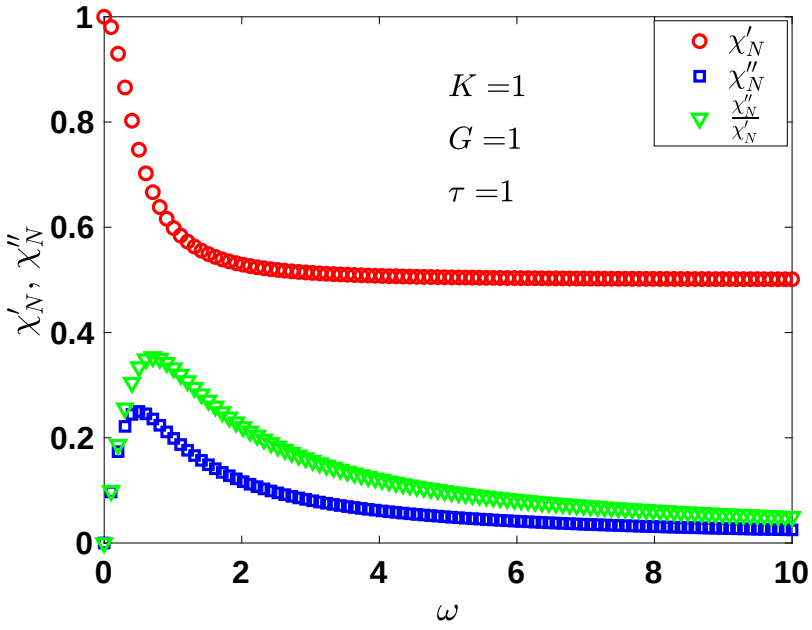

Figure 6.5: Susceptibility χ'_N and χ''_N versus frequency ω of a Kevin-Voigt fluid. The parameters are chosen arbitrarily that $K = 1$, $G = 1$, and $\tau = 1$. The critical frequency $\widehat{\omega}_c$ corresponds to the peak of χ_r and is found that $\widehat{\omega}_c = \tau^{-1}$.

In contrast to the case of Kevin-Voigt model where the fluid's relaxation modulus G is found at the zero-frequency limit, the relaxation modulus of Maxwell model is found at the high-frequency limit such that

$$\chi'_N(\omega \to \infty) \to \frac{1}{KG+1}, \text{ and} \tag{6.14a}$$

$$\chi''_N(\omega \to \infty) \to 0. \tag{6.14b}$$

The relaxation time τ is buried in the critical frequency, ω_c, at which χ''_N is maximum. Finding τ requires solving the equation $\frac{\partial}{\partial\omega}\chi''_N = 0$. Unfortunately, this equation is prohibitive to solve because of the complicated form of χ''_N. But, if we take a ratio between χ'_N and χ''_N and denote it as χ_r such that

$$\begin{aligned}\chi_r &= \frac{\chi''_N}{\chi'_N} \\ &= \frac{KG\omega\tau}{(1+\omega^2\tau^2)+KG\omega^2\tau^2}.\end{aligned} \tag{6.15}$$

The ratio, χ_r, is much easier to deal with, and we obtain the solution that

$$\frac{\partial\chi_r}{\partial\omega} = 0 \quad \to \quad \widehat{\omega}_c = \frac{1}{\tau}. \tag{6.16}$$

The hat on the critical frequency means that it is found according to χ_r instead of χ''_N. Thus, if we fit the data of χ'_N and χ_r and find the critical frequency, $\widehat{\omega}_c$, from χ_r and high-frequency in-phase susceptibility, χ'_N, we are able to obtain the properties of Maxwell fluid.

APPENDICES

Appendix A

Derivations in Single Particle Dynamics

A.1 Oblate Spheroid Resistance Tensor

For any resistance tensor, $\mathcal{R}$, a corresponding mobility tensor, $\mathcal{M}$, exists such that $\mathcal{R} \cdot \mathcal{M} = \mathbf{I}$ [42]. Multiplying both sides of Eq. (2.5), under the condition of quiescent fluid, by a mobility tensor M_{im} that corresponds to C_{ij}, the following

expression is obtained for the angular velocity

$$\omega_m = M_{im}\varepsilon_{ijk}\mu_j B_k - M_{im}\varepsilon_{ijk}p_j\frac{\partial\left[k_B T\log\Psi\right]}{\partial p_k}. \tag{A.1}$$

Substituting Eq. (A.1) into Eq. (2.8) gives an explicit expression for the orientation rate of change,

$$\frac{dp_\ell}{dt} = M_{im}\varepsilon_{\ell mn}\varepsilon_{ijk}\mu_j B_k p_n - M_{im}\varepsilon_{\ell mn}\varepsilon_{ijk}p_j p_n\frac{\partial\left[k_B T\log\Psi\right]}{\partial p_k}. \tag{A.2}$$

The mobility tensor for an axisymmetric particle has the following form

$$M_{im} \equiv C_1\delta_{im} + C_2 p_i p_m. \tag{A.3}$$

We substitute the mobility tensor into Eq. (A.2) to have

$$\begin{aligned}\frac{dp_\ell}{dt} =& C_1\varepsilon_{\ell in}\varepsilon_{ijk}\mu_j B_k p_n + C_2\varepsilon_{\ell mn}\varepsilon_{ijk}p_m p_n p_i\mu_j B_k \\ &- C_1\varepsilon_{\ell in}\varepsilon_{ijk}p_j p_n\frac{\partial\left[k_B T\log\Psi\right]}{\partial p_k} - C_2\varepsilon_{\ell mn}\varepsilon_{ijk}p_m p_n p_i p_j\frac{\partial\left[k_B T\log\Psi\right]}{\partial p_k}.\end{aligned} \tag{A.4}$$

Since the product of a symmetric tensor and an anti-symmetric tensor is zero, the product $\varepsilon_{\ell mn}p_m p_n$ is null, where $\varepsilon_{\ell mn}$ is anti-symmeetric in m and n, while $p_m p_n$ is symmetric in m and n. Thus, the second and fourth terms of Eq. (A.4) are zero, and only terms containing C_1 remain. Therefore, only the isotropic term of M_{im}, or equivalently C_{ij}, plays a role in the rotation of an oblate spheroid. We can thus

write

$$C_{ij} = \zeta_r \delta_{ij}, \tag{A.5}$$

where ζ_r is equal to $8\pi\eta a^3 Y^C$ from Eq. (2.6). If the aspect ratio is very large, then $Y^C = \frac{4}{3\pi}$ and $C_{ij} = \frac{32\eta a^3}{3}\delta_{ij}$.

A.2 High Peclét Limit

Now we have the resistance tensor and we can write the governing equation as

$$\frac{dp_i}{dt} = -\frac{\left(\chi_\perp^E - \chi_\parallel^E\right) V}{\mu_0 \zeta_r} B_n p_n \left(B_i - B_k p_k p_i\right) - \frac{k_B T}{\zeta_r}\frac{\partial \log \Psi}{\partial p_i}. \tag{A.6}$$

A "rotational Peclét number" is defined as the ratio between the magnetic torque and Brownian torque such that

$$\begin{aligned} Pe_r &= \frac{\left(\chi_\perp^E - \chi_\parallel^E\right) V B_n p_n \left(B_i - B_k p_k p_i\right)}{\mu_0 k_B T} \\ &\sim \frac{\left(\chi_\perp^E - \chi_\parallel^E\right) V B^2}{\mu_0 k_B T}. \end{aligned} \tag{A.7}$$

The Peclét number in this study is very high ($\mathcal{O}\left[10^4\right]$). Thus the Brownian torque can be neglected.

A.3 Derivation of Solution of Rotating Field

To solve Eq. (2.17a), separating the variables and integrating gives

$$\int \frac{du}{\sin 2u - \xi} = \begin{cases} \frac{1}{2\sqrt{1-\xi^2}} \log\left[\frac{-\xi\tan u+1-\sqrt{1-\xi^2}}{-\xi\tan u+1+\sqrt{1-\xi^2}}\right] & \text{if } \xi < 1 \\ -\frac{1}{\cot u - 1}, & \text{if } \xi = 1 \\ \frac{1}{\sqrt{\xi^2-1}} \arctan\left[\frac{1-\xi\tan u}{\sqrt{\xi^2-1}}\right], & \text{if } \xi > 1 \end{cases} \tag{A.8}$$

which provides the need for separate cases depending on the value of ξ. The solution of Eq. (2.17a) has the form

$$X = D\tau + X_0, \tag{A.9}$$

as seen in Eqs. (2.22c), (2.24c) and (2.26c), where D is a constant. Now, Eq. (2.17b) can be integrated such that

$$\int \frac{d\theta}{\sin 2\theta} = -\int \frac{1}{2}\cos^2 u d\tau, \;\Rightarrow\; \log\left[\tan\theta\right] = -\int \frac{1}{1+\tan^2 u} d\tau. \tag{A.10}$$

Here $\left[1+\tan^2 u\right]^{-1}$ is used instead of $\cos^2 u$, since Π and K are expressed as $\tan u$, and the integrand in Eq. (A.10) can be transformed according to Eq. (2.22a) and (2.26a).

A.4 Low-ξ Expansion

The alignment time appears to scale as ξ^{-2} at $\xi \ll 1$. To validate the scaling constant, a Taylor expansion around $\xi = 0$ on the low-ξ solution is necessary. Writing the Taylor expansion around $\xi = 0$ for the Γ-terms gives

$$\Gamma_1 = \left(\lambda_2 - \lambda_1\xi + \frac{3\lambda_2 + \lambda_0}{4}\xi^2 + \mathcal{O}\left[\xi^4\right]\right) e^{-\tau\left(\frac{\xi^2}{2} + \mathcal{O}\left[\xi^4\right]\right)}, \tag{A.11a}$$

$$\Gamma_2 = \left(\lambda_0 - \lambda_1\xi + \frac{\lambda_2 + 3\lambda_0}{4}\xi^2 + \mathcal{O}\left[\xi^4\right]\right)\left(1 + \frac{\xi^2\tau}{2} + \mathcal{O}\left[\xi^4\right]\right) e^{-2\tau}, \text{ and} \tag{A.11b}$$

$$\Gamma_3 = \left(2\lambda_1\xi - (\lambda_0 + \lambda_2)\,\xi^2 + \mathcal{O}\left[\xi^4\right]\right) e^{-\tau}. \tag{A.11c}$$

Because the exponentials in Γ_2 and Γ_3 decay much faster than the exponential decay in Γ_1, the value of Γ_1 is much greater than the values of Γ_2 and Γ_3 when $\tau \gg 1$. Therefore, Eq. (2.27) can be simplified to be

$$\frac{\tan\theta}{\tan\theta_0} \approx [\Gamma_1]^{1/2}. \tag{A.12}$$

Keeping the leading terms in Γ_1 such that $\Gamma_1 \approx \lambda_2 \exp\left[-\frac{\tau\xi^2}{2}\right]$, Eq. (A.12) becomes Eq. (2.30).

A.5 Stability Analysis of Alignment of Microdisk

Even though the analytic solutions have been derived, it is still desired to predict the dynamics without obtaining the complicated expressions. In this section, a

stability analysis is carried out to describe the dynamics for different values of ξ. The method used in this study for the stability analysis follows the book by Strogatz [137].

A.5.1 $\xi = 0$

In the constant field case, we plot the Eq. (2.17a) in terms of u versus $\frac{du}{d\tau}$ as shown in Fig. A.1. The red arrow indicates the *flow* of u and we can see that u flows to $\pi/2$ while away from 0, so we can say that $\pi/2$ is the *stable node* while 0 is the *unstable node* (the periodicity is π). Unless the microdisk initially starts with the orientation vector perfectly orthogonal to the field vector, the microdisk will be one-dimensional aligned as discussed before.

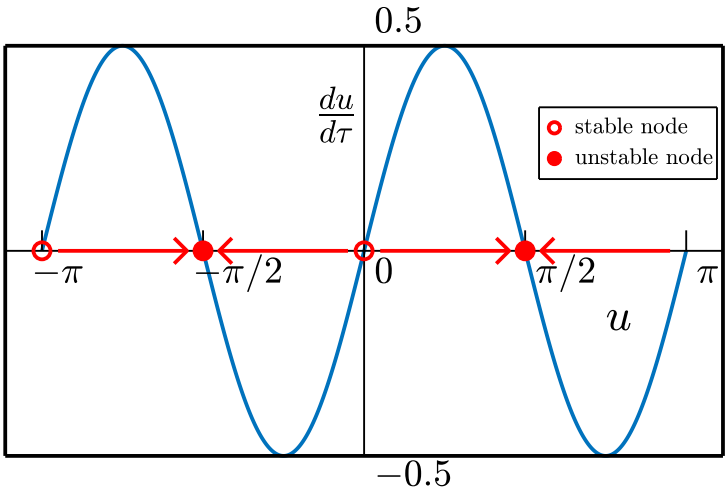

Figure A.1: The rate of change of u versus u at $\xi = 0$. The stable node is shown to be $\pi/2$ and the unstable node 0.

A.5.2 $\xi < 1$

In the slow-rotating field case, the stable node is $u = \frac{\pi}{2} - \frac{\arcsin \xi}{2}$ and the unstable node is $u = \frac{\arcsin \xi}{2}$, as shown in Fig. A.2. The field rotates so slowly that the particle is able to catch up with the field, and the phase shift does not change with time. The particle can spin synchronously with the external field; and the particle is *phase-locked* with respect to the external rotating field.

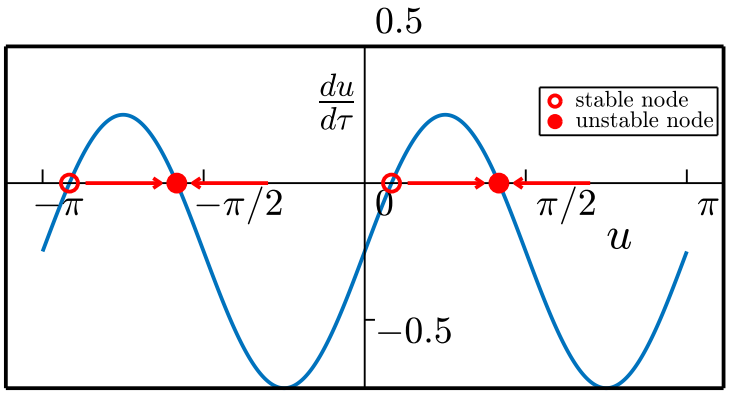

Figure A.2: The rate of change of u versus u at $\xi = 0$. The stable node is shown to be $\pi/2 - \arcsin \xi/2$ and the unstable node $\arcsin \xi/2$.

A.5.3 $\xi = 1$

In the case of $\xi = 1$, the stable node and unstable node collapse into a single *saddle point* at $u = \frac{\pi}{4}$, as shown in Fig. A.3. The saddle point is not stable, but it attracts all the trajectories toward it. But for u that starts initially smaller to

$\frac{\pi}{4}$ goes through a large *excursion* before it reaches to $\frac{\pi}{4}$, as shown in Fig. A.3. The motion of the particle is changed from phase-locked to *phase-ejected* at $\xi = 1$, where the external field is rotating at a frequency that is equal to the intrinsic frequency.

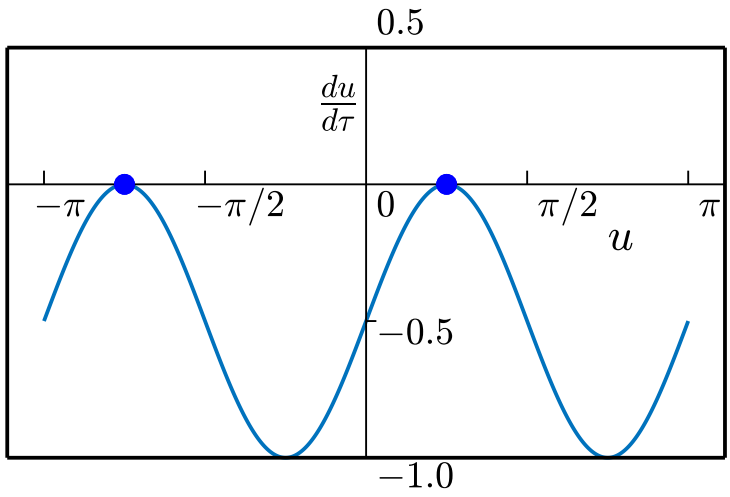

Figure A.3: The rate of change of u versus u at $\xi = 0$. The stable node and unstable node collapse into a single saddle point at $\pi/4$.

A.5.4 $\xi > 1$

In the case of $\xi > 1$, there is not fixed point of u, as shown in Fig. A.4. The field is rotating so fast that the particle "sees" the field everywhere. It cannot follow up with the rotating field, so the particle is *phase-ejected* with respect to the field.

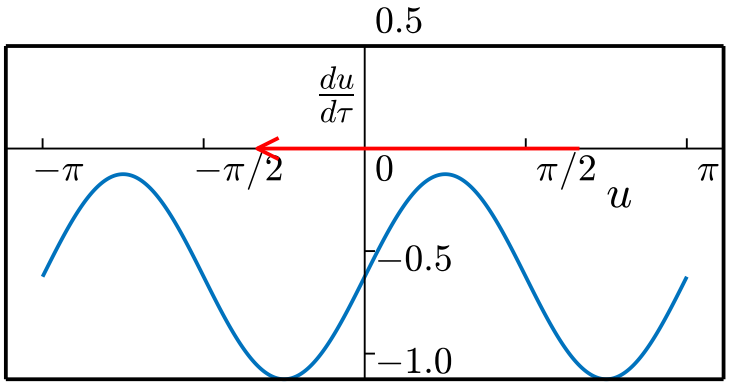

Figure A.4: The rate of change of u versus u at $\xi = 0$. No stable/unstable node or saddle point is found and u keeps changing.

Appendix B

Ewald Summation

B.1 Introduction

In simulating *homogeneous* infinite systems such that we let the number of particles, N, go to infinity, volume of the system, V, go to infinity, and keep N/V fixed, we often take a finite number of particles in a simulating box, the *primary cell*, and replicate it *periodically* in space, as shown in Fig. B.1. Avoiding calculation of pair interactions among all the particles is crucial; otherwise, the computational efforts would become prohibitive. Thus, we need to truncate the number of parti-

cles or the number of cells. However, if the interactions are *long-range* (decays no faster than $1/r^3$) such as electrostatic interaction or the hydrodynamic interaction, the infinite summation of the interactions converges very slowly, and the accuracy depends on the order of summation.

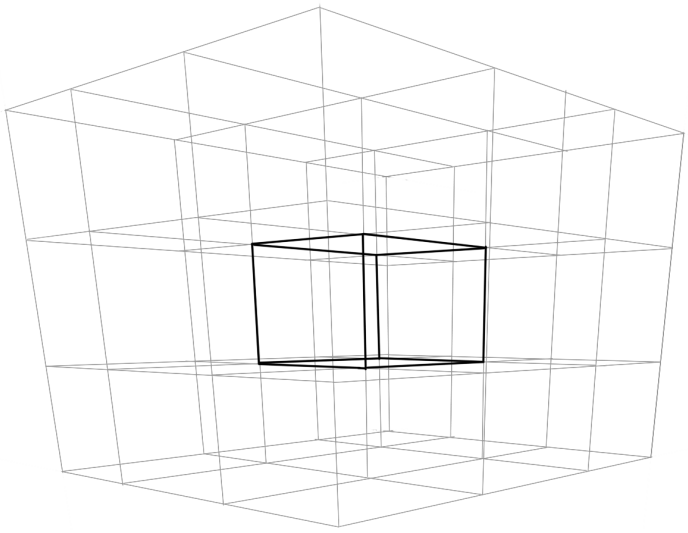

Figure B.1: The simulation cells periodically positioned in space. The primary cell is in dark line.

Ewald summation is a method that is used to calculate electrostatic energies of ionic crystals that can converge fast. It provides a method to calculate the long-range interaction by splitting the interaction into a short-range contribution, which converges fast in the real space, and a long-range contribution, which converges fast in the Fourier space. Beenakker [69] calculated the Ewald summation of hydrodynamic interactions. We will present the technique briefly here.

We write the mobility problem such that

$$\begin{pmatrix} \mathbf{U} \\ \boldsymbol{\Omega} \\ \mathbf{E} \end{pmatrix} = \begin{pmatrix} \mathbf{a} & \widetilde{\mathbf{b}} & \widetilde{\mathbf{g}} \\ \mathbf{b} & \mathbf{c} & \widetilde{\mathbf{h}} \\ \mathbf{g} & \mathbf{h} & \mathbf{m} \end{pmatrix} \cdot \begin{pmatrix} \mathbf{F} \\ \mathbf{T} \\ \mathbf{S} \end{pmatrix},$$

and $\mathbf{a}$, $\mathbf{b}$, etc are the sub-matrices of the grand mobility tensor $\mathcal{M}^{\infty}$. The sub-matrices are calculated based on the stokeslet, $\mathbf{J}$. In this section, we take $\mathbf{a}$, the *Rotne-Prager tensor*, as an example to see how Ewald summation is applied.

B.2 Ewald Summation of Rotne-Prager Tensor

We write the velocity of particle α in terms of the tensor $\mathbf{a}$ and the force $\mathbf{F}$ in a periodic system such that

$$\mathbf{U}^{\alpha} = \frac{1}{6\pi\eta a} \sum_{\mathbf{n}} \left(\sum_{\beta=1}^{N} \mathbf{a}^{\alpha\beta} \cdot \mathbf{F}^{\beta} \right), \tag{B.1}$$

where $\mathbf{n}$ is the position vector of simulation cell, and we denote $\mathbf{n} = 0$ the primary cell. We can rewrite the velocity of particle α as

$$\mathbf{U}^{\alpha} = \frac{1}{6\pi\eta a} \mathbf{a}^{\alpha\alpha} \cdot \mathbf{F}^{\alpha} + \frac{1}{6\pi\eta a} \sum_{\mathbf{n}} \left(\sum_{\beta=1}^{N}{}' \mathbf{a}^{\alpha\beta} \mathbf{F}^{\beta} \right), \tag{B.2}$$

where the prime sign means that $\alpha \neq \beta$ when $\mathbf{n} = 0$. The self-interaction and pair-interaction Rotne-Prager tensors are

$$\mathbf{a}^{\alpha\alpha} = \mathbf{I}, \text{ and} \tag{B.3a}$$

$$\mathbf{a}^{\alpha\beta} = \left(\frac{3}{4} + \frac{1}{4}\nabla^2\right)\mathbf{J}. \tag{B.3b}$$

We will focus on deriving the Ewald summation of $\mathbf{a}^{\alpha\beta}$ in the rest of this section. We write the stokeslet $\mathbf{J}$ here

$$J_{ij} = \frac{\delta_{ij}}{r} + \frac{x_i x_j}{r^3} = \left(\delta_{ij}\nabla^2 - \nabla_i\nabla_j\right) r, \tag{B.4}$$

where r is the separation between particles α and β. As discussed before, we are going to split $\mathbf{a}^{\alpha\beta}$ into two parts by writing r as a sum of the error function and the complementary error function such that

$$r = r\,\mathrm{erf}\left[\upsilon r\right] + r\,\mathrm{erfc}\left[\upsilon r\right] \tag{B.5}$$

so that the Rotne-Prager tensor can be written as

$$\mathbf{a}^{\alpha\beta} = \left(\frac{3}{4} + \frac{1}{4}\nabla^2\right)\left(\delta_{ij}\nabla^2 - \nabla_i\nabla_j\right)\left\{r\,\mathrm{erf}\left[\upsilon r\right] + r\,\mathrm{erfc}\left[\upsilon r\right]\right\}. \tag{B.6}$$

where υ is a parameter that controls the convergent rate. According to Beenakker's paper [69], for optimal convergent, $\upsilon = \pi^{1/2}V^{-1/3}$. We then split $\mathbf{a}^{\alpha\beta}$ into two parts,

$\mathbf{a}^{\mathrm{R}}$ and $\mathbf{a}^{\mathrm{K}}$ such that

$$\mathbf{a}^{\mathrm{R}} = \left(\frac{3}{4} + \frac{1}{4}\nabla^2\right)\left(\delta_{ij}\nabla^2 - \nabla_i\nabla_j\right) r \operatorname{erfc}\left[\upsilon r\right], \text{ and} \tag{B.7a}$$

$$\mathbf{a}^{\mathrm{K}} = \left(\frac{3}{4} + \frac{1}{4}\nabla^2\right)\left(\delta_{ij}\nabla^2 - \nabla_i\nabla_j\right) r \operatorname{erf}\left[\upsilon r\right]. \tag{B.7b}$$

Obviously, $\mathbf{a}^{\mathrm{R}}$ converges fast in the real space, and it is the short-range contribution, while $\mathbf{a}^{\mathrm{K}}$ converges fast in the reciprocal space, and it is the long-range contribution. We substitute the decomposition into Eq. (B.2) to give

$$\mathbf{U}^{\alpha} = \frac{1}{6\pi\eta a}\mathbf{a}^{\alpha\alpha}\cdot\mathbf{F}^{\alpha} + \frac{1}{6\pi\eta a}\left\{\sum_{\mathbf{n}}\left(\sum_{\beta=1}^{N}{}'\mathbf{a}^{\mathrm{R},\alpha\beta}\mathbf{F}^{\beta}\right) + \sum_{\mathbf{n}}\left(\sum_{\beta=1}^{N}{}'\mathbf{a}^{\mathrm{K},\alpha\beta}\mathbf{F}^{\beta}\right)\right\}. \tag{B.8}$$

We further add the self-interaction part back in the long-range contribution and then subtract it off,

$$\mathbf{U}^{\alpha} = \frac{1}{6\pi\eta a}\left(\mathbf{a}^{\alpha\alpha} - \mathbf{a}^{\mathrm{K}}(\mathbf{x}=0)\right)\cdot\mathbf{F}^{\alpha} + \frac{1}{6\pi\eta a}\left\{\sum_{\mathbf{n}}\left(\sum_{\beta=1}^{N}{}'\mathbf{a}^{\mathrm{R},\alpha\beta}\mathbf{F}^{\beta}\right) + \sum_{\mathbf{n}}\left(\sum_{\beta=1}^{N}\mathbf{a}^{\mathrm{K},\alpha\beta}\mathbf{F}^{\beta}\right)\right\}. \tag{B.9}$$

The short-range contribution, $\mathbf{a}^{\mathrm{R}}$, after some tedious differentiation, becomes

$$\begin{aligned} a_{ij}^{\mathrm{R}} = \delta_{ij} \Bigg\{ & \left(\frac{3}{4r} + \frac{1}{2r^3} \right) \operatorname{erfc}\left[\upsilon r\right] \\ & + \left(4\upsilon^7 r^4 + 3\upsilon^3 r^2 - 20\upsilon^5 r^2 - \frac{9}{2}\upsilon + 14\upsilon^3 + \frac{\upsilon}{r^2} \right) \frac{\exp\left[-\upsilon^2\right] r^2}{\sqrt{\pi}} \Bigg\} \\ & + e_i e_j \Bigg\{ \left(\frac{3}{4r} - \frac{3}{2r^3} \right) \operatorname{erfc}\left[\upsilon r\right] \\ & + \left(-4\upsilon^7 r^4 - 3\upsilon^3 r^2 + 16\upsilon^5 r^2 + \frac{3\upsilon}{2} - 2\upsilon^3 - \frac{3\upsilon}{r^2} \right) \frac{\exp\left[-\upsilon^2 r^2\right]}{\sqrt{\pi}} \Bigg\}, \end{aligned} \tag{B.10}$$

where $\mathbf{e} = \frac{\mathbf{x}}{r}$.

The long-range contribution is calculated in the Fourier space. For a lattice summation, we can write it in terms of the Fourier series

$$\sum_{\mathbf{n}} \left(\sum_{\beta=1}^{N}{}' \mathbf{a}^{\alpha\beta}\left(\mathbf{x}\right) \right) = \frac{1}{V} \sum_{\substack{\mathbf{k} \\ \mathbf{k}\cdot\mathbf{k}\neq 0}} \left(\sum_{\beta=1}^{N}{}' e^{-i\mathbf{k}\cdot\mathbf{x}} \mathbf{a}^{\alpha\beta}\left(\mathbf{k}\right) \right), \tag{B.11}$$

where

$$V = \mathbf{n}^{(1)} \cdot \left(\mathbf{n}^{(2)} \times \mathbf{n}^{(2)} \right), \text{ and} \tag{B.12}$$

$$\mathbf{k}^{(1)} = \frac{1}{V} \left(\mathbf{n}^{(2)} \times \mathbf{n}^{(3)} \right), \; \mathbf{k}^{(2)} = \frac{1}{V} \left(\mathbf{n}^{(3)} \times \mathbf{n}^{(1)} \right), \; \mathbf{k}^{(3)} = \frac{1}{V} \left(\mathbf{n}^{(1)} \times \mathbf{n}^{(2)} \right), \tag{B.13}$$

and $\mathbf{a}^{\alpha\beta}\left(\mathbf{k}\right)$ is the Fourier transform of $\mathbf{a}^{\alpha\beta}\left(\mathbf{x}\right)$ such that

$$\mathbf{a}^{\alpha\beta}\left(\mathbf{k}\right) = \int e^{i\mathbf{k}\cdot\mathbf{x}} \mathbf{a}^{\alpha\beta}\left(\mathbf{x}\right) d\mathbf{x}. \tag{B.14}$$

After some integrations, (details can be found in Beenakker's paper [69]), we find that

$$a_{ij}^{\mathrm{K}}\left(\mathbf{x}=0\right)=\delta_{ij}\frac{1}{\sqrt{\pi}}\left(6\upsilon-\frac{40}{3}\upsilon^{3}\right),\ \text{and} \tag{B.15}$$

$$a_{ij}^{\mathrm{K}}=\left(\delta_{ij}-\hat{k}_{i}\hat{k}_{j}\right)\left(1+\frac{k^{2}}{4\upsilon^{2}}+\frac{k^{4}}{8\upsilon^{4}}\right)\left(1-\frac{k^{2}}{3}\right)\frac{6\pi}{k^{2}}\exp\left[-\frac{k^{2}}{4\upsilon^{2}}\right]. \tag{B.16}$$

Appendix C

Simulation Flowchart

In this appendix, the process of the simulation is introduced.

1. A initial configuration of particles is randomly distributed inside the primary cell, if the goal is to simulate an infinite suspension. The initial configuration is produced according to the value of the volume fraction, ϕ. At low volume fraction ($\phi \leq 0.1$), the particles are distributed using the Monte Carlo method. At high volume fraction, the particles are first distributed on a regular grid. Then, the particles are nudged out of the grid points by a

random displacement. In both cases, overlap needs to be checked in the end.

2. According to the initial configuration, the initial external body forces, if present, are calculated according to Eq. (3.78). The configuration-dependent tensors $\mathcal{M}^{-1}$ and $\mathbf{R}_{2B} - \mathbf{R}_{2B}^{\infty}$ are computed.

3. We need to invert $\mathcal{M}^{\infty}$. The dimension of the mobility tensor $\mathcal{M}^{\infty}$ is $(11N \times 11N)$, where N is the number of particles. The operation of inverting the mobility tensor is of the order $[(11N)^3]$. To accelerate the simulation, we decompose the mobility tensor into sub-matrices and do a *blockwise inversion*. We write the mobility tensor as

$$\mathcal{M}^{\infty} = \begin{pmatrix} \mathbf{M}_{\mathrm{UF}} & \mathbf{M}_{\mathrm{US}} \\ \mathbf{M}_{\mathrm{EF}} & \mathbf{M}_{\mathrm{ES}} \end{pmatrix} \tag{C.1}$$

where the dimension of $\mathbf{M}_{\mathrm{UF}}$ is $6N \times 6N$, the dimension of $\mathbf{M}_{\mathrm{US}}$ is $6N \times 5N$, the dimension of $\mathbf{M}_{\mathrm{EF}}$ is $5N \times 6N$, and the dimension of $\mathbf{M}_{\mathrm{ES}}$ is $5N \times 5N$. We can invert $\mathcal{M}^{\infty}$ by these submatrices such that

$$\begin{pmatrix} \mathbf{M}_{\mathrm{UF}} & \mathbf{M}_{\mathrm{US}} \\ \mathbf{M}_{\mathrm{EF}} & \mathbf{M}_{\mathrm{ES}} \end{pmatrix}^{-1} = \begin{pmatrix} \mathbf{R}^{*}_{\mathrm{FU}} & \mathbf{R}^{*}_{\mathrm{FE}} \\ \mathbf{R}^{*}_{\mathrm{SU}} & \mathbf{R}^{*}_{\mathrm{SE}} \end{pmatrix} \tag{C.2}$$

where

- $\mathbf{R}^{*}_{\mathrm{FU}} = \left[\mathbf{M}_{\mathrm{UF}} - \mathbf{M}_{\mathrm{US}} \cdot \mathbf{M}_{\mathrm{ES}}^{-1} \cdot \mathbf{M}_{\mathrm{EF}}\right]^{-1}$

- $\mathbf{R}^*_{\mathrm{FE}} = -\mathbf{R}^*_{\mathrm{FU}} \cdot \mathbf{M}_{\mathrm{US}} \cdot \mathbf{M}^{-1}_{\mathrm{ES}}$.
- $\mathbf{R}^*_{\mathrm{SU}} = [\mathbf{R}^*_{\mathrm{FE}}]^{\mathrm{T}}$
- $\mathbf{R}^*_{\mathrm{SE}} = \mathbf{M}^{-1}_{\mathrm{ES}} - \mathbf{R}^*_{\mathrm{SU}} \cdot \mathbf{M}_{\mathrm{US}} \cdot \mathbf{M}^{-1}_{\mathrm{ES}}$

Note that the inversion operations above are carried out by *Cholesky decomposition* to accelerate the simulation, as the hydrodynamic tensors are symmetric positive definite because of the dissipative nature of the Stokes' flow. Then the far-field resistance matrices are added to the corresponding sub-matrices of $\mathbf{R}_{\mathrm{2B}} - \mathbf{R}^{\infty}_{\mathrm{2B}}$ to obtain the resistance matrices.

4. The velocity, $\mathbf{U}$, is calculated according to Eq. (3.70a).

5. The new position is computed by $\mathbf{x}(t + \Delta t) = \mathbf{x}(t) + \Delta t\mathbf{U}$. The choice of the time difference needs to be careful. For a system where the shear rate or magnetic force is strong, Δt needs to be chosen sufficiently small to avoid overlapping. But, if Δt is chosen too small, the simulation cost increases. So, in some studies, an arbitrary volume-exclusive force is imposed to prevent overlapping. In this study, the volume-exclusive force is not included since the computational costs are not high in the simulations.

6. With the new configuration, Steps 2 to 5 are repeated.

Bibliography

[1] D.D. Sriramulu, H. Lünsdorf, J.S. Lam, and U. Römling. Microcolony formation: a novel biofilm model of pseudomonas aeruginosa for the cystic fibrosis lung. *Journal of Medical Microbiology*, 54:667–676, 2005.

[2] M. Dawson, D. Wirtz, and J. Hanes. Enhanced viscoelasticity of human cystic fibrotic sputum correlates with increasing microheterogeneity in particle transport. *Journal of Biological Chemistry*, 278:50393–50401, 2003.

[3] M. Tan, H. Song, P. Dhagat, A. Jander, and T.W. Walker. Theoretical study of alignment dynamics of magnetic oblate spheroids in rotating magnetic fields. *Physics of Fluids*, 28(6):062004, 2016.

[4] M. Tan, A.L. Lambert, B.M. Swann, H. Song, P. Dhagat, A. Jander, and T.W. Walker. Utilizing yield-stress fluids to suppress chaining during magnetic alignment of microdisks via rotating fields. *AIChE Journal*, 64(8):3215–3226, 2018.

[5] V. Imbeni, J.J. Kruzic, G.W. Marshall, S.J. Marshall, and R.O. Ritchie. The dentin-enamel junction and the fracture of human teeth. *Nature Materials*, 4:229–232, 2005.

[6] H.J. Qi, B.J.F. Bruet, J.S. Palmer, C. Ortiz, and M.C. Boyce. *Mechanics of Biological Tissue*. Springer, 2005.

[7] W. Yang, I.H. Chen, B. Gludovatz, E.A. Zimmermann, R.O. Ritchie, and M.A. Meyers. Natural flexible dermal armor. *Advanced Materials*, 25:31–48, 2013.

[8] J.F.V. Vincent and U.G.K. Wegst. Design and mechanical properties of

insect cuticle. *Arthropod structure & development*, 33:187–199, 2004.

[9] B.D. Wilts, H.M. Whitney, B.J. Glover, U. Steiner, and S. Vignolini. Natural helicoidal structures: morphology, self-assembly and optical properties. *Materials Today: Proceedings*, 1:177–185, 2014.

[10] R.M. Erb, R. Libanori, N. Rothfuchs, and A.R. Studart. Composites reinforced in three dimensions by using low magnetic fields. *Science*, 335:199–204, 2012.

[11] G. Ferk, P. Krajnc, A. Hamler, A. Mertelj, F. Cebollada, M. Drofenik, and D. Lisjak. Monolithic magneto-optical nanocomposites barium hexaferrite platelets in PMMA. *Scientific Reports*, 5(11395), 2015.

[12] H. Le Ferrand, F. Bouville, T.P. Niebel, and A.R. Studart. Magnetically assisted slip casting of bioinspired hetogeneous composites. *Nature Materials*, 14:1172–1179, 2015.

[13] R.M. Erb, J. Segmehl, M. Charilaou, J.F.Loffler, and A.R. Studart. Nonlinear alignment dynamics in suspensions of platelets under rotating magnetic fields. *Soft Matter*, 8:7604–7609, 2012.

[14] F. Bentivegna, M. Nyvlt, J. Ferre, J.P. Jamet, A. Brun, S. Visnovsky, and R. Urban. Magnetically textured $\gamma - Fe_2O_3$ nanoparticles in a silica gel matrix: optical and magneto-optical properties. *Journal of Applied Physics*, 85:2270–2278, 1999.

[15] M. Liu, Y. Ishida, Y. Ebina, T. Sasaki, T. Hikima, M. Takata, and T. Aida. An anisotropic hydrogel with electrostatic repulsion between cofacially aligned nanosheets. *Nature*, 517:68–72, 2015.

[16] A.G. Smart. Stiff yet supple hydrogel mimics cartilage. *Physics Today*, 68:12–14, 2015.

[17] V.P. Torchilin. Drug targeting. *European Journal of Pharmaceutical Sciences*, 11:S81–S91, 2000.

[18] L.B. Kong, Z.W. Liu, L. Liu, R. Huang, M. Abshinova, Z.H. Yang, C.B. Tang, P.K. Tan, C.R. Deng, and S. Matitsine. Recent progress in some composite materials and structures for specific electromagnetic applications. *International Materials Reviews*, 58:203–259, 2013.

[19] H. Song, M. Tan, T.W. Walker, A. Jander, and P. Dhagat. Planar alignment of magnetic microdisks in composites using rotating fields. *IEEE Transactions on Magnetics*, 51:1–5, 2015.

[20] R. Han, L. Qiao, T. Wang, and F. Li. Microwave complex permeability of planar anisotropy carbonyl-iron particles. *Journal of Alloys and Compounds*, 509:2734–2737, 2011.

[21] D.G. Grier. A revolution in optical manipulation. *Nature*, 424:810–816, 2003.

[22] M.E.J. Friese, T.A. Nieminen, N.R. Heckenberg, and H. Rubinsztein-Dunlop. Optical alignment and spinning of laser-trapped microscopic particles. *Nature*, 394:348–350, 1998.

[23] B. Edwards, T.S. Mayer, and R.B. Bhiladvala. Synchronous electrorotation of nanowires in fluid. *Nano Letters*, 6:626–632, 2006.

[24] S.J. Papadakis, Z. Gu, and D.H. Gracias. Dielectrophoretic assembly of reversible and irreversible metal nanowire networks and vertically aligned arrays. *Applied Physics Letters*, 88(233118), 2006.

[25] P.A. Smith, C.D. Nordquist, T.N. Jackson, T.S. Mayer, B.R. Martin, J. Mbindyo, and T.E. Mallouk. Electric-field assisted assembly and alignment of metallic nanowires. *Applied Physics Letters*, 77(1399), 2000.

[26] L. Sun, K. Keshoju, and H. Xing. Magnetic field mediated nanowire alignment in liquids for nanocomposite synthesis. *Nanotechnology*, 19(405603), 2008.

[27] T. Kimura, M. Yamato, W. Koshimizu, M. Koike, and T. Kawai. Magnetic orientation of polymer fibers in suspension. *Langmuir*, 16:858–861, 2000.

[28] T. Kimura. Orientation of feeble magnetic particles in dynamic magnetic fields. *Japanese Journal of Applied Physics*, 48(202017), 2009.

[29] H. Song, M. Tan, T.W. Walker, A. Jander, and P. Dhagat. Planar alignment of isolated magnetic disks in newtonian fluids by a rotating field. *IEEE Magnetics Letters*, 6:1–4, 2015.

[30] S. Kim and S.J. Karrila. *Microhydrodynamics: Principles and Selected Applications*. Dover, 1991.

[31] S. Kim. Similarity solutions for the orientation distribution function and rheological properties of suspensions of axisymmetric particles with external couples. *Journal Nonnewton Fluid Mechanics*, 24:297–310, 1987.

[32] M. Mohebi, N. Jamasbi, and J. Liu. Simulation of the formation of nonequilibrium structures in magnetorheological fluids subject to an external magnetic field. *Physical Review E*, 54:5407–5413, 1996.

[33] J.E. Martin, E. Venturini, J. Odinek, and R.A. Anderson. Simulation of the athermal coarsening of composites structured by a uniaxial field. *Journal of Chemical Physics*, 108:3765–3787, 1998.

[34] J.E. Martin, R.A. Anderson, and C.P. Tigges. Simulation of the athermal coarsening of composites structured by a biaxial field. *Journal of Chemical Physics*, 108:7887–7900, 1998.

[35] S. Melle, O.G. Calberón, M.A. Rubio, and G.G. Fuller. Chain rotational dynamics in MR suspensions. *International Journal of Moden Physics B*, 16:2293–2299, 2002.

[36] R.T. Bonnecaze and J.F. Brady. Dynamic simulation of an electrorheological fluid. *The Journal of Chemical Physics*, 96(3):2183–2202, 1992.

[37] R.C. Bell, E.D. Miller, J.O. Karli, A.N. Vavreck, and D.T. Zimmerman. Influence of particle shape on the properties of magnetorheological fluids. *International Journal of Modern Physics B*, 21:5018–5025, 2007.

[38] M.T. López-López, G. Vertelov, G. Bossis, P. Kuzhir, and J.D.G. Durán. New magnetorheological fluids based on magnetic fibers. *Journal of Materials Chemistry*, 17:3839–3844, 2007.

[39] P. Kuzhir, M.T.López-López, and G. Bossis. Magnetorheology of fiber suspensions. II. Theory. *Journal of Rheology*, 53:127–151, 2009.

[40] R.C. Bell, J.O. Karli, A.N. Vavreck, D.T. Zimmerman, G.T. Ngatu, and N.M. Wereley. Magnetorheology of submicron diameter iron microwires dispersed in silicone oil. *Smart Materials and Structures*, 17:015028, 2008.

[41] G.B. Jeffery. The motion of ellipsoidal particles immersed in a viscous fluid. In *Proceedings of the royal society of London A: Mathematical, physical and engineering sciences*, volume 102, pages 161–179. The Royal Society, 1922.

[42] J. Happel and H. Brenner. *Low Reynolds Number Hydrodynamics: with Special Applications to Particulate Media*, volume 1. Springer Science & Business Media, 2012.

[43] S. Kim. Singularity solutions for ellipsoids in low-reynolds-number flows: with applications to the calculation of hydrodynamic interactions in suspensions of ellipsoids. Technical report, WISCONSIN UNIV-MADISON MATHEMATICS RESEARCH CENTER, 1985.

[44] M. Aoshima and A. Satoh. Two-dimensional monte carlo simulations of a colloidal dispersion composed of rod-like ferromagnetic particles in an applied magnetic field. *Modelling and Simulation in Materials Science and Engineering*, 16:015004, 2007.

[45] A. Satoh and Y. Sakuda. Quasi-2D Monte Carlo simulations of phase transitions and internal aggregate structures in a highly dense suspension composed of magnetic plate-like particles. *Molecular Physics*, 108(16):2105–2113, 2010.

[46] A. Satoh. On the orientational characteristics and transport coefficients of an oblate spheroidal hematite particle in a simple shear flow. *Molecular Physics*,

110(18):2137–2149, 2012.

[47] A. Satoh and H. Yokoyama. On the behavior of an oblate spheroidal hematite particle in a simple shear flow under a uniform magnetic field applied in the flow direction. *Colloid and Polymer Science*, 292(4):935–944, 2014.

[48] A. Satoh. Brownian dynamics simulation of a dispersion composed of disk-like hematite particles regarding aggregation phenomena. *Colloids and Surfaces A: Physicochemical and Engineering Aspects*, 483:328–340, 2015.

[49] N. Garraud and D.P. Arnold. Characterization of fluids via measurement of the rotational dynamics of suspended magnetic microdiscs. *Journal of Applied Physics*, 117(17):17B320, 2015.

[50] S. Jäger and S.H.L. Klapp. Pattern formation of dipolar colloids in rotating fields: layering and synchronization. *Soft Matter*, 7(14):6606–6616, 2011.

[51] D.J. Jeffrey and Y. Onishi. Calculation of the resistance and mobility functions for two unequal rigid spheres in low-reynolds-number flow. *Journal of Fluid Mechanics*, 139:261–290, 1984.

[52] S. Kim and R.T. Mifflin. The resistance and mobility functions of two equal spheres in low-reynolds-number flow. *The Physics of Fluids*, 28(7):2033–2045, 1985.

[53] L. Durlofsky, J.F. Brady, and G. Bossis. Dynamic simulation of hydrodynamically interacting particles. *Journal of Fluid Mechanics*, 180:21–49, 1987.

[54] Q. Meng and J.J.L. Higdon. Large scale dynamic simulation of plate-like particle suspensions. Part i: Non-Brownian simulation. *Journal of Rheology*, 52(1):1–36, 2008.

[55] Q. Meng and J.J.L. Higdon. Large scale dynamic simulation of plate-like particle suspensions. part ii: Brownian simulation. *Journal of Rheology*, 52(1):37–65, 2008.

[56] S. Yamamoto and T. Matsuoka. Viscosity of dilute suspensions of rodlike particles: A numerical simulation method. *The Journal of chemical physics*, 100(4):3317–3324, 1994.

[57] M. Yamanoi, C. Leer, F.W.J. Van Hattum, O.S. Carneiro, and J.M. Maia. Direct fibre simulation of carbon nanofibres suspensions in a newtonian fluid under simple shear. *Journal of colloid and interface science*, 347(2):183–191, 2010.

[58] M. Yamanoi and J.M. Maia. Analysis of rheological properties of fibre suspensions in a newtonian fluid by direct fibre simulation. part1: Rigid fibre suspensions. *Journal of Non-Newtonian Fluid Mechanics*, 165(19-20):1055–1063, 2010.

[59] M. Yamanoi and J.M. Maia. Stokesian dynamics simulation of the role of hydrodynamic interactions on the behavior of a single particle suspending in a newtonian fluid. part 1. 1d flexible and rigid fibers. *Journal of Non-Newtonian Fluid Mechanics*, 166(9-10):457–468, 2011.

[60] M. Yamanoi, J. Maia, and T. Kwak. Analysis of rheological properties of fibre suspensions in a newtonian fluid by direct fibre simulation. part 2: Flexible fibre suspensions. *Journal of Non-Newtonian Fluid Mechanics*, 165(19-20):1064–1071, 2010.

[61] M. Yamanoi and J.M. Maia. Stokesian dynamics simulation of the role of hydrodynamic interactions on the behavior of a single particle suspending in a newtonian fluid. part 2. 2d flexible and rigid rings. *Journal of Non-Newtonian Fluid Mechanics*, 166:469–477, 2011.

[62] R. Kutteh. Stokesian dynamics of nonspherical particles, chains, and aggregates. *The Journal of Chemical Physics*, 119(17):9280–9294, 2003.

[63] R. Kutteh. Rigid body dynamics approach to stokesian dynamics simulations of nonspherical particles. *The Journal of Chemical Physics*, 132(17):174107, 2010.

[64] E. Bertevas, X. Fan, and R.I. Tanner. Simulation of the rheological properties of suspensions of oblate spheroidal particles in a newtonian fluid. *Rheologica acta*, 49(1):53, 2010.

[65] L.G. Leal. *Advanced transport phenomena: fluid mechanics and convective transport processes*, volume 7. Cambridge University Press, 2007.

[66] A.J.C. Ladd. Hydrodynamic transport coefficients of random dispersions of hard spheres. *The Journal of Chemical Physics*, 93(5):3484–3494, 1990.

[67] J.F. Brady and G. Bossis. Stokesian dynamics. *Annual Review of Fluid Mechanics*, 20:111–157, 1988.

[68] H. Hasimoto. On the periodic fundamental solutions of the stokes equations and their application to viscous flow past a cubic array of spheres. *Journal of Fluid Mechanics*, 5(2):317–328, 1959.

[69] C.W.J. Beenakker. Ewald sum of the rotne–prager tensor. *The Journal of Chemical Physics*, 85(3):1581–1582, 1986.

[70] E.E. Keaveny and M.R. Maxey. Modeling the magnetic interactions between paramagnetic beads in magnetorheological fluids. *Journal of Computational Physics*, 227(22):9554–9571, 2008.

[71] J.W. Swan, J.F. Brady, R.S. Moore, and ChE 174. Modeling hydrodynamic self-propulsion with stokesian dynamics. or teaching stokesian dynamics to swim. *Physics of Fluids*, 23(7):071901, 2011.

[72] R. Kutteh. Methods for stokesian dynamics simulations of nonspherical particles and chains. *Physical Review E*, 69(1):011406, 2004.

[73] G.K. Batchelor and J.T. Green. The determination of the bulk stress in a suspension of spherical particles to order c 2. *Journal of Fluid Mechanics*, 56(3):401–427, 1972.

[74] R.J. Phillips, J.F. Brady, and G. Bossis. Hydrodynamic transport properties of hard-sphere dispersions. i. suspensions of freely mobile particles. *The Physics of Fluids*, 31:12, 1988.

[75] A.T. Chwang and T.Y. Wu. Hydromechanics of low-reynolds-number flow. part 2. singularity method for stokes flows. *Journal of Fluid Mechanics*, 67(4):787–815, 1975.

[76] T.G. Mason and D.A. Weitz. Optical measurements of frequency-dependent linear viscoelastic moduli of complex fluids. *Physical Review Letters*, 74:1250–1253, 1995.

[77] A. Heilbronn. A new method for the estimation of viscosity in living protoplasts. *Jahrb Wiss Bot*, 61:284–338, 1922.

[78] H. Freundlich and W. Seifriz. Ueber die elastizität von solen und gelen. *Zeitschrift für physikalische Chemie*, 104(1):233–261, 1923.

[79] W. Seifriz. An elastic value of protoplasm, with further observations on the viscosity of protoplasm. *Journal of Experimental Biology*, 2(1):1–11, 1924.

[80] A. Einstein. On the theory of the brownian movement. *Ann. der Physik*, 19:371–381, 1906.

[81] R. Brown. A brief account of microscopical observations made on the particles contained in the pollen of plants. *Phil. Mag.*, 4:161–173, 1828.

[82] J.B. Perrin. Mouvement brownien et réalité moléculaire (Brownian movement and the molecular reality). *Ann. de Chimie et de Physique*, 18:5–114, 1909.

[83] T.G. Mason, K. Ganesan, J.H. Van Zanten, D.A. Wirtz, and S.C. Kuo. Particle tracking microrheology of complex fluids. *Physical Review Lettersters*, 79(17):3282, 1997.

[84] T. Savin and P.S. Doyle. Static and dynamic errors in particle tracking microrheology. *Biophysical Journal*, 88:623–638, 2005.

[85] J.C. Crocker and D.G. Grier. Methods of digital video microscopy for colloidal studies. *Journal of Colloid and Interface Science*, 179:298–310, 1996.

[86] T.G. Mason, H. Gang, and D.A. Weitz. Diffusing-wave-spectroscopy measurements of viscoelasticity of complex fluids. *JOSA A*, 14(1):139–149, 1997.

[87] Y. Mao. Transient microrheological characterization of biogels. 2017.

[88] J. Janesick, K. Klaasen, and T. Elliott. Charge-coupled-device charge-collection efficiency and the photon transfer technique. *Optical Engineering*, 26(10):97, 1987.

[89] F. Ziemann, J. Rädler, and E. Sackmann. Local measurements of viscoelastic moduli of entangled actin networks using an oscillating magnetic bead microrheometer. *Biophysical Journal*, 66(6):2210–2216, 1994.

[90] A.R. Bausch, F. Ziemann, A.A. Boulbitch, K. Jacobson, and E. Sackmann. Local measurements of viscoelastic parameters of adherent cell surfaces by magnetic bead microrheometry. *Biophysical Journal*, 75(4):2038–2049, 1998.

[91] A.R. Bausch, W. Möller, and E. Sackmann. Measurement of local viscoelasticity and forces in living cells by magnetic tweezers. *Biophysical journal*, 76(1):573–579, 1999.

[92] J.P. Rich, J. Lammerding, G.H. McKinley, and P.S. Doyle. Nonlinear microrheology of an aging, yield stress fluid using magnetic tweezers. *Soft Matter*, 7(21):9933–9943, 2011.

[93] M.A. Chilvers and C. O'callaghan. Local mucociliary defence mechanisms. *Paediatric Respiratory Reviews*, 1:27–34, 2000.

[94] P.L. Masson and J.F. Heremans. Sputum proteins. *Fundamentals and Clin-*

ical Pathology. Springfield: Charles C. Thomas, pages 412–474, 1973.

[95] J. Sturgess, A.J. Palfrey, and L. Reid. Rheological properties of sputum. *Rheologica Acta*, 10(1):36–43, 1971.

[96] R. Cone. *Mucus Immunology.* Academic Press, 1999.

[97] I. Carlstedt and J.K. Sheehan. Macromolecular properties and polymeric structure of mucus glycoproteins. *Mucus and Mucosa*, 109:157–172, 1984.

[98] F.A. Meyer and A. Silberberg. The rheology and molecular organization of epithelial mucus. *Biorheology*, 17:163, 1980.

[99] T.M. Chen and M.J. Dulfano. Mucus viscoelasticity and mucociliary transport rate. *The Journal of Laboratory and Clinical Medicine*, 91:423–431, 1978.

[100] K. Adler and M.J. Dulfano. The rheological factor in mucociliary clearance. *The Journal of Laboratory and Clinical Medicine*, 88:22–28, 1976.

[101] S.S. Olmsted, J.L. Padgett, A.I. Yudin, K.J. Whaley, T.R. Moench, and R.A. Cone. Diffusion of macromolecules and virus-like particles in human cervical mucus. *Biophysical Journal*, 81:1930–1937, 2001.

[102] I.Y. Wong, M.L. Gardel, D.R. Reichman, E.R. Weeks, M.T. Valentine, A.R. Bausch, and D.A. Weitz. Anomalous diffusion probes microstructure dynamics of entangled f-actin networks. *Physics Review Letters*, 92(18):178101, 2004.

[103] J.S. Suk, S.K. Lai, Y.Y. Wang, L.M. Ensign, P.L. Zeitlin, M.P. Boyle, and J. Hanes. The penetration of fresh undiluted sputum expectorated by cystic fibrosis patients by non-adhesive polymer nanoparticles. *Biomaterials*, 30:2591–2597, 2009.

[104] B.K. Rubin. Mucus structure and properties in cystic fibrosis. *Paediatric*

Respiratory Reviews, 8:4–7, 2007.

[105] R.C. Boucher, C.U. Cotton, J.T. Gatzy, M.R. Knowles, and J.R. Yankaskas. Evidence for reduced cl-and increased na+ permeability in cystic fibrosis human primary cell cultures. *The Journal of Physiology*, 405:77, 1988.

[106] J.J. Smith, S.M. Travis, E.P. Greenberg, and M.J. Welsh. Cystic fibrosis airway epithelia fail to kill bacteria because of abnormal airway surface fluid. *Cell*, 85:229–236, 1996.

[107] N.N. Sanders, S.C. De Smedt, E. Van Rompaey, P. Simoens, F. De Baets, and J. Demeester. Cystic fibrosis sputum: a barrier to the transport of nanospheres. *American Journal of Respiratory and Critical Care Medicine*, 162:1905–1911, 2000.

[108] R. Hamed and J. Fiegel. Synthetic tracheal mucus with native rheological and surface tension properties. *Journal of Biomedical Materials Research Part A*, 102:1788–1798, 2014.

[109] A.A. Hassan, C.A. Evrensel, and P.E. Krumpe. Clearance of viscoelastic mucus simulant with airflow in a rectangular channel, an experimental study. *Technology and Health Care*, 14(1):1–11, 2006.

[110] D.M. Schenck and J. Fiegel. Tensiometric and phase domain behavior of lung surfactant on mucus-like viscoelastic hydrogels. *ACS Applied Materials & Interfaces*, 8:5917–5928, 2016.

[111] M. Milas and M. Rinaudo. Properties of xanthan gum in aqueous solutions: role of the conformational transition. *Carbohydrate Research*, 158:191–204, 1986.

[112] I.T. Norton, D.M. Goodall, E.R. Morris, and D.A. Rees. Kinetic evidence for intramolecular conformational ordering of the extracellular polysaccharide (xanthan) from xanthomonas campestris. *Journal of the Chemical Society, Chemical Communications*, pages 545–547, 1980.

[113] F. Lambert, M. Milas, and M. Rinaudo. Sodium and calcium counterion activity in the presence of xanthan polysaccharide. *International Journal of Biological Macromolecules*, 7:49–52, 1985.

[114] G. Holzwarth and E.B. Prestridge. Multistranded helix in xanthan polysaccharide. *Science*, 197:757–759, 1977.

[115] M. Rinaudo and M. Milas. Enzymic hydrolysis of the bacterial polysaccharide xanthan by cellulase. *International Journal of Biological Macromolecules*, 2:45–48, 1980.

[116] P.G. DeGennes. Dynamics of entangled polymer solutions. ii. Inclusion of hydrodynamic interactions. *Macromolecules*, 9(4):594–598, 1975.

[117] X. Zhang, D.B. Reeves, I.M. Perreard, W.C. Kett, K.E. Griswold, B. Gimi, and J.B. Weaver. Molecular sensing with magnetic nanoparticles using magnetic spectroscopy of nanoparticle brownian motion. *Biosensors and Bioelectronics*, 50:441–446, 2013.

[118] E.A. DiMarzio and M. Bishop. Connection between the macroscopic electric and mechanical susceptibilities. *The Journal of Chemical Physics*, 60(10):3802–3811, 1974.

[119] V. Marin, E. Holder, M.M. Wienk, E. Tekin, D. Kozodaev, and U.S. Schubert. Ink-jet printing of electron donor/acceptor blends: Towards bulk heterojunction solar cells. *Macromolecular Rapid Communications*, 26:319–324, 2005.

[120] T. Okamoto, T. Suzuki, and N. Yamamoto. Microarray fabrication with covalent attachment of DNA using bubble jet technology. *Nature Biotechnology*, 18:438, 2000.

[121] E.A. Roth, T. Xu, M. Das, C. Gregory, J.J. Hickman, and T. Boland. Inkjet printing for high-throughput cell patterning. *Biomaterials*, 25:3707–3715, 2004.

[122] H. Song, J. Spencer, A. Jander, J. Nielsen, J. Stasiak, V. Kasperchik, and P. Dhagat. Inkjet printing of magnetic materials with aligned anisotropy. *Journal of Applied Physics*, 115(17):17E308, 2014.

[123] W. Voit, W. Zapka, L. Belova, and K.V. Rao. Application of inkjet technology for the deposition of magnetic nanoparticles to form micron-scale structures. *IEE Proceedings - Science, Measurement and Technology*, 150:252–256, 2003.

[124] B. Weidenfeller, M. Anhalt, and W. Riehemann. Variation of magnetic properties of composites filled with soft magnetic fecov particles by particle alignment in a magnetic field. *Journal of Magnetism and Magnetic Materials*, 320(14):e362–e365, 2008.

[125] P.J. Rankin, A.T. Horvath, and D.J. Klingenberg. Magnetorheology in viscoplastic media. *Rheologica Acta*, 38:471–477, 1999.

[126] J. D. Carlson, D.M. Catanzarite, and K.A. St. Clair. Commercial magnetorheological fluid devices. *International Journal of Modern Physics B*, 10(23n24):2857–2865, 1996.

[127] A. Imeson. *Food Stabilisers, Thickeners and Gelling Agents*. John Wiley & Sons, 2011.

[128] C.R. Yuan, N.A. Morrison, and R. Clark. Calcium stable high acyl gellan gum for enhanced colloidal stability in beverages, October 6 2014. US Patent App. 14/507,497.

[129] J.P. Rich, P.S. Doyle, and G.H. McKinley. Magnetorheology in an aging, yield stress matrix fluid. *Rheologica Acta*, 51(7):579–593, 2012.

[130] J.P. Rich, G.H. McKinley, and P.S. Doyle. Arrested chain growth during magnetic directed particle assembly in yield stress matrix fluids. *Langmuir*, 28(8):3683–3689, 2012.

[131] L.G. Wilson and W.C.K. Poon. Small-world rheology: an introduction to

probe-based active microrheology. *Physical Chemistry Chemical Physics*, 13(22):10617–10630, 2011.

[132] G.G. Allen, R.and Fuller and Z. Bao. Aligned SWNT films from low-yield stress gels and their transparent electrode performance. *ACS Applied Materials & Interfaces*, 5(15):7244–7252, 2013.

[133] J.E. Martin. Field-structured polymer composites. In *Macromolecular Symposia*, volume 329, pages 162–172. Wiley Online Library, 2013.

[134] L.J. Van Rooyen, J. Karger-Kocsis, O.C. Vorster, and L.D. Kock. Helium gas permeability reduction of epoxy composite coatings by incorporation of glass flakes. *Journal of Membrane Science*, 430:203–210, 2013.

[135] R.T. Bonnecaze and J.F. Brady. A method for determining the effective conductivity of dispersions of particles. *Proc. R. Soc. Lond. A*, 430(1879):285–313, 1990.

[136] A. Sierou and J.F. Brady. Accelerated stokesian dynamics simulations. *Journal of Fluid Mechanics*, 448:115–146, 2001.

[137] S.H. Strogatz. *Nonlinear dynamics and chaos: with applications to physics, biology, chemistry, and engineering*. CRC Press, 2018.